ALBA BEAMLINE PROPOSAL

SIRENA:

the Surface, Interface and REsonant diffractionN beamline at Alba

Acknowledgements

Contact:

Dr. Xavier Torrelles Albareda	Inst. Ciencia Materiales de Barcelona	ICMAB-CSIC

Local contact:

Prof. Salvador Ferrer Fàbregas	Scientific Advisor ALBA Synchrotron	ALBA-CELLS

Collaborators:

Dr M.J. Capitán Aranda	Inst. Estructura de la Materia	CSIC
Dr. J. Álvarez Alonso	Dpto. Fisica de la Materia Condensada	UAM

With the contributions of:

Dr. Javier Herrero-Martín	BL-29 BOREAS, ALBA Synchrotron	ALBA-CELLS
Dr. Oier Bikondoa	BM28 XMAS, ESRF Synchrotron	ESRF
Prof. Jose Luis García	Inst. Ciencia Materiales de Barcelona	ICMAB-CSIC
Dr. Esther Barrena	Inst. Ciencia Materiales de Barcelona	ICMAB-CSIC
Prof. José Ángel Martín Gago	Inst. Ciencia Materiales de Madrid	ICMM-CSIC

INDEX

ABSTRACT

We propose a beamline to investigate surface and interface atomic structures and dynamical processes with x-ray diffraction at large and small (GISAXS) scattering angles. The beamline aims to satisfy the existing Spanish community in the fields of: (i) surface crystallography of ultrathin films and atomic layers, (ii) heterogeneous catalysis in operando conditions (i.e. above atmospheric pressure) with thin films, model single crystal surface catalysts and supported nanoparticles, and (iii) solid- liquid interfaces for electrochemistry and fuel cells applications.

In addition, the experimental set up would also allow to investigate charge ordering and magnetic diffraction by performing energy resolved azimuthal scans of the diffracted beams.

The beam at the sample position will have approximate dimensions of 10 micrometers in both horizontal and vertical directions, which is appropriate for coherent diffraction imaging applications. In addition, the beamline optics will be windowless allowing to have a vacuum path from the photon source to the sample if desired.

SIRENA will be a beamline with an open and flexible architecture able to accommodate a variety of experiments. The end station will be based in a heavy duty vertical diffractometer designed to host small UHV chambers, reactor cells, cryostat magnets and scanning probes among others. The extent of realization of these possible experimental possibilities will depend on how fruitful the collaboration with user groups actively involved in instrumentation development will be.

1. INTRODUCTION

The goal of SIRENA-beamline is to provide to the scientific community a beamline with surface diffraction set-up and controlled sample environment for surface studies in different areas of physics, chemistry and biology.

The interest of this project is to combine two different scientific aspects. On the one hand to be able to explore novel scientific fields of increasing interest as it is the study of the growth of organic layers in surfaces or the research in new catalysts in operando at atomic scale by mainly using the GIXRD technique (Grazing Incidence X-Ray diffraction). On the other hand, to combine the GIXRD results with other complementary scientific studies of diffraction at surfaces, which are largely present within the Spanish scientific community, e.g., GISAXS (Grazing Incidence Small Angle X-Ray Scattering), RXS with polarization control (Resonant X-Ray Scattering), anomalous scattering and coherence.

We propose an undulator beamline at ALBA that utilizes the source's high brilliance coupled with the latest advances in x-ray diffraction techniques (polarization, resonance and coherence) to create a powerful and versatile X ray diffraction station facility.

The undulator will be located in a medium straight section and will provide a tunable monochromatic beam in an energy range from 4.5 to 22 keV. The exploitation of large bandwidth beams for fast measurements will depend on future technological advances in energy resolved detectors. The beamline will have two stages of horizontal (H) focusing to achieve a rounded focus at the sample. This beam will be used in one experimental hutch with a removable sample station with capability for applying different wide angle techniques, i.e., grazing incidence diffraction of X rays to study surfaces, interfaces and nanostructures of different materials in several environments, reflectivity, resonant X-ray scattering with polarization analysis, single crystal, powder, CXDI and small angle techniques (GISAXS).

As was commented above, the techniques available with this beamline can be used in quite different research fields. In the figure below some key areas that are expected to be prominent in the proposed beamline are shown. These thematics address to research areas offering great challenges with high social impact but require advances in novel materials with not just a single approach, but rather with a flexible and broad range of capabilities that can be utilized synergistically. To meet this challenge, the Beamline will enable the *in-situ* study of materials in a flexible range of environment chambers, providing a polarised micro focused beam with an intensity nearly to 10^{12} ph/sec at 8 keV with Si (111) at working distance of 1 to 2 m from the focusing optics. In addition to facilitating studies of inhomogeneous materials, this will allow the entire beam intensity to be placed at grazing incidence on millimetre size horizontal samples for surface and interface studies.

In addition to providing state of the art grazing incidence diffraction techniques, we propose to push the beamline along the following directions:

1- large available space: In-situ studies often require building dedicated sample environments. Typically the available space for these setups is small, resulting in adapting the experiment to the setup and measuring on model systems in model environments limited by the small available space.

The vertical geometry of the diffractometer will be able to host different sample environments like heavy preparation chambers to allow in-situ studies of solid surfaces, interfaces, nanometric objects and growth mechanisms, as well as other type of cells required by users, i.e., electrochemical cells, Langmuir trough and catalytic chambers… for the study of interfaces (liquid-liquid, liquid-solid, solid-gas).

2- The beamline will be equipped with state of the art detectors that allow to acquire 2D diffraction images at elevated frame rates which are appropriate for time resolved experiments such as reaction kinetics, structural evolution, phase transitions etc...

3- Tunable energy: The ability to scan the energy through a particular elemental edge allows resonant

scattering experiments to measure weak or non-observable reflections that could make them observable via the resonant enhancement. By exploiting the anomalous contrast and polarization dependence, measurements of very weak but information-rich scattering processes, such as magnetic diffraction (resonant and no-resonant) and anisotropic scattering (charge, orbital and multipolar orderings) will get the opportunity to extract electronic and chemically specific structural information, i.e., DAFS/MAD techniques.

4- SIRENA will be able to perform wide angle diffraction by setting the diffractometer at specific diffraction conditions and also GISAXS simultaneously during dynamic processes as chemical reactions. The small beam dimensions at the sample might allow collecting coherent diffraction data at small and large angles simultaneously.

5- UHV surface preparation laboratory: The absence of a second experimental hutch with an UHV fixed chamber mounted on a diffractometer make this workshop mandatory for an optimal use of the SIRENA Beamline. Moreover, the Beamline should be equipped with the maximum number of different sample environments to support the different experiments that will be requested for the users: reaction chambers (batch and flow modes), baby chambers, Nima Langmuir troughs and other liquid through (Langmuir-Blodgett) to create, modify and study Langmuir films, specific cells to study surfaces in controlled wetting conditions and or liquids on surfaces in stationary conditions. Special care will be made on the design of the electrochemical cell to permit the simultaneous acquisition of electro-chemical impedance spectra (EIS).

To achieve these objectives, we would like to built a beamline with open and flexible architecture allowing a large variety of experiments to satisfy the current and/or future needs of the surface science users of ALBA. The technical requirements of the beamline optics and experimental hutch, i.e. beam size, energy range, windowless source-sample path, x-rays polarization, heavy duty vertical diffractometer with an open configuration… will be accomplished to give the opportunity to the SIRENA users the possibility to make, among others, specific type of experiments exploiting the coherence properties of the beam or combine diffraction and or coherence techniques with scanning probes simultaneously. To note that although the beamline will be offered to the users for giving them the possibility to perform such experiments, those **experienced** users interested on them, in collaboration with the scientific staff of SIRENA, will have to develop the techniques through collaborative scientific projects, software development and any other requirement needed to implement the technique in the beamline with the objective to offer this new service (or tool) to any other user.

SCIENTIFIC FIELDS:

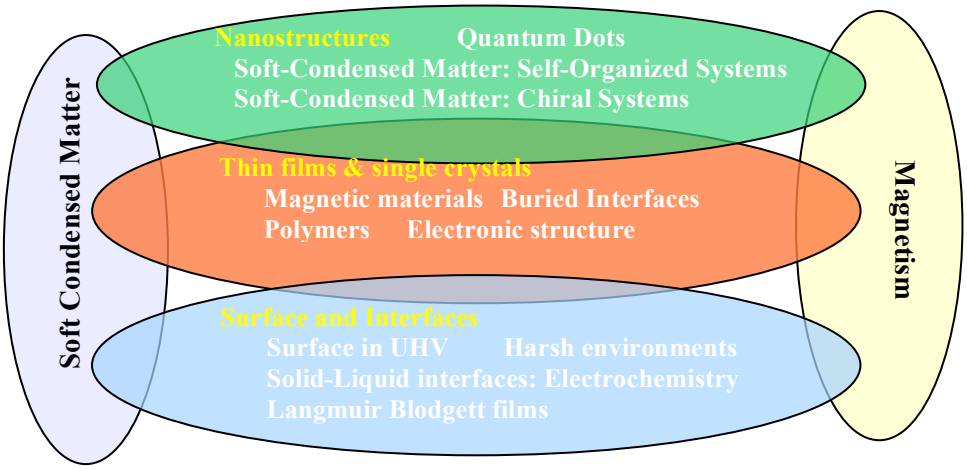

2. MAIN FEATURES OF THE BEAMLINE

1.- Source:
Horizontally polarized radiation delivered by an in-vacuum undulator. Energy from 4.5 to 22 keV

2.- Optics:

2.1 Silicon 111 monochromator and focusing mirrors to deliver at the sample position a monochromatic beam ($\Delta\lambda/\lambda \cong 10^{-4}$) of approximate dimensions 10 (H) x 7 (V) μm^2 FWHM and ca. 10^{12} ph/s in the whole energy range.

The beamline has to be windowless and it has to have the possibility of having a vacuum path from the sample to the source.

2.2 Quarter wave plate for variable polarization experiments.

3.- End station

3.1 Diffractometer:

Heavy duty vertical axis 8 circle diffractometer able to accommodate ~150 kg loads at the sample stage.

The detector arm has to be robust to install heavy detectors and be equipped with an analyzer crystal set up that in addition allows azimuthal rotation around the diffracted beam.

A linear stage of a length of ca. 3m to install an evacuated tube for GISAXS or coherent scattering measurements.

3.2 Detectors:
2D photon counting pixel detector
Scintillator detectors

3.3 Sample environment:
UHV/flow reactor chamber for in situ catalysis experiments
UHV baby chamber for surface structure determination
Electrochemical cell set up
Portable chamber for in-situ growth and GISAXS experiments

Other components of the sample station that might be eventually considered are:
A UHV cryostat, a DC magnet, and an AFM set up compatible with grazing diffraction

The deployment of all the possibilities of the beamline, largely will depend on the interests of the users (or specific groups of expert users) to develop them through collaborative research projects with the beamline staff. The objective of this collaboration will be the development first and implementation later of the technique in the beamline for being offered to the users community as a standard technique.

3. SCIENTIFIC CASE

Surface X-ray diffraction under grazing incidence (GIXRD) is nowadays well established in the panel of surfaces and interfaces structural probes. Following the pioneering experiments of Marra and Eisenberger [1], dedicated surface diffraction beamlines have been built in almost all synchrotron radiation facilities. Indeed the structural information is a key step for a complete understanding of the physical and chemical properties of ultra thin heterostructures involved in modern materials science and technology.

The reduced dimension of artificial structures, thin films, wires or dots, single layers supported catalysts, induces new physical and chemical properties associated with the confinement. These effects, first observed in semiconductor quantum wells many years ago, are still the object of intense research in systems like self-assembled quantum dots by using the new imaging synchrotron technics to unravel their morphology, inner structure or strain distribution under (or not) applied external strain conditions. A major effort is also dedicated nowadays to the understanding and design of metal/metal, metal/insulator, metal/semiconductor and insulator/insulator nanostructures where the magnetic, catalytic, and transport properties can be tailored by selecting the size of the individual objects or the donor/acceptor nature between specimens.

The study of nano-objects has thus become very important not only for fundamental issues but also for its broad technological impact. Nanostructured systems concern physics, chemistry and also biology communities, interested in their optical, magnetic, electrical and catalytic properties. Heteroepitaxy, faceting, grafting are elemental processes leading to spontaneous nanopatterning and a detailed knowledge of the atomic structure of the initial substrate surface together with a continuous control of the structural and morphological evolution of all the components during the material processing is mandatory.

If many studies can be performed by laboratory UHV techniques like LEED, RHEED, STM... directly coupled to the growth chamber, they are now very often complemented by GIXRD experiments at different synchrotron radiation facilities. Moreover, for whole classes of materials and systems like the solid-liquid or solid-gas interfaces at high pressure, the "standard" UHV techniques cannot be used. It should be emphasized that such systems are at the core of several subjects of growing importance like the reactivity of metal catalysts; the study of glass-metal interfaces or the electrochemical interfaces among many others. These studies requiring brilliant hard X-ray sources are being developed at third generation synchrotron facilities like ESRF, APS-Argonne, DIAMOND and SOLEIL. Indeed, more than simply bringing a higher precision with respect to the standard UHV structural techniques, GIXRD offers a unique tool to control easily the penetration of X-rays in the material from the very first atomic planes to several micrometres simply by tuning the incidence angle. This allows studying buried interfaces to evaluate distortions induced by the surface structure deep inside the crystal or to probe the strain distribution across a thin film.

Nevertheless, the main specificity of GIXRD is still to allow atomic structure determinations in surface science in the framework of the Born approximation of single scattering, which greatly simplifies the data treatment. To be reliable, these structure determinations imply a careful control of the surface and therefore ultra high vacuum conditions together with preparation and characterisation tools interconnected with the diffractometer. Moreover the high counting rate obtained with third generation synchrotron sources allows to perform studies *in-situ*, in real time and in extremely stringent experimental conditions (high temperature, magnetic field, gas atmosphere, wet conditions), enabling to follow growth kinetics and surface structure transitions.

The importance of the sample preparation facilities associated with the GIXRD experimental station has been clearly demonstrated during the last 20 years; however, from a few years ago a change of tendency and of preferences is being observed among the international scientific community of synchrotron radiation users in this field. The original idea to prepare the surfaces of interest in UHV chambers equipped with all sample cleaning and growth characterization

tools, permanently mounted on its diffractometer, is being less attractive than: i) perform the surface characterization in Surface Labs equipped with STM, LEED and AES techniques for transferring later the prepared sample in UHV baby chambers to be mounted on the diffractometer, ii) home preparation UHV chambers (< 100 Kg) that can be directly mounted on the diffractometer. These last chambers would cover in-situ growth experiments. The lasts statistics at ESRF, DIAMOND and SOLEIL clearly show the preferences of their users for this modality respect to a fixed UHV chamber. Most of their uses refer to samples prepared in Surface Labs that are transferred to the UHV diffractometer chamber using a baby chamber.

The in-situ sample preparation on a fixed UHV chamber has been evolved towards access to surface preparation labs because i) these infrastructures are becoming part of the user facilities of these beamlines, and ii) the possibility to prepare the surface samples before starting the experiment, so not consuming beam time, and iii) previous preparation of the experiment performing and testing specific designs for particular samples geometries and conditions.

The main scientific areas of interest that motivated the present beamline proposal focus on:

- Organic thin films on metals and inert substrates. A large number of studies have demonstrated that surface diffraction is a valuable tool for characterizing the ordering of organic molecules on substrates. The development of self-assembly processes capable of generating functional surfaces with well-defined and tunable properties promises to have far-reaching consequences for biological and medical applications. Furthermore, these self-assembly processes can lead to preparation and tailoring of intrincated surfaces with unique properties for electronic and optical application. Moreover, the interaction between chiral molecules with the surface substrate can induce homochirality at surfaces.
- Heterogeneous catalysis in model systems (single crystals), membranes and thin films and/or polycrystalline systems in batch and flow reactors [2].
- New types of materials, and even new states of matter, are being discovered at an accelerating rate, as those becoming to Group 15 (pnictides exhibit high-temperature superconductivity), topological insulators, and novel quantum-critical states. From an applied viewpoint, materials combining several functional properties – the multiferroics – hold promise for future device applications. The SIRENA Beamline will provide a unique tool for studies of these materials. Because of significant resonant enhancement, magnetic signals, multipolar orders, the effects of spin-orbit coupling, charge/orbital order, and the effects of crystalline environment all can be studied in the 3d elements as Se chalcogens and Br halogens (K-edges); the 4d through the lanthanides and most of the 5d elements (L-edges); and the actinides (M-edges). The combination of such an extended energy range with full polarization control/analysis would be unmatched in the world and will allow definitive characterization of the electronic states, including their multipolar character and the quantum-mechanical nature of the magnetic moment. Importantly, such studies will be possible in environmental chambers with limited access (such as magnets) – a task that requires full polarization control. This will provide unique insight into the physics of antiferromagnetic domains, chiral magnetic systems, and many multiferroic states, which are inaccessible to other experimental techniques such as PEEM. It will also provide crucial information for future applications of multifunctional materials. Finally, coherent scattering techniques could also be used at resonance to study static and dynamic properties of domains in an unmatched range of materials.

4. USER CASE

The potential user community for a diffraction beamline is large and covers multiple techniques and scientific fields. As such SIRENA will have users in most Spanish universities and nano/micro science dedicated Spanish research institutes. The particular conception of the diffractometer (big free space and heavy chambers support) will benefit several European groups that currently are limited to accommodate their heavy portable chambers in ANKA and ESRF (ID03, ID10).

The exact combination of techniques and sample environments which will make the beamline unique remains to be created, however, the presence of a number of groups with research subjects centred on gas/solid and solid/liquid interactions warrants that dedicated setups will be built and used. Below are listed a few examples of potential users who have expressed direct interest for a diffraction beamline that are grouped around some scientific cases representative of their research areas.

It should be noted that Spanish Public Research Institutions are present in the synchrotron user community represented by a non-profit Spanish Association of Synchrotron Users (AUSE) as consequence of the relevance that synchrotron facilities have in most research areas. This Association has a broad experience of synchrotrons over many years and is often involved in tasks related with:

- Dissemination of the new opportunities offered by synchrotron radiation to solve scientific and technical problems
- To achieve a better use of available beam time for our community by using a fluid exchange of ideas
- To articulate an efficient mechanism to permit the contact among the Spanish users of Synchrotron Light in the various experimental techniques (mainly via web media)
- To define the areas of interest of the users in this field
- To serve as a link between those project responsible being carried out on synchrotron techniques and users (with or without previous experience).

4.1. GIXRD

4.1.1 Surface structure

From the opening of the ESRF and the active Spanish participation as funding member of this facility, a rather large community of Spanish scientific groups have been central in development and using Surface X-Ray Diffraction (SXRD) techniques, beginning from the initial designing and building of the Surface Diffraction beamline at the ESRF and pushing to surface structure, surface magnetism and crystal growth areas [3-5].

Surfaces and interfaces define a boundary between a material and its surrounding environment and influence interactions with the environment (it is the first thing we can “see”, either with the naked eye, or with various probes, e.g., electron diffraction, helium atom scattering, scanning probes…). At the molecular level, the surface atoms have a different chemical environment, that is, fewer nearest neighbours, from that in the bulk. As consequence, these surface atoms with changed atomic and electronic structures might exhibit high chemical reactivity. This property makes surfaces and interfaces a favoured medium for physical, chemical and biological processes in nature and in technological applications. That probes that smaller is the size of an object greater will be the relative importance of the surface (therefore important in the “nanoworld”).

Consequently, interesting phenomena may be observed on surface/interface but not in bulk, e.g.,

- Surface reconstructions (atomic rearrangement at surface)
- Surface elementary excitations: surface phonons, plasmons, etc.
- Uniquely 2-D phenomena, e.g. properties of a 2-D electron gas at interfaces between oxides…

However, the surface processes involve lower number of atoms in comparison with similar processes could happen in bulk [6,7]. For this reason, high brightness synchrotron grazing incidence X-ray scattering techniques are required to characterize the chemical structure of the surface [8]. Apart of the usual low intensities due to the intrinsically diluted nature of a surface, if information on the surface magnetic structure is pursued, one faces an additional weakening of the diffracted intensities by several orders of magnitude, so the XRMS enhancement is required to observe any magnetic contribution from the surface. Such difficult measurements will provide a significant and unique insight into surface magnetic ordering.

The interaction between substrates and organic or carbon based molecules induces large lateral arrangements on the substrate surface generating surface reconstructions with large unit cells. Usually, the intensities coming from these types of atomic periodicities are small, so intense X-ray beams impinging onto the sample are desirable. The literature is nowadays fully illustrating the degree of development of this technique in the surface crystallography area, some few examples are shown below.

Examples

4.1.1.1 Molecular linear systems

4.1.1.1.1 Unrevealing the surface chemistry of the thiolate (√3×√3)-R30° on gold

Thiol self-assembled monolayers (SAMs) on gold are the most popular molecular thin films because this substrate provides oxide-free, clean, flat surfaces that can be easily modified not only in gas phase but also in liquid media under ambient conditions. In particular, SAMs on Au(111) have been extensively studied because they are considered as model systems to understand the basic aspects of the self-assembly of organic molecules on well-defined metal surfaces. Also, a great interest has arisen in the surface structure of thiol-capped gold nanoparticles (AuNPs) because of their simple synthesis method that results in highly monodisperse particles with controllable size. They show a high surface/volume ratio, which makes them very attractive for technological applications in different fields ranging from medicine to heterogeneous catalysis. Thus, the understanding of the nature of the sulphur-gold (S-Au) interface, on both planar and nanoparticle surfaces, has been the focus of intensive research. However, it is remarkable that, in spite of the considerable theoretical and experimental efforts made using different and sophisticated techniques, the structure and chemical composition of this interface at the atomic level remain elusive. In particular, the search for a unified model of the chemistry of the S-Au interface has become one of the most challenging topics because it illustrates the difficulty of determining the surface chemistry at the nanoscale. In fact, while its is accepted that the surface structure of gold nanoclusters (size < 2 nm) is composed by RS-Au_{ad}-RS (RS-Me: strong thiolate-metal bond) or RS-Au_{ad}-SR-Au_{ad}-SR species the chemistry of the thiolate SAMs on the Au(111) and Au(100) planes is still under debate. The knowledge of the thiolate Au(111) system is particular relevant as the {111} faces involves about 70% of the AuNPs surface with size smaller than 10 nm.

At saturation coverage (θ=0.33) thiols arrange on gold forming different stable lattices: (3×4), for short thiols with a number of C atoms n < 3, and (√3×√3)-R30° and/or c(4×2) for n > 3, which can coexist on the substrate. In this way, many efforts have been done to determine the adsorption site of the S head of the thiol molecules on the gold surface. The structural models

initially proposed considered an unreconstructed (U) Au(111) surface, and hollow, bridge or intermediate sites have been alternatively proposed as those energetically favoured for chemisorption. However, all these models have been reviewed since experimental data suggested that thiol chemisorption promotes a strong substrate reconstruction. Because chemical bonding is a local issue, one approach to tackle this problem is to use the information provided by Au nanoclusters. In this way, efforts have been recently made to model the thiolate-Au(111) interface in terms of RS–Au_{ad} species under the form of complexes or polymers, in analogy with those found in nanoclusters. Eventually, a unified model for the thiol-Au interface with the RS–Au_{ad}–SR staple motif, valid for both Au nanoclusters and Au(111) surfaces, has been proposed [9].

While the RS–Au_{ad}–SR complexes are compatible with the (3×4) (RS–Au_{ad}–SR in *trans* configuration) and c(4×2) (RS–Au_{ad}–SR in *cis* configuration) lattices [10,11], the surface chemistry of the paradigmatic (√3×√3)-R30° lattice imaged by STM, which dominates for alkanethiols with n > 10, does not seem to be compatible with these species. Consequently, the understanding of the (√3×√3)-R30° structure is key to unravel the nature of the SAMs interaction on Au(111) to determine whether the thiol SAM is formed on an unreconstructed gold surface or gold adatoms are involved. The (3√3×3√3)-R30° surface model recently proposed [9] could help to solve this dilemma. Figure 1 shows two models with S–Au distances in excellent agreement with those experimentally found for different alkanethiolate (√3×√3)-R30° lattices on the Au(111) interface [12].

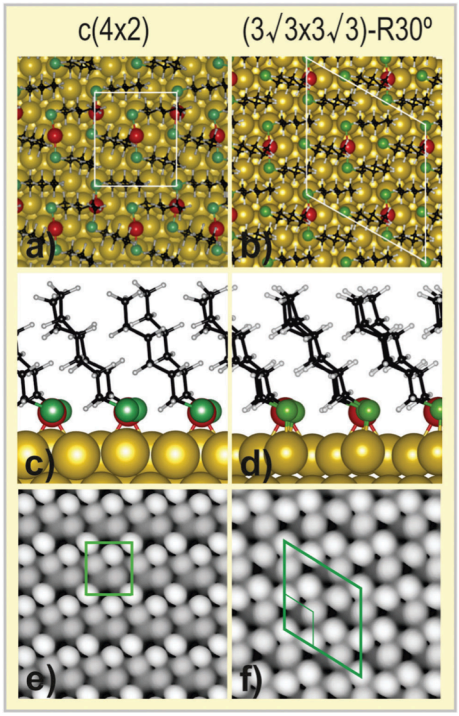

Figure 1. *(a–d) Optimized hexanethiolate surface structures on Au(111). Left panel: c(4x2) Right panel: (3√3x3√3)R30º. In (a) and (b) top view, in (c) and (d) lateral view of the surface structures. Green: S; black: C; white: H; red: Au adatom; yellow: Au. The corresponding unit cells are drawn on the figures. (e) and (f) show simulated constant current STM images of the c(4x2) (e) and (3√3x3√3)R30º (f) lattices. The corresponding unit cells are drawn on the images. (3√3x3√3)R30º unit cell is also included in (f).*

One way to solve this structural problem would be measuring the average (√3×√3)-R30° structure. The (3√3×3√3)-R30° model is the newest proposed model to account the compatibility between the (3x4), c(4x2) and (√3×√3) models and contains 3 Au adatoms so, 1/3 Au atom by (√3×√3)-R30° cell, so the idea is to measure the average structure in order to detect the presence of fractional portions of adsorbed gold adatoms on the surface to validate/reject the presence or not of RS–Au_{ad}–SR complexes [9] on it. Another advantage for measuring this average structure is that it defines the nearest-neighbour thiol-thiol distances, consequently, the structure from this average structure would be up to 2 orders of magnitude higher than other reconstructions implying larger unit cells (Figure 2).

In order to minimize SAM damage during the experiment, the X-ray energy of the

incident beam should be set at 11.579 keV (or close), below the gold L_{III} absorption edge, to avoid both the background due to the gold fluorescence and emitted Auger electrons. It is usual in this type of experiments to refresh the surface sample in case severe radiation damage is produced.

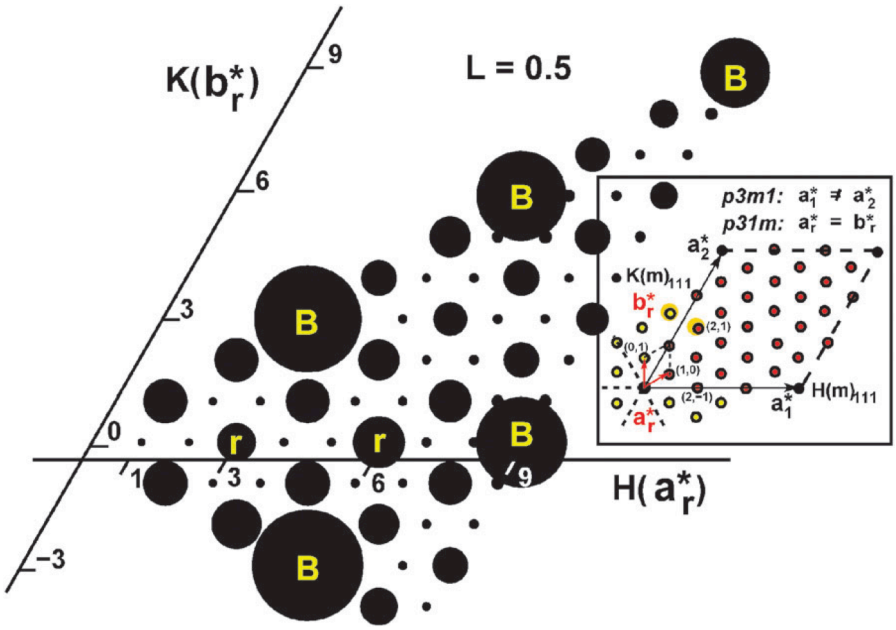

Figure 2. *Portion of the two-dimensional non-equivalent reciprocal space quadrant generated from the model of Fig. 1b using 6 symmetry p31m related domains. B and r characters identify the reflections having bulk/substrate or contributions from the average (√3x√3) units forming part of the (3√3x3√3)R30° structure, respectively. The areas of the circles are proportional to the corresponding calculated structure factors. The áreas of bulk circles have been reduced by a factor 3 to enhance the contrast of the smallest ones. The image shows a reciprocal space section cut at L = 0.5. (H, K, L) denote the Miller indexes expressed in reciprocal lattice units. Inset: the reciprocal space diagram showing the reciprocal lattice vectors for both the Au(111) substrate (a1*, a2*) and the (3√3x3√3) superstructure (ar*, br*). The (m) label along H and K Au(111) directions denotes mirror planes. (Red circles) Non-equivalent portion of the reciprocal space corresponding to the (3√3x3√3) lattice where reflections of the main figure were calculated; (colored dots) fractional reflections from the (3√3x3√3) superstructure. Reflections outlined in gold/yellow, i.e., (H, K) = (2, 1) are equivalent between them.*

The experiment should consist in measuring fast scans with a 2D CCD camera (L-scans) to minimize the exposure time while also using a fast shutter to avoid sample irradiation during not effective counting time. These types of experiments should be performed using the continuous mode scan where the motor movements of the diffractometer are coupled with the counting time of the CCD camera. This mode has the advantage to minimize the sample exposure time while collecting data with the desired statistics. The detector proposed for such experiments would be a MAXIPIX photon-counting pixel detector [13] described in the beamline setup section.

Moreover, in-situ thiol growth is another important issue that can be followed with synchrotron radiation during its crystallization stage from liquid phase deposition [14]. Capitan et al. showed that the deposition of 1-Nonanethiol monolayers on Au(111) by thiol adsorption from an thanolic solution does not produce observable diffraction peaks at the (1/3,1/3,1) reciprocal-space position after 2 h and subsequent rinsing during 10 min. The replacement of the ethanol by a continuous flow of helium (30 mL/min) produces a diffraction peak characteristic of the (√3x√3)-

R30^{o} overlayer structure after 10 h (Figure 3), evidencing the crystallization of the thiols chains after the solvent evaporation. It should be noted that no diffraction peak was detected maitaining the sample in contact with the solution for up to 20 h [14].

This study concludes that in the presence of a liquid phase, even if the thiol heads can be periodically arranged on the gold substrate, the alkyl chains, which contribute most of the monolayer scattering power at the recorded L position, do not display long-range order, particularly along the surface normal where the scanning probe techniques are silent.

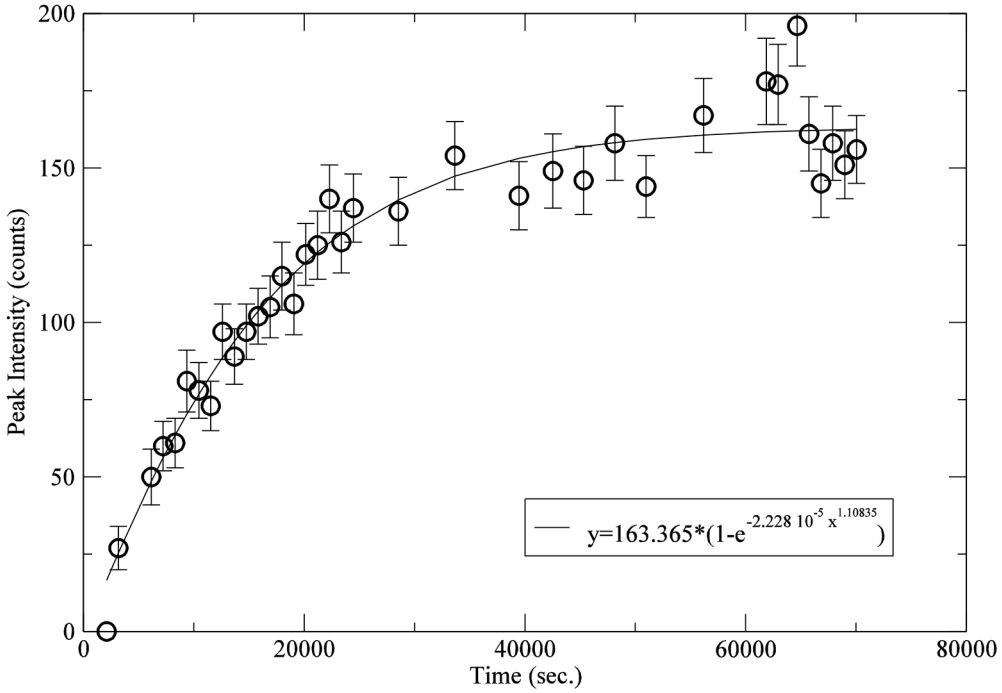

Figure 3. *Time evolution of the (1/3 1/3 1) thiol diffraction peak showing the crystallization of the thiol monolayer when the solvent is removed. The data can be fitted with the Kolmogorov–Avrami theory which gives a dimensional parameter close to 1, indicating a constant rate of nucleation combined with ordered domains of homogenenous size whose number increases with time.*

4.1.1.2 Chiral molecules

A field that is acquiring a great importance in the last years is related to the organic film and their chirality capabilities. It has potential benefits in the ability of the surface to selectively adsorb one enantiomer in preference to the other [15]. In many molecular systems it is very important to ensure the purity of the molecules and can be very difficult to separate molecules having the same chemical composition that only differ in the handedness of their structure. Such studies are invaluable as the effectiveness of many drugs depends on this distinction, as demonstrated by thalidomide. The ability of specific surfaces to adsorb certain molecules has therefore tremendous potential in the role of molecular purification. Recently, asymmetries in the scattering probability of polarized electrons from chiral molecules have been demonstrated [16]. Even for unpolarized electrons, enantio-selective scattering has been predicted.

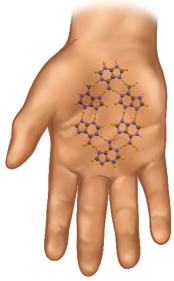

Prochiral molecules can produce chiral structures upon adsorption on surfaces or interfaces in which the interface plane breaks the mirror symmetry of the molecule. An example of this is the adenine [17]. The deposition of DNA basis on surfaces is receiving significant attention opening the way for new bio-medical and pharmacological applications.

X-ray diffraction is a valuable tool that can be used to study these systems. The chiral arrangement of prochiral molecules can be easily distinguished from the racemic mixture of molecules due to the differences in symmetry of the unit cell that results in the appearance or the disappearance of diffracted features.

In the case of the growth of adenine on Au(111) it has been found that two crystalline phases (alpha-beta structure) exist. Both phases are energetically quasi-degenerated and exhibit a very similar structure consisting in the "pile-up" of adenine planes. In the case of the alpha-adenine the stacked planes are enantiopure planes while in the beta structure the stacked planes are a racemic mixture of both chiralities. It has been found that under certain conditions the growth of the alpha phase is favoured resulting in surfaces covered with adenine islands which are chiral from the first stages of the growth. Upon adenine deposition, a number of diffraction peaks, as those shown in the diffraction peaks of Figure 1, appear in the radial patterns while they are

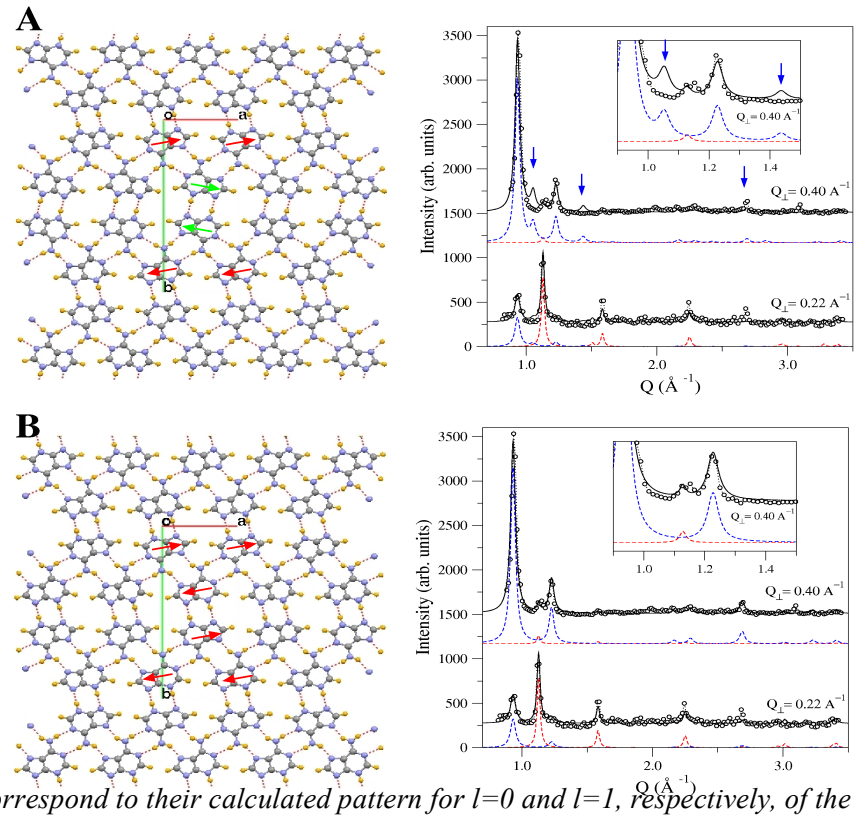

Figure 1. *Two different plane structure models used in the data analysis. (A) and (B) correspond to the p2gg 2D symmetry group and the 2D plane derived from the 3D Fdd2, respectively. Calculated diffraction patterns for their corresponding structures at two different perpendicular momentum transfers compared with the recorded experimental data are shown. Arrows indicate reflections related qwith the symmetry of the molecules. The calculation was done by considering a highly textured growth of the adenine crystals with the adenine planes lying parallel to the substrate surface (adenine c-axis is parallel to the substrate surface perpendicular direction). The red and the blue lines correspond to their calculated pattern for l=0 and l=1, respectively, of the adenine lattice.*

constant and isotropic in the azimuthal scans (rotation around an axis perpendicular to the sample surface). The adenine growth forms a polycrystalline mosaic on the gold surface. For the x-ray data analysis two models are compatible with the submonolayer adenine coverage. The structural model shown in Figure 1A has two symmetrically bonded adenine dimers per unit cell with a 2D symmetry group p2gg. The second structure model (Figure 1B) has identical cell dimensions than the previous one but belongs to the symmetry group p2. In the right panel of Figure 1 the experimental and calculated diffraction patterns obtained for both models are shown. An inspection of both diagram patterns shows that the stacked structure of the p2gg planes has Bragg peaks that are not observed in the measured patterns (indicated by arrows).

Another example of the viability of these types of chiral studies by means of surface diffraction can be found in [18] that reports results on the growth of PVBA over a substrate.

In the quest of the genesis of chiral structures there is a inspiring question: "Can the asymmetry of a chiral field –such as a specifically oriented magnetic field, radiation field, or the combination of both– be transferred to racemic or prochiral organic molecules in a manner that an enantiomeric enhancement is induced, that is to say, transferred from the mass-less chiral field into the organic molecule?" And indeed, the answer to this question is "yes".

The combination of chirality and magnetism stems from Pasteur's work is particularly appealing. In the 80's, Barron reformulated and generalized the definition of chirality given by Lord Kelvin to include motion; a chiral system is thus defined as one in which space parity is broken, while time parity is conserved [19]. This point of view has recently been confirmed by experiments: it has been demonstrated how chirality can be introduced in a system by the so-called "magnetochiral anisotropy" effect, combining a magnetic field parallel to the direction of propagation of an unpolarized light beam [19]. In this way enantiomeric excess is generated in a chemical reaction. The setup envisaged for this beamline would also allow explore this highly suggestive subject.

Conversely it has been found that planar chiral structures are an intriguing new type of optical meta-material which offer the possibility of effective manipulation of the polarization state of light in the far and near fields, as well as manifesting a range of new phenomena such as 2D optical activity.

4.1.1.3 Metallic surfaces on insulating oxides

Perovskite (PV) type oxides play a central role in the field of oxide electronics. For instance, the archetype ferroelectric $BaTiO_3$(BTO) has attracted much interest motivated by applications in multiferroic tunnel junctions [19-21], which might open new functionalities in the field of spintronics [22]. Similarly, heteroepitaxial PV structures such as $SrTiO_3$(STO)/$LaAlO_3$ have become a central topic in solid state physics owing to the presence of a two- dimensional (2D) electron gas at the interface [23,24]. Surface x-ray diffraction (SXRD/GIXRD) can provide direct evidence for a structural model concerning the atomic geometry of the BTO(001)-(2x1) reconstruction [25]. In combination with ab initio calculations it is possible to link the atomic

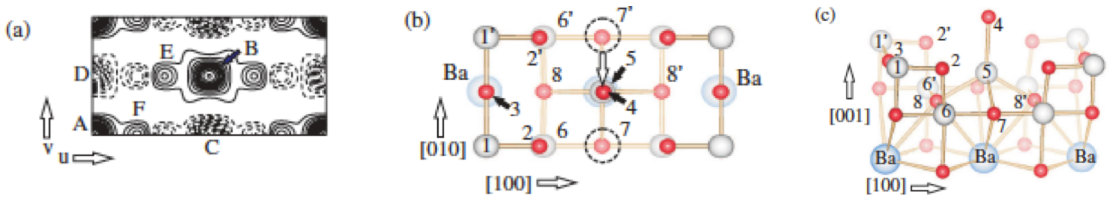

Figure 1 *(a) Paterson function of the projected structure. (b) Structure model of the (2x1) reconstructed unit cell projected along [001]. Atoms within the two top TiO2 layers are labeled from 1–8. O and Ti atoms are represented by red and gray spheres, respectively. Dashed circles indicate the position of Ti atom 5 in the unreconstructed (1x1) unit cell, which is shifted to the position (1/2, 1/2) as indicated by the open arrow (c) Perspective side view of the structure.*

structure to the metallic character of the surface and to the appearance of large magnetic moments up to $2\mu_B$ located at Ti and O atoms.

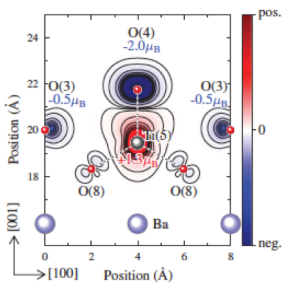

Figure 2. *Spin density and magnetic moments calculated for BTO(001)-(2x1).*

Figure 2 shows the calculated spin density contour plot in the plane defined by the [100] and the [001] direction. In detail, the atoms Ti (5) and O (4) are antiferromagnetically coupled characterized by magnetic moments of +1.3 μ_B and -2.0 μ_B, respectively. The magnetic interaction in the Ti(5)-O(4) bond is strongly localized. By contrast, O atoms (3) form a magnetic chain along [010] with local magnetic moments of -0.5 μ_B. The total energy calculations also reveal that the surface is magnetic with the total magnetic moment of 1.5 μ_B.

4.1.2 Catalysis

During the last years of the last century the first beamline responsible of ID03 at the ESRF was exploring the capabilities of surface diffraction techniques applied to the area of surface chemistry by designing one of the first reactors to study gas-solid surface reactions in batch mode. Since then this field experimented a big development with the design of small volume reactors able to work in controlled gas flow rate mode to simulate the working conditions, or as close as possible, of real catalysts. For this purpose GIXRD techniques were combined with mass spectrometry to study both the surface structure of model type of catalysts under reaction conditions [26]. The focus was mainly made on oxidation and reduction reactions with the aim of an atomic scale understanding of the **surface structure of the active phase** and the reaction pathway. In this way, this field is nowadays ready to accept studies on more complex materials with the goal to facilitate the development of multifunctional catalytic coatings and/or membranes with enhanced activity and selectivity. The type of desired flow reactor chamber is shown in the figures below [2].

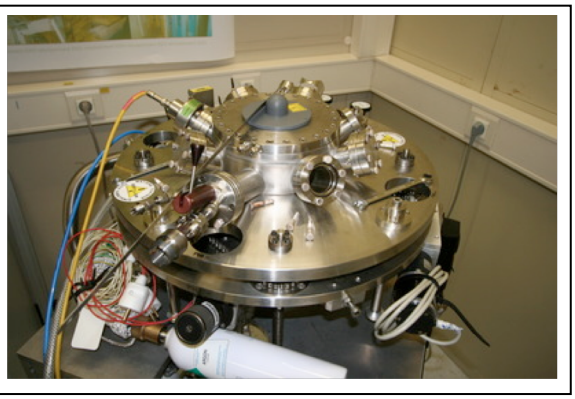

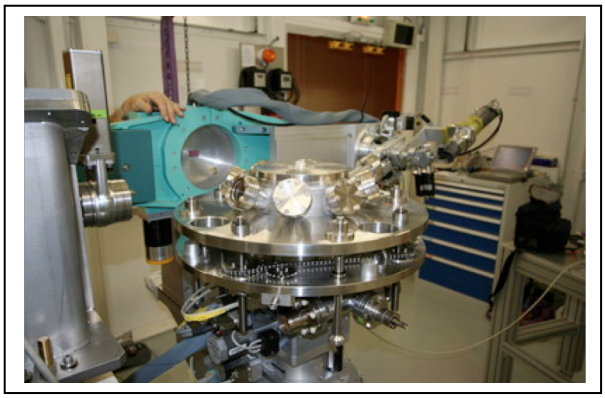

This flow reactor is equipped with in-situ UHV surface preparation tools that allow the study of reactions in real time and closer to real industrial conditions. The reactor is also equipped with a gas line having an automated system of gas flow controllers that improves the data acquisition procedure and gives the ability to follow the catalytic reaction from the beginning. This chamber is formed by a lower and an upper part. The lower part is the UHV section whose upper big flange is holding the UHV tools and is equipped with Ion Sputter Gun for sample surface preparation, Residual Gas Analyzer, RGA and Electron beam evaporator. The big flange can be moved up and

down with respect to the sample position. When up, the sample is in UHV conditions and can be prepared with standard UHV tools. When the flange is down the region around the sample is sealed off having a small reactor volume (15 mL). Gases can flow through two capillaries. UHV conditions are preserved in the bottom section all the time [2].

The gas system has four mass flow controllers at the gas inlet. This allows mixing exact proportions of desired gases. It will be remote controlled via beamline control software.

Examples

4.1.2.1 Stepped surfaces

Atomic steps on catalyst surfaces are often considered to be special, active sites for heterogeneous catalytic reaction. In 1925 they were already proposed as possible active sites in surface chemical processes [27]. They enable enhanced binding of reactant molecules [28-30] and exhibit enhanced activity for bond breaking [31-34]. The early papers from the Somorjai group [30,35] suggested that surface steps in Pt surfaces were active sites for C–C and C–H bond breaking. Further published literature provides a variety of examples of dissociation of molecules chemisorbed at step sites [36-40]. Consequently, steps play on the dissociative chemisorption of gas molecules.

Surface chemical reactions are intrinsically more complex tan chemisorption processes since they involve additional elementary steps. This additional complexity blurs the precise role of steps in many cases. The intuitive idea that the presence of steps always increases the reactivity can be questioned. This is technically difficult to address since only a few techniques can provide direct structural information under reaction conditions. Literature documents that (i) the turnover frequency (TOF) on the dehydrogenization of cyclohexane on stepped Pt surfaces did not occur on the surface with the highest density of steps [41]; (ii) atomic oxygen reacts more rapidly with the CO adsorbed on the terraces that on the steps [42]; (iii) thermal desorption experiments on several adsorbed gases on stepped surfaces don't show clear evidences that surface steps or kinks have any effect on catalytic activity [43]; (iv) CO adsorbed on the terraces was more effective in producing CO_2 than CO on the steps [44-47]. However, Au particles seem to be an exception since the results are opposite [48]. Low coordinated Au atoms were associated with high TOFs since small Au particles (2–4 nm) exhibited TOFs ~ 100 times larger than particles of 20–30 nm in size.

Experiments on the oxidation of CO to CO_2 on Pd(001) surfaces exposed to 500 mbar of O_2 and 25 mbar of CO investigated with surface X-ray diffraction in operando conditions [49], evidenced an oscillatory reaction rate and surface morphology. The surface was periodically changing from metallic to oxidized, and the production of CO_2 was also oscillating in phase with the structure of the surface. High reaction rates corresponded to oxide surfaces and low rates to metallic surfaces. The high reaction rate was associated with a broadening of the diffracted peaks indicating an increase in surface roughness that was interpreted as being due to an increase in the density of surface steps. From these observations, it was concluded that surface steps had a key role on the reactivity.

X-ray diffraction techniques permit consequently the simultaneous evolution of the surface structure of the catalyst and its surface reactivity by monitoring in operando conditions (i) the intensities of some reflections becoming to the active phases of the catalyst, (ii) the gas partial pressures of the products derived from the reaction and (iii) the temperature in the stages previous, during and after the chemical activity of the catalyst.

It has been recently proved in a stepped Pt(977) surface that under reaction conditions at near atmospheric pressures the surface is faceted and consists of (111) and (977) areas that have to coexist with rough or step bunched areas to keep the mean surface orientation (Figure 1). The maximum density of (977) areas and hence of atomic steps occurred when the reactants had the stoichiometric proportion (two COs per one O_2 molecule). Excess of CO or O_2 over the 2:1 nominal

ratio in the gas mixture caused an increase in the proportion of (111) facets and a decrease in (977) revealing the disappearance of some monoatomic steps. If the gas proportion was returned back to the stoichiometric ratio, the (977) facet increased, i.e., steps were regenerated. This process was reversible [50] (Figure 2).

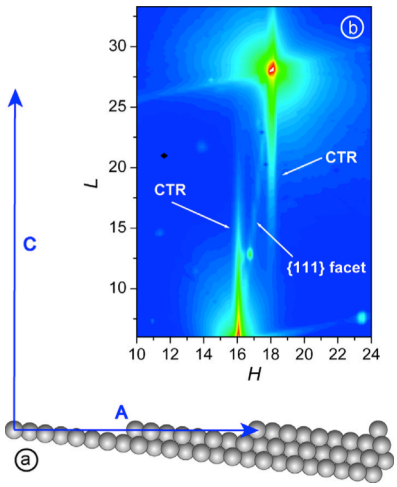

Figure 1. *(a) Side view of the 977 surface and representation of the A and C vectors in direct space. C is perpendicular to the 997 planes and A has a length twice the step separation. (b) Diffracted intensities in a portion of the plane (H,L) at K = 0 in reciprocal space. The H and L axes are parallel to vectors A and C respectively. The intense red spot at (H,L) = (18,28) arises from a Bragg reflection from the bulk of the crystal. The diffuse intensity streak emanating from the Bragg reflection, parallel to the L axis, is a crystal truncation rod (CTR) of the 977 surface plane. At (H,L) = (16,5) there is another Bragg reflection which tail is visible in the lower part of the figure. Again, its associated diffraction rod from the stepped surface parallel to the L axis is noticeable. In addition, an inclined diffuse intensity line connecting the two bulk Bragg reflections is visible. It corresponds to a diffracted rod from 111 surface planes indicative of the existence of surface 111 facets. (For interpretation of the references to colour in this figure legend, the reader is referred to the web version of this article.)*

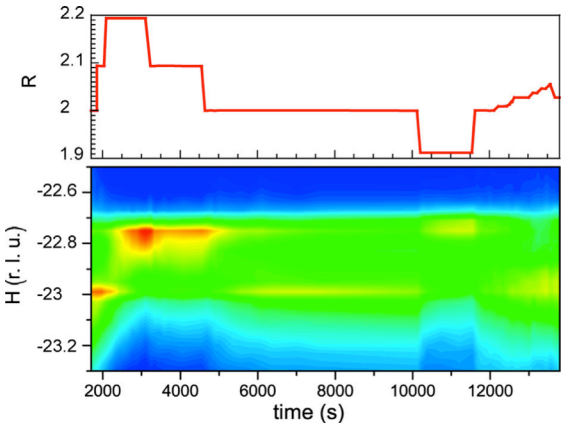

Figure 2. *Top panel: The CO/O_2 gas mixture was varied as a function of time around its stoichiometric 2/1 value ($R = PCO/PO_2 = 2$). Starting with a stoichiometric mixture, it was changed to $R = 2.2$ at $t \sim 2200$ s (CO rich mixture) in two steps and subsequently it was set again to the stoichiometric $R = 2$ value at $t \sim 5000$. At $t \sim 10{,}000$ s the gas mixture was changed to O_2 rich ($R = 1.9$) and finally was set again to the stoichiometric proportion followed by very small changes to a slightly CO rich mixture. Bottom panel: Temporal evolution of the diffracted intensity while the changes displayed in the top panel were being carried out. The diffraction pattern shows a portion of reciprocal space where K and L are fixed at 1 and 8 respectively while H is varied. The intensity H = -23 arises from the surface monoatomic steps. The colour code ranging from blue to red denotes increasing intensities. The intensity at H ~ -22.7 arises from 111 surface facets. At the start of the experiment, the intensity from the monoatomic steps is pronounced and it fades out when the gas mixture is made CO rich while the intensity from the facets that was initially low clearly develops. When the gas mixture is set back to the stoichiometric proportion (near t = 5000 s) the intensity from the step increases again while that of the facet strongly decreases. Subsequent change to an oxygen rich mixture (t ~ 10,000 s) decreases again the intensity from the steps in favour of the facets. Finally, the intensity from the steps reappears when the gas mixture is returned to the stoichiometric value. The linear colour scale ranges from (2.8 to 6.4) x 10^4 photons/s (red is most intense).*

4.1.2.2 Catalysis and GISAXS from nanoparticles

Metal nanoparticles dispersed on substrates are standard systems for catalysts of gas phase reactions. The nanoparticles (NPs) are small crystallites exposing several low index faces to the reactants. It is known since several years that the surface morphology of metal particles may change during catalytic reactions. They may aggregate, change their shape or become storage media of reactant atoms for example forming an oxide in an oxidation reaction [51,52]. These and other possible changes complicate the understanding of the fundamental mechanisms determining the reaction rate. X ray diffraction is a well adapted tool to investigate the morphology of nanoparticles since it provides characteristic signatures of their shape. As an example the work of Nolte et al. [53] investigated the oxidation of CO to CO_2 at elevated temperatures catalyzed by Rh nanoparticles on an oxide substrate.

Figure 1 illustrates the basic idea.

The shape of the Rh NPs consists of low index faces having the (001) face in contact with the substrate and the (100) and (111) facets in the sides of the NPs. The 2D diagram of such NPs would consist of an intense (111) Bragg reflection and on diffuse scattering rods emanating from this reflection, as indicated in the previous Figure, and with the [001] reciprocal space direction oriented perpendicularly to the surface substrate. The directions and intensities of these diffuse scattering rods allow monitoring the changes in morphology of the particles during a chemical reaction. The intensity evolution of these reflections during the oxidation process revealed the change of the shape transformation of the NPs by increasing the area of the side and top facets upon oxidation. This process is reversible, so the original shape of the NPs is recovered when the surface oxide is removed by CO exposure.

GISAXS is also suitable for the same purpose and in some cases may be more flexible than wide-angle diffraction shown before.

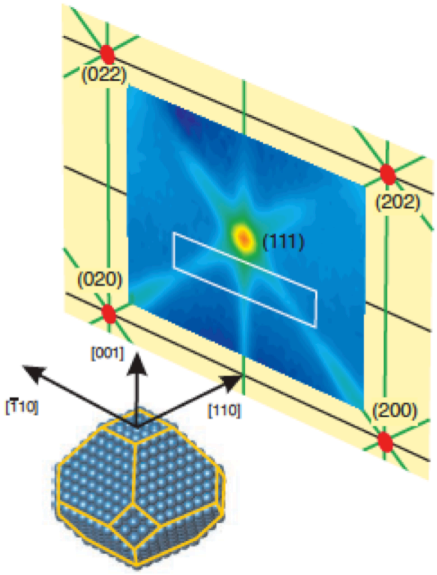

***Figure 1**. 2D diffraction diagram around the (111) Bragg reflection from the Rh nanoparticlen depicted in the figure.*

A recent experiment done at ID3 (ESRF), still in the process of being analysed, consisted in investigating the gas phase oxidation of CO to CO_2 in an enriched oxygen atmosphere using catalyst Pd NPs resulted in an oscillatory reaction rate [54]. These particles, 15 nm sized, were deposited on an aluminium oxide substrate. The reaction conditions were established at a gas pressure of 0.5 atm and a temperature close to 600 K. The diffraction experiment was set to an X-ray energy of 18.0 keV and grazing angle conditions to make possible the acquisition of GISAXS patterns with a 2D pixel detector located at 540 mm from the sample and was performed in operando conditions.

During the experiment, both the partial pressures of CO and CO_2 using a mass spectrometer and the variations of the sample temperature were monitored simultaneously during the reaction. A movie was recorded displaying these three experimental variables (gas pressures and intensities). Figure 2 (in next page) depicts three illustrative instants of the reaction. The CO pressure is displayed in red and that of CO_2 in blue. Under the conditions of the experiment the production of CO_2 is oscillatory with time between a high and a low reactivity regimes, and consequently the concentration of CO is also oscillatory with opposite phase, i.e, a maximum of CO_2 production

corresponds to a minimum of CO. High/low reactivity regimes (HRR / LRR) are associated to high/low CO_2 production regimes.

As it may be observed in the GISAXS pattern of the middle image (Fig. 2), the maximum of reaction rate is associated to a diffuse diffraction that extends continuously along the surface normal (vertical direction in the figure) with decreasing intensity going from the bottom to the top part of the diagram. However, when the reaction rate is minimum (left or right images: CO maximum and CO_2 minimum) the GISAXS pattern displays along the surface normal a distinct two lobed pattern. This scenario is repeated in many reaction cycles (Fig. 2). The two lobes resemble diffraction spots along the surface normal and they could be due to constructive interference between the upper part of the facet of the particle parallel to the substrate and the facet of the particle in contact with the substrate. From the geometry of the experiments the distance between both facets results to be 9.6 nm approximately.

Although the analysis of the data is still in progress, the above experiment illustrates the possibilities of the technique for investigating the changes of the catalyst *in operando* conditions.

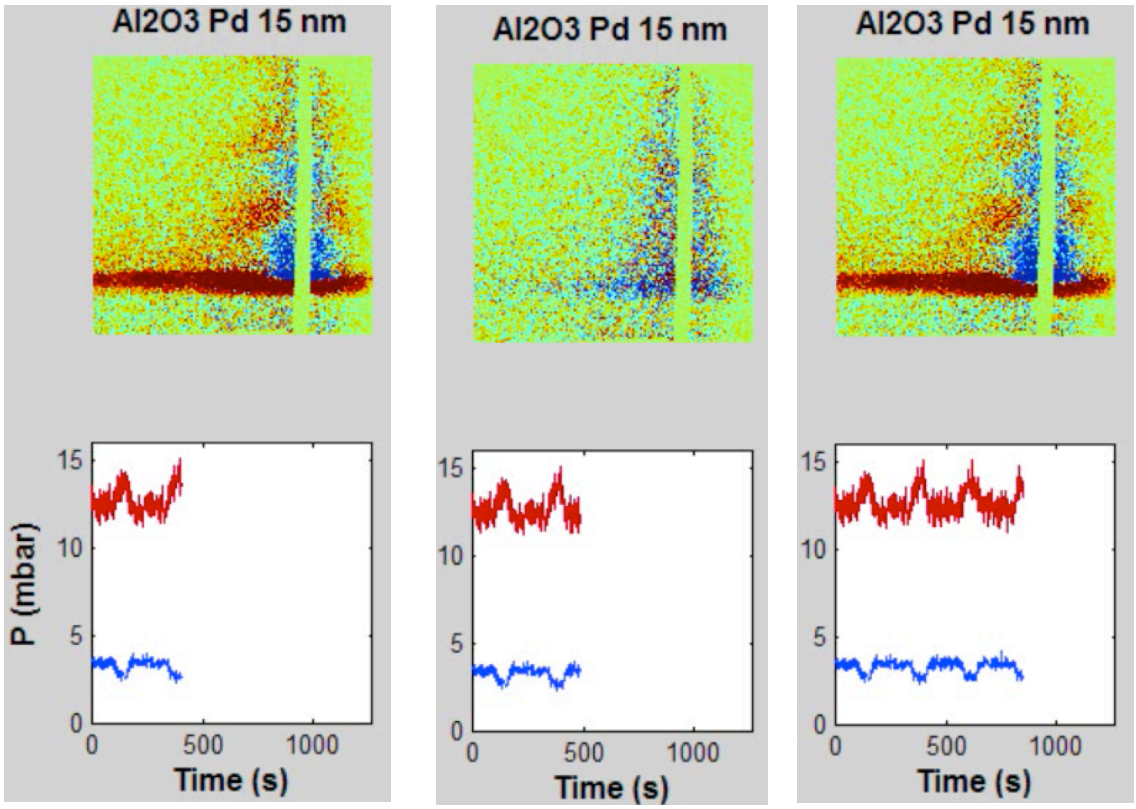

Figure 2. *Three instants during the CO oxidation reaction with Pd NPs. Red and blue curves show CO or CO_2 gas pressures evolution during the reaction, indicating high (CO_2 maximum) or low (CO_2 minimum) reaction rates. Left and right (middle) images correspond with low (high) reactivity periodes of the catalyst during the reaction.*

4.1.3 Electrochemistry-Corrosion and its protection

In a sense, corrosion can be viewed as the spontaneous return of metals to their ores; the huge quantities of energy that were consumed in mining, refining, and manufacturing metals into useful objects is dissipated by a variety of different routes. The especial characteristic of most corrosion processes is that the oxidation and reduction steps occur at separate locations on the metal. This is possible because metals are conductive, so electrons can flow through the metal from the anodic to the cathodic regions. The presence of water is necessary in order to transport ions to and from the metal, but a thin film of a moisture can be sufficient. A corrosion system can be regarded as a short-circuited electrochemical cell in which the anodic process starts when the metal is under stress (at a bend or weld) or isolated from the air (where two pieces of metal are joined or under loosely-adhering paint film). The metal ions dissolve in the moisture film (i.e., $Fe \rightarrow Fe^{2+} + 2e$-) and the electrons migrate to another location where they are taken up by a depolarizer. Oxygen is the most common depolarizer ($O_2 + 2H_2O + 4e^- \rightarrow 4OH^-$). The resulting hydroxide ions react with the Fe2+ to form the mixture of hydrous iron oxides known as rust. To prevent corrosion, most metals are covered with a thin oxide film, which inhibits anodic dissolution. When corrosion does occur, it sometimes hollows out a narrow hole or pit in the metal. The bottoms of these pits tend to be deprived of oxygen, thus promoting further growth of the pit into the metal.

The economic aspects of corrosion in the U.S. alone exceeded in 2013 $1 trillion, approximately 3.1% of GDP (Gross Domestic Product), so from here the relevance of the scientific and industrial interest on this area.

Electrochemical processes such as anodization and cathodic deposition are used in a number of industrial applications for improved performance of everyday materials such as aluminium and many other metals. As a result, the improvement of the corrosion resistance by the generated surface films may have significant economic, competitive and social implications. Moreover, electrochemical techniques have been widely used for investigation of corrosion resistance of various types of surface films.

The common key question in these type of studies is the role of the thin passive film (oxide/hydroxide, a few nanometers in thickness) formed on the alloy surface under ambient environments or corrosive conditions, whereas the information about such thin films obtained from traditional ex-situ analyses are not really relevant and sometimes confusing. It is expected that the new information of the thin surface films obtained by integrated in-situ electrochemical, synchrotron analyses and electrochemical impedance spectroscopy (IES) will lead to a great advancement in corrosion science and also in material science and engineering.

A prototype of Kel-F electrochemical cell is proposed in the figure below [55]. The electrode/substrate is mounted at the end of a holed Kel-F rod for electrical contact. The Mylar window is held in place by an O-ring that clamps it to the Kel-F cell body. The tube and substrate can be adjusted towards the Mylar window by means of a micrometer screw mounted on the male substrate joint. Inlet and outlet lines to the cell can be opened/closed by valves to apply over and under pressure to the interior of the cell.

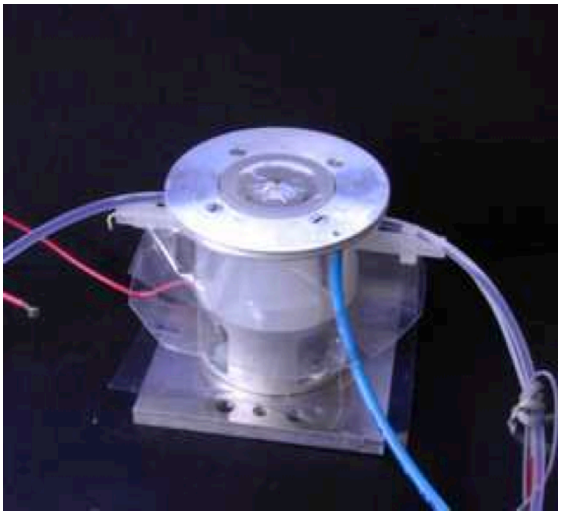

Examples

4.1.3.1 S on Au(111)

The understanding of the surface structure of the first atomic layers of crystals attracts considerable attention because their atomic arrangement determines the electronic properties and reactivity of surfaces. The ability to control the surface structure at the atomic level is a crucial point, not only for designing new materials for catalytic applications, but also in the development of the rapidly developing wide field of nanotechnology [56].

Sulphur (S) and S-containing organic molecules adsorbed on metals represent very interesting systems, as S is a well-known poison in heterogeneous catalysis [57], and S-containing organic molecules, such as alkanethiols, play a key role in nanotechnology applications [58]. Therefore, these species adsorbed on well-defined metal surfaces, particularly the Au(111) face, are usually taken as a model system for interfacial science research [59].

The combination of electrochemistry and SXRD, as well as SPM, techniques to the study of Au(111)/S electrodes in aqueous electrolytes allows to follow changes in the amount of adsorbed species induced by the electrode potential in real time [60]. Thus, it is possible to identify weakly bound S species before anodic adsorption or after cathodic stripping and to follow the kinetics of the adsorption/desorption processes in real time [61].

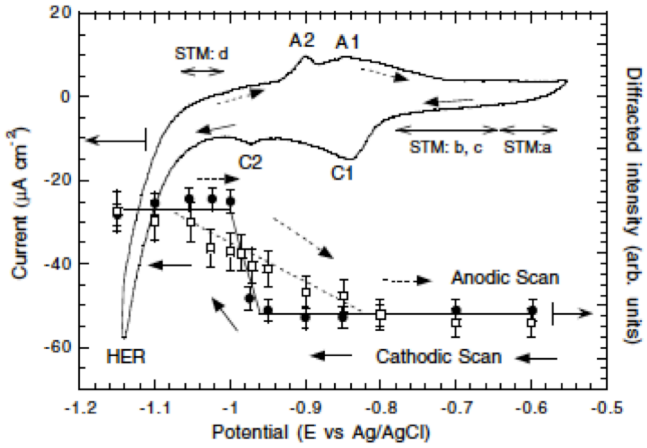

Figure 1. *(Upper curve, left axis) Cyclic voltammogram for Au(111) in 0.1 M NaOH + 10^{-3} M Na_2S. Sweep rate was 0.001 V=s. The labels STM (a) – (d) correspond to the STM images in Fig. 2. (Lower curve, right axis) Integrated diffraction intensity at (HKL) = (1 0 2.5) as a function of the applied voltage in a cathodic (solid circles) and anodic scan (empty squares). The lines are fitted to the data as a guide for the eye. Dotted arrows indicate anodic scan direction, and solid arrows cathodic scan direction.*

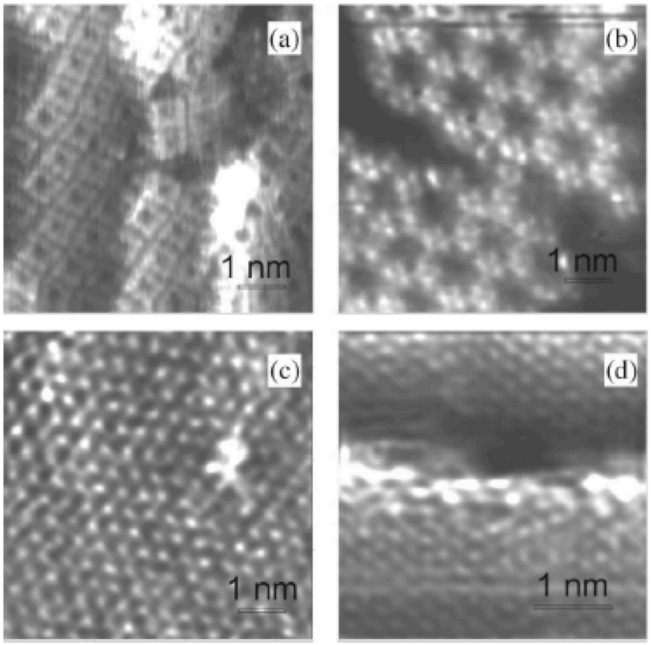

Figure 2. *In situ atomic resolution STM images recorded at electrode potentials shown by the arrows in Fig. 1.*

Figure 2(a) indicates that the main species on the surface are S octomers (S8) in the range (-0.65 V < *E* < -0.55 V), Figure 2(b) S trimers (-0.78 < *E*<-0.65 V), Figure 2(c) at -0.78 V S8 and S3 species coexist and are slowly transformed into monomeric S and a small fraction of the S atoms go to solution while the remaining ones rearrange slowly into a (3 x3) *R*30º lattice [62]; at *E* = -1.05 V a 1x1 Au(111) surface structure is observed. Only a few S atoms remain adsorbed at step edges [62].

In Figure 3 the (1 0 *L*) CTRs obtained for *E* -0.76 V and *E* -1.05 V, corresponding to the

regions of the voltammogram where the S layer is on the surface and after it has been stripped to the solution, respectively. The absorption/desorption process is reversible. Figure 4 shows the intensity at the CTR minimum with time, while cycling the potential. The starting potential was -0.476 V, and then it was scanned at a speed of 0.005 V/s and reversed when *E* reached the value of -1.1 V. The arrows indicate the time where the voltage scan is reversed (i.e., changed from *C* to *A* direction). S atoms leave the surface to the solution and reattach at the surface, and after each complete process the diffraction intensity recovers its original value, proving the absence of roughening of the Au(111) surface, which appears to react completely elastically. The system can be cycled some tens of times before observing irreversibility associated with a roughening of the surface. Similar scans made in 0.1 M NaOH (in the absence of sulphur species) show no such change.

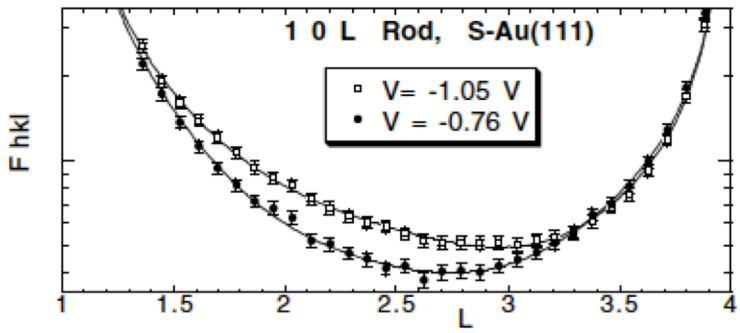

Figure 3. *(1 0 L) CTR for Au(111) in 0.1 M NaOH +10^{-3} M Na_2S recorded at two different electrode potentials. The overlapping solid lines represent the best fit. The difference between the curves is due to the presence of a S layer.*

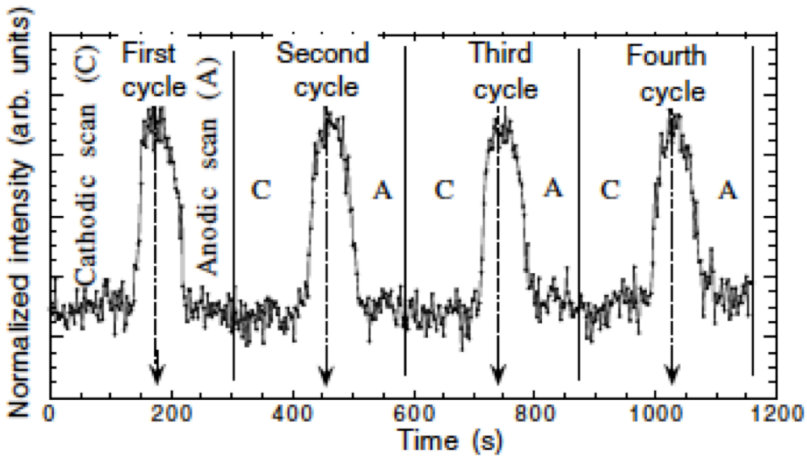

Figure 4. *Real-time measurement of the evolution of the diffracted intensity at (1 0 2.5). The diffraction peak was recorded while scanning the electrode potential at 0:005 V=s.The arrows mark the time where the scan is reversed. The starting and reversing potentials are -0.476 and -1.1 V, respectively.*

4.2. GISAXS

The elaboration of well-defined nano-organised objects demands a precise control of the growth parameters which requires by the way, the understanding of the processes related with nucleation and growth in terms of size, shape and correlation distance between islands.

The equilibrium morphology of such objects can be visualized by scanning probe microscopy (SPM) or studied by x-ray scattering. However, several phenomena on these systems show fast evolution under UHV, even at room temperature, thus demanding in-situ and in real time studies. GISAXS is complementary to SPM techniques since it provides overall information on the sample, combining the potentiality of small angle X-ray scattering (SAXS) with the surface sensitivity of grazing off-specular reflectivity.

In fact, SAXS is sensitive to heterogeneities in the electron density on a mesoscopic scale (10 - 10^3Å) so well adapted to study the particles distribution. Like grazing incidence X-ray Diffraction (GIXD), SAXS experiments can be carried out at or near total external reflection of the material [63]. It is possible to study nanostructures deposited on a flat surface or even embedded in the matrix of a thin layer and it does not even require the matrix simple and/or the deposit to be crystalline. The scattered signal is collected under grazing exit angles, in the forward direction, using a two-dimensional position sensitive detector placed perpendicular to the incident beam path. This type of detectors has the advantage to reveal directly a possible anisotropic shape of the scattering pattern that is normally related with an anisotropic spatial distribution and shape of nano-objects [64]. The Born approximation (kinematic approximation) can be used to extract the morphology and electron density of small scattering objects, which greatly simplifies the GISAXS interpretation. For large scattering objects (very small angles) and high specular substrate reflectivity (very smooth surface) however, it becomes necessary to introduce the distorted-wave Born approximation (DWBA) to take into account reflections and eventually multiple scattering effects [65].

GISAXS can be used to determine *in situ* and *in real time* the morphology of small islands (1nm - 10nm) during growth at different temperatures, under ultra high vacuum (UHV), from the very beginning of the growth. The 2D scattering pattern gives access to the average lateral size, height and separation between islands (island density), and even statistic distribution of these parameters [66].

GISAXS technique needs a bright synchrotron radiation source (flux, collimation) with tunable photon energy in order to perform anomalous scattering measurements. In this case, anomalous dispersion near absorption edges enables to obtain information on the chemical composition of islands, and study segregation effects like those observed in bimetallic islanding [64]. A particularly interesting field of study is the formation of exotic particles or clusters (non-equilibrium shape, imperfect structure, nanosegregation) by ion assisted atomic deposition on amorphous substrate [64]. A precise control of the growth parameters can lead to the formation of well-defined nano-organized systems. But, to obtain the control and understanding of the process, it is necessary to follow, the cluster formation mechanisms in terms of structure, shape, size and in-plane distribution, by GISAXS and GIXRD.

In another field, self-organized islands (like quantum dots) obtained by heteroepitaxial growth (strain effect) can be studied also by coupling GISAXS and GIXRD on the same x-ray scattering apparatus [67]. As in the previous case, the structural information, obtained by GIXRD can be complemented with respect to the ordering effects (lateral and vertical) induced by strain field, by GISAXS (shape, size and orientation symmetry). In summary, an experimental end-station allowing in-situ (UHV, temperature or gas pressure) and in-real-time (growth or reaction kinetic) grazing incidence X-ray scattering (GISAXS and GIXRD) will open brand new opportunities to nanostructured surfaces studies and/or nano-objects dispersed on a surface. Moreover, these two diffraction techniques can be combined in reactivity type of experiments, using a flow reactor chamber as that proposed for catalysis [2], in order to follow simultaneously, substrate structure and

evolution of the different phases with catalytic activity, surface morphology evolution and/or that of the nanoparticles in case of being present on it, as well as the evolution of the inlet and product gases derived from the reaction process.

4.2.1 Examples

4.2.1.1 TiO2 supported gold nanoparticles

It is well known that gold nanoparticles supported on TiO_2 act as a catalyst for CO oxidation, even below room temperature, however, the origin of this catalytic activity remains still under debate. It is known the dependence when the particle size decreases with the electronic properties of the nanoparticles (NPs) and consequently with their catalytic performances. The current state-of-the-art of the diffraction techniques offered by 3rd generation synchrotron radiation facilities in the study of the catalytic response in-operando conditions on these types of materials permits to identify the dependence of the NPs morphology as well as their atomic structure as function of their catalytic activity by means of Grazing Incidence Small Angle X-ray Scattering (GISAXS) and Grazing Incidence X-ray Diffraction (GIXRD), respectively [68,69]. In the present example [70], the characterization of gold nanoparticles (GNPs) supported on TiO_2(110) during CO oxidation was performed by recording at the same time the catalytic activity, GISAXS patterns and GIXRD data. Previous results on the reaction rate dependence with GNPs size can be found in [71,72]. The maximum reaction rate is achieved for GNPs size of about 2nm. The analysis of the evolution of the GNPs' atomic-scale structure and morphology around this maximum should yield a better understanding of the key parameters involved in their catalytic properties. Moreover, in contrast to atomic structures determined by X-ray measurements performed on powders, the use of nanoparticles epitaxially grown on TiO_2(110) single crystal reveals information on their shape, their atomic structure and their lattice parameter parallel and perpendicular to the substrate surface. In this frame, GISAXS and GIXRD lead to the definition of what can be called an 'average' particle analysed in the reciprocal space and representing a wide collection of nanoparticles.

The experimental procedure [71,72] can be summarized as follows:
i) The GNPs were synthesized in an UHV preparation chamber (base pressure of $5x10^{-8}$ Pa). ii) The TiO_2(110) single crystal, used as a substrate, was first bombarded with 750 eV argon ions and then annealed at 1000 K under an oxygen partial pressure of 10^{-3} Pa in order to restore the surface stoichiometry [73]. iii) The gold nanoparticles were grown by UHV vapour deposition at 300 K from a Knudsen cell.

Once prepared, the Au/TiO_2 (110) samples were transferred under UHV into the batch reactor in order to perform X-ray and catalytic activity measurements during the carbon monoxide oxidation. The measurement procedure involved three steps; each lasting approximately two to three hours: (1) Au/TiO_2(110) was first studied in UHV ($2x10^{-7}$ Pa) at room temperature (RT); (2) then during annealing at 473 K in $2x10^{3}$ Pa of oxygen; (3) and finally during CO conversion into CO_2 that was started by adding 20 Pa of CO to the oxygen, while keeping the sample at 473 K. The CO and CO_2 partial pressures in the reactor were deduced respectively from the 28 and 44 ionization currents measured by a mass spectrometer.

The structure of bulk gold is face centred cubic (fcc) and two kinds of epitaxy relationships are usually observed on TiO_2(110) : (112)Au//(110)TiO_2 and (111)Au//(110)TiO_2, depending on the substrate temperature during the GNPs growth [74]. However, by means of GIXRD in UHV, Lazzari et al. found that these two epitaxial relationships are nearly equiproportional whatever the temperature [75]. The diffraction measurements show that the (111)Au//(110)TiO_2 epitaxy is predominant, especially under reactive conditions.

For each gold deposit, the mean geometrical parameters of the GNPs, such as the diameter D, the height H and the interparticle distance L, were deduced from the quantitative analysis

of the GISAXS patterns performed using the IsGISAXS software [76].

Figure 1 illustrates the evolution of the diffracted intensities obtained during the three steps of the experimental procedure for a sample with an equivalent gold thickness of 0.1 ML (Figures 1a and 1c) and another one with 0.5 ML (Figures 1b and 1d). Two directions of the reciprocal space are represented: parallel to the surface along H and perpendicularly to it along the rod (0 1)Au. Above 1 ML, the spectra remained independent of the environment. This behaviour can be correlated to what was deduced from GISAXS patterns measured at the same time.

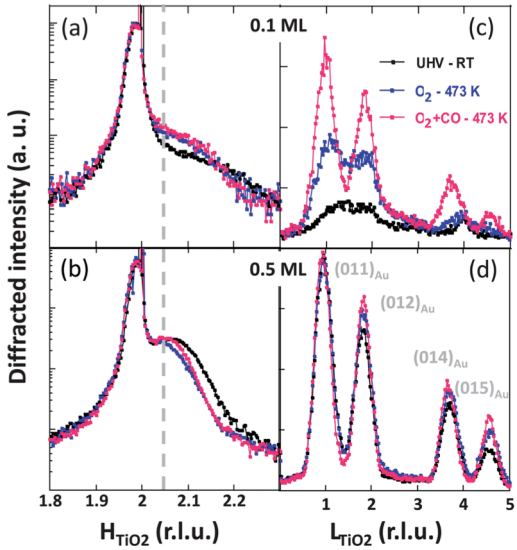

Figure 1. *Diffracted intensity: (a) and (b) along a radial scan around (2 _1 0)Au and (c) and (d) along the (01)Au rod for two samples with gold equivalent thicknesses of: (a) and (c) 0.1 ML and (b) and (d) 0.5ML during the three steps of the experimental procedure. (1) in UHV at RT (black), (2) under 2.103 Pa of oxygen at 473 K (blue) and (3) after adding 20 Pa of CO while keeping T 1/4 473 K (red). In (a) and (b) the thin peak centered at (200)TiO2 with a broad and intense foot is the TiO2 Bragg peak, the shoulder on the right is the (2 -1 0)Au Bragg peak that is expected at (2.05 0 0)TiO2 for bulk Au, as indicated by the grey dashed line.*

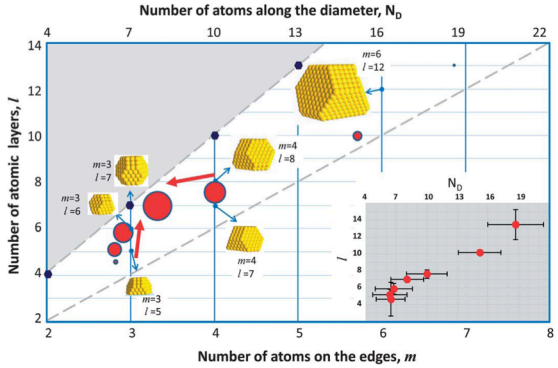

Figure 2. *Reaction rate of the GNPs as a function of the size of the corresponding truncated cubo-octahedron with, on the vertical axis the number of atomic layers l, and on the bottom horizontal axis, m, the number of atoms on the edges and on the upper one, ND, the number of atoms along the diameter; the scales for l, ND and m are proportional to the value of dt, d// and 3d//, respectively. The red spots are proportional to the reaction rate for CO oxidation, as deduced from the experimental data. They are located at the m and l values deduced from the mean D and H, as explained in the text. Schematic representations of cubo-octahedrons are given for several couples of (m, l) pointed by the blue arrows (see text for the red arrows). The couples (m, l) corresponding to complete cubo-octahedrons are marked by dark blue diamonds. On the lower grey dashed line, the aspect ratio H/D is 0.5 and it is 0.8 on the upper one, that crosses the dark blue diamonds. The part of the diagram above it has been shaded since the corresponding (m, l) couples cannot be assigned to the cubo-octahedral geometry. In the insert, the experimental data were also plotted as a function of l (vertical axis) and ND (upper horizontal axis) with their error bars calculated from the width of the Gaussian distribution of the GNPs size given by the GISAXS analysis.*

4.2.1.2 Drying Temperature-Influence on the Structural Evolution of Bulk-Heterojunction of Polymer-Fullerene Solar Cells

Organic bulk heterojunction (BHJ) solar cells comprising conjugated polymers (as electron donor) and fullerene derivatives (as electron acceptor) deposited from solution make low cost photovoltaic-energy conversion feasible [77,78]. The active layer of BHJ solar cells comprises an interpenetrating network of polymer and fullerene domains that forms during deposition and drying. The energy-conversion process involves the creation of excitons upon light absorption, which are dissociated into free charges at the donor/acceptor interface and are further transported towards the respective electrodes. Thus, for a given combination of donor and acceptor materials, the efficiency of a BHJ critically depends on its nanoscale structural properties.

The P3HT polymer shows crystalline order with a $\pi - \pi$ stacking of the molecules (important for ensuring sufficient hole-carrier mobility for charge extraction [79-81]), a relative orientation of the P3HT crystallites (due to their anisotropic electrical charge mobility) and the distribution of amorphous P3HT regions (which are expected to affect the electronic interconnection among P3HT domains [79,82]). The relative importance of the many implied microstructural features on solar-cell performance and the factors determining the development of specific structures during blend solidification are still under debate.

GISAXS is an excellent tool to observe in real-time the emergence and evolution of the blend P3HT:PCBM (poly(3-hexylthiophene) (P3HT) and [6,6]-phenyl-C 61 butyric acid methyl ester (PCBM)) microstructure as function of the surface temperature and solvent evaporation [83].

For the in situ study of the structural evolution during drying, a solution of P3HT and PCBM dissolved in dichlorobenzene (DCB) was doctor–bladed on poly(3,4–ethylenedioxythiophene): poly(styrenesulfonate) (PEDOT:PSS) coated glass substrates at substrate temperatures of 10 ºC, 25 ºC, 40 ºC, and 80 ºC. Immediately after coating, real–time X-ray scattering data was collected simultaneously with a two-dimensional (2D) Mar–CCD (charge-coupled device) camera and a reflectometer for measuring the film thickness during evaporation (Figure 1).

Figure 2a–d show 2D X-ray scattering patterns of the dried P3HT:PCBM blends after solvent evaporation at drying temperatures of 10 ºC, 25 ºC, 40 ºC, and 80 ºC. The vertical and horizontal axes correspond to the components of the momentum-transfer perpendicular (q_z) and parallel to the sample (q_{xy}), respectively (also denoted out–of–plane and in–plane directions). The diffraction ring marked in Figure 2c corresponds to randomly oriented PCBM aggregates [84,85].

As the solvent evaporates, the structural evolution is further analyzed as depicted in the Figure 2e–g. An estimation of the P3HT "overall crystallinity" from the (100) reflections has to include the azimuthal intensity distribution which accounts for all differently oriented crystallites. Therefore the X-ray scattered intensity was integrated between two concentric circles containing the (100) Bragg peak (as shown in the inset of Figure 2e) and plotted as a function of the drying time (Figure 2e).

The time evolution of the mosaicity is shown in Figure 2f. The mosaicity was obtained from the full width at half maximum (FWHM) of the angular spread of the P3HT (100) intensity fitted to a Lorentzian curve. The plots of the (100) intensity as a function of azimuthal angle are given in Figure 2g for different drying temperatures. In Figure 2f it can be seen that the microcrystalline grains exhibit a similar orientation distribution (mosaicity of 7 º–10 º) in the early stages of P3HT drying at all substrate temperatures. As solvent evaporates, there is a larger fraction of misaligned crystallites, which is significantly larger for lower temperature drying and results in the highest mosaicity of 25 º for the film dried at 10 ºC. Additional measurements at the Bragg condition with a 2D detector confirmed this trend.

The analysis of the X-ray experiment provides insight into the effect of the substrate temperature on the structural evolution of doctor-bladed P3HT:PBCM blends in the transition from wet to solid. It shows that active-layer drying at lower temperatures (10 ºC) leads to a good $\pi - \pi$ P3HT assembly, a broader orientational distribution of P3HT (enabled by the slow crystallization

kinetics), and a restricted phase separation of P3HT and PCBM (due to lower molecular mobility) that results in a better nanomorphology with a finer interpenetrating network

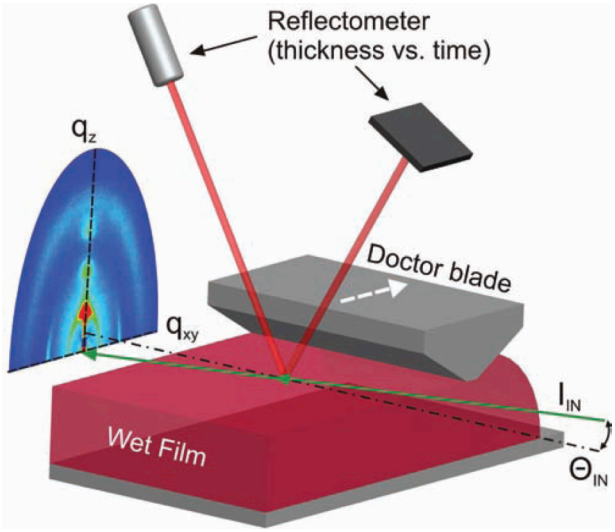

Figure 1 . *Schematic of the experimental set-up for real-time grazing incidence X-ray scattering and laser refl ectometry.*

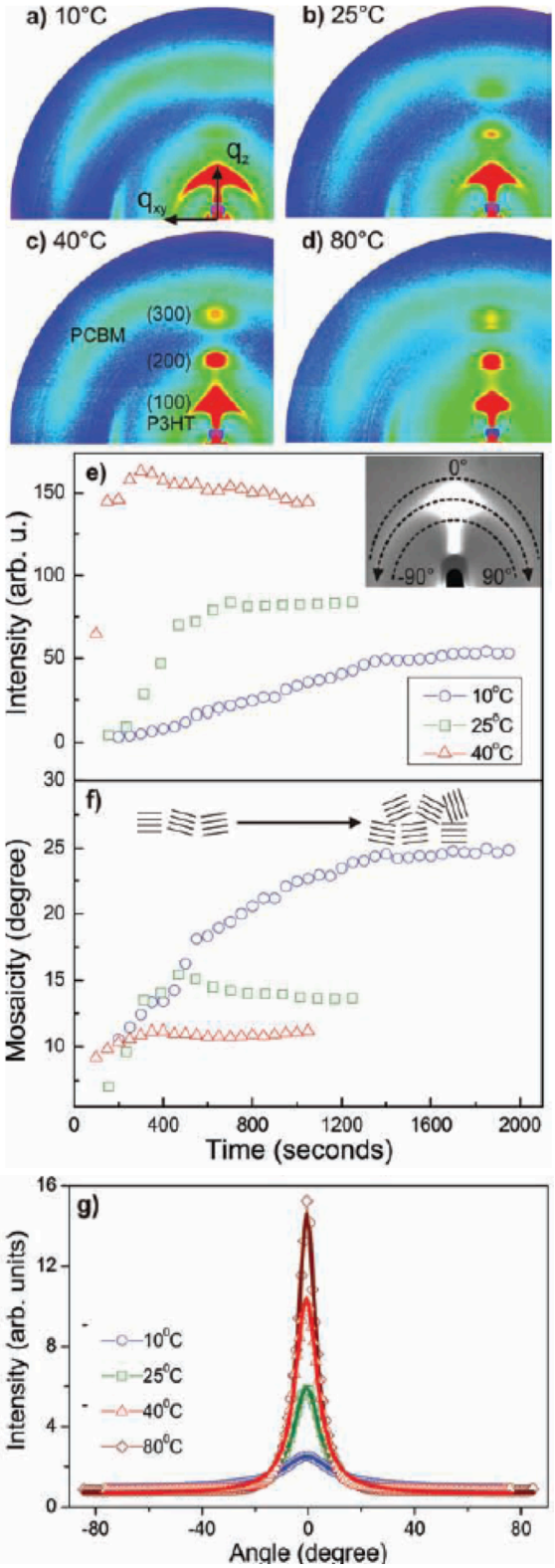

Figure 2 . *2D diffraction pattern of P3HT:PCBM in DCB dried at substrate temperatures of a) 10 ºC, b) 25 ºC, c) 40 ºC, and d) 80 ºC on glass substrates/PEDOT:PSS applied by doctor-blading. Evolution of e) P3HT (100) integrated intensity and f) mosaicity of P3HT with drying of the solvent at substrate temperatures of 10 ºC, 25 ºC, and 40 ºC. The evolution data for 80 ºC is not plotted because the fi lm dried immediately upon coating. g) Azimuthal distribution of the (100) intensity.*

4.3 COHERENCE

The use of X-rays in diffraction has conventionally yielded the average structure of the ensemble, where the coherence length of the domains on the sample is inversely related to the width of the diffraction peaks. In such measurements, the coherence of the x-ray beam has not been a dominant factor. The advent of new-generation synchrotron sources with small source dimensions and the use of narrow band pass insertion devices have ensured that x-ray diffraction with coherent beams has open up a whole new range of studies that nowadays are well established. The potential of using a coherent source of x-rays in diffraction experiments has been experimented a strong development during the last years only recently been realised with some preliminary experiments carried out at the European Synchrotron Radiation Facility (ESRF) and the Advanced Photon Source (APS). Several types of measurements and analysis have been identified including the reconstruction of the shape of nanocrystals due to oversampling [86] and the determination of dynamical processes by observation of x-ray speckle [87]. The first of these requires that the size of the coherent beam closely match that of the crystal, resulting in diffraction features with fringes arising from facets. The 'phase problem' usually associated with x-ray diffraction is overcome, as the pattern is oversampled by more than a factor of two relative to the Nyquist frequency. Inversion is therefore possible to produce a two-dimensional projection of the crystal shape.

The scattering of a fully coherent x-ray beam from an object gives rise to interference effects in the scattered beam. In the near-forward scattering direction, the phase differences between the waves traversing different parts of the object enable imaging of the object in *phase contrast.* At larger scattering angles, the interferences (the *speckle* pattern) provide us with information on its shape and internal structure on a length scale much shorter than is accessible with visible light. The high contrast of the speckles and their fine, diffraction-limited, graininess are essential for a wide range of applications at optical wavelengths [88] including the new laser optical mouse. As far as spatial coherence is concerned it can be improved by spatial filtering of the main beam with a pinhole, although at a considerable loss of power. This has enabled the development of a large number of X-ray speckle-based techniques like X-ray photon correlation spectroscopy (XPCS) or coherent diffraction imaging [89-92].

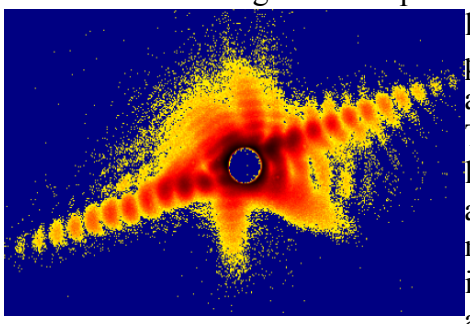

The retrieval of the object's real-space structure from the observed interference pattern is known as *coherent diffractive imaging* (CDI) or lensless imaging, which can be regarded as holography without a reference beam. CDI is a technique that uses incident coherent x-ray beams, among others, and permits the 2D or 3D image reconstruction of diffracted patterns scattered from objects at nanoatomic scale as nanotubes nanocrystal defects, potentially proteins, and more.

CDI is a technique for 2D or 3D reconstruction of images obtained from objects at nanoatomic scale such as nanotubes nanocrystal defects, potentially proteins, and more. The recorded pattern is then used to reconstruct an image via an iterative feedback algorithm. Effectively, the objective lens in a typical microscope is replaced with software to convert from the reciprocal space diffraction pattern into a real space image. The advantage in using no lenses is that the final image is aberration–free and so resolution is only diffraction and dose limited (dependent on wavelength, aperture size and exposure). A simple Fourier transform retrieves only the intensity information and so is insufficient for creating an image from the diffraction pattern due to the phase problem.

One milestone of this technique is its application to crystalline samples since them produce a periodic scattering pattern around each Bragg peak; the local scattering pattern contains information about the shape and the strain of the crystalline sample. This information is encoded through a Fourier transform of the projected complex electron density of the sample into the direction of the Bragg peak. The purpose of the technique is the measurement of the coherent scattering pattern around a certain Bragg peak. The diffraction pattern can be measured at any of the possible Bragg

peaks, depending on the orientation of the sample. If multiple diffraction patterns around a Bragg reflection are acquired, both the 3D shape of function and the internal strain of the nanocrystal can be obtained. This enables to measure all low frequency data in reciprocal space, which is normally missing in a coherent small angle scattering experiment. The detector measures then two types of patterns from the sample: a diffraction pattern at higher scattering angles and an interference pattern or hologram at lower scattering angles. The hologram is formed by the interference between the curved incident wave and the scattered wave from the sample. Both patterns can be combined into a single pattern for the retrieval of the sample structure at high resolution. The main advantages of this method are its rapid convergence and the ability to image a subregion in an extended sample with a single view (application to scanning a continuous sample) [93,94]. The main experimental requirement of this technique is related with the stability of the sample relative to the incident beam.

These techniques have experimented a fast development and a wide use imaging and characterizing materials and biological samples since the new third-generation synchrotron radiation facilities appeared.

4.3.1 AFM-assisted probe to μ-XRD

SPM (Scanning Probe Microscopy) techniques are used in many scientific fields ranging from biology to materials sciences. They are easy to use and can unveil many local properties of the surface. Synchrotron Radiation is used instead to probe the atomic and electronic structures of surfaces averaging over the illuminated area. In the most recent years the use of micro and nano X-ray beams is steadily increasing and the join exploitation of many SPM or SR techniques appears more and more desirable.

In micro-nano characterization it is often necessary to work on a single object whose size can vary from the micro to the nanoscale. It is then covetable to be able to perform SPM and X-ray experiments on the same single object in the same conditions and at the same time for more systematic and comprehensive exploration of the micro-nano world.

An useful integration of SPM techniques on SR instrumentation would allow adapting a compact, optic free, AFM scanning probe to an end station leaving the beamline as it is to perform indifferently diffraction or spectroscopy experiments, that is, the integration of the AFM should not modify the beamline. Moreover, the AFM tip has been used successfully to locally detect X-ray absorption and diffraction data as well as to detect the relative position of the particle respect to the beam through the alignment of the beam with the tip of the AFM [95]. These AFM instruments operate very much like a conventional AFM but with a simplified set up: unlike conventional AFMs, where the deflection of a cantilever is detected by a laser beam, AFMs based on TFs (Tuning Forks) have the added simplicity that the motion of the oscillator is detected directly by the conversion of the alternating stress field inside the quartz piezoelectric material into charge. Neither a laser nor a photodetector are necessary for the operation of this type of AFMs. This simplifies this type of AFM and makes it more robust.

The combination of X-ray diffraction (μm beam size) and scanning force microscopy setup combines complementary experimental techniques to access chemical and physical sample properties with nanometer scale resolution. While AFM probes physical properties such as sample topography, local mechanical properties, adhesion, electric and magnetic properties on lateral scales, XRD offers direct access to the local chemical composition, shape, and strain of micro/nano sized structures.

The applications of this tool combined with X-rays diffraction would probe elastic properties of individual nano/microstructures [96,97] or to follow the in-situ structural deformation of individual microcrystals or micro/nano pillars induced by the mechanical compression using the AFM tip as a nano-indenter. Moreover, the system also permits to follow both the different states of deformation induced by the applied force and the defects created during the compression process by

recording coherent three-dimensional reciprocal space maps of several Bragg reflections [98]. The beamline would be ready to implement this experimental set up if a user group is leading its development, i.e. through collaboration with the beamline staff or a Long Term Project development.

4.3.2 Examples

The next examples are possible type of experiments that could be performed in ALBA according to the characteristics of the source and to the optical instrumentation required for constructing the beamline. However, the implementation of coherent techniques will depend on both the experience of the beamline scientific staff and the ability of users for collaborating with the beamline scientists and promote the scientific and technological development on the technique.

4.3.2.1 3D imaging of strain inside nanocrystals

The ability of 3-D imaging of the ion displacement and strain inside nanocrystals has important implications in designing future materials and making new devices. Bragg CDI, pioneered by Robinson *et al*. in 2001 [99], offers the unique capability of mapping out the full strain tensor inside nanocrystals at nanometer scale resolution. Moreover, X-ray beams generated by third-generation sources of synchrotron radiation using undulators have practical levels of flux after the pinhole small enough to ensure coherence in the range of 10^9 photons s^{-1}. Figure 1 shows a schematic layout of Bragg CDI with multiple Bragg reflections from a single ZnO rod [100].

The experiment was conducted at the Advanced Photon Source using a wavelength of 1.42A°. By carefully rotating the ZnO rod, oversampled X-ray diffraction patterns were measured at six Bragg reflection directions, which are related to both the shape function of the rod and the strain inside the rod. By using the iterative algorithm described in Section II, the diffraction patterns were inverted into two parts: the reconstructed magnitudes and phases. While the reconstructed magnitudes correspond to the shape of the rod, the phases are related to the 3-D ion displacement inside the rod. This ion displacement information can be used to construct the strain tensor. Figure 1(b) shows a slice of the 3-D ion displacement field inside the ZnO rod in which the direction of each arrow indicates the direction of the displacement and the size of each arrow indicates the magnitude of the displacement [100]. Although the resolution of Bragg CDI is currently around 40 nm, utilization of more brilliant X-ray sources will be able to significantly improve its spatial resolution.

The Bragg CDI experiment in these type of systems as well as to nanometer sized samples can be performed selecting a coherent X-ray beam by a silicon (111) double-crystal monochromator, and focused to ~1.5 μm full-width at half-maximum in diameter with a pair of Kirkpatrick-Baez mirrors. The Coherence is a property that can be imposed on an X-ray beam by setting an entrance slit smaller than the transverse coherence length.

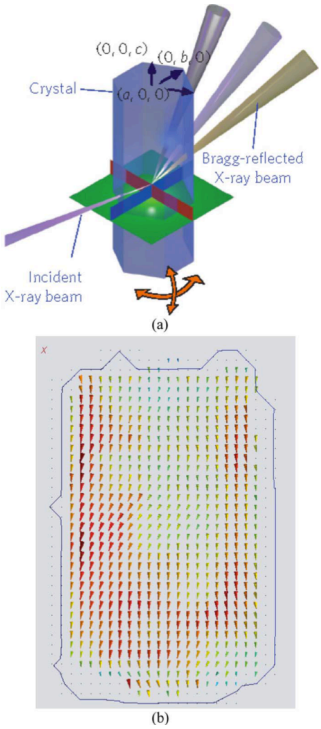

Figure 1. *(a) Schematic layaout of Bragg CDI. (b) Slice of the reconstructed 3-D ion displacement field inside the ZnO rod*

4.3.2.2 Dislocations in microcrystals

In the context of semiconductor device miniaturization down to the nanoscale, one of the most important challenges for the realization of highly efficient systems is to ensure a high crystalline quality of micro- or nanocrystals. Any deviation from the perfect atomic arrangement constitutes a ‘‘defect’’ [101] that can dramatically modify the device performance [102-104]. This is especially true for ‘‘phase’’ defects, characterized by a global shift of one part of the crystal with respect to another such as, for example, dislocations [105]. A technique that not only detects but also evaluates the number of defects in a small crystal is thus highly desirable for performing quantitative diagnostic and defect engineering studies. However, an efficient, fast, robust, and non-destructive defect characterization method has not been available previously. Transmission electron microscopy (TEM) can provide images of lattice defects, but this approach is limited to thin, electron transparent samples that often require a destructive simple preparation method. Coherent x rays provide a very powerful method able to detect and quantify small numbers of dislocations in microcrystals, without introducing any sample degradation.

Some III-V semiconductor systems shows can show changes in the mechanical properties that are attributed to a change of deformation mechanism when reducing the crystal size: elastic strain accumulated in the crystal during mechanical loading is mostly released by cracks in bulk InSb, whereas this strain is dissipated via the formation of dislocations in small crystals [106]. The coherent diffraction technique allows following the dynamic evolution during controlled formation of dislocations in microcrystals subjected to mechanical deformation up to the irreversible deformation limit (the elastic to plastic transition).

The sample is an InSb(213) single crystal, on which several InSb micropillars (6 μm in height, 2 μm in diameter) have been machined using a focused ion beam (FIB) [107].

Experimental details (Figure 1):
- Beam energy: 7 keV (λ = 1.771 Å) selected with a channel-cut Si(111) monochromator providing a band pass $\Delta\lambda/\lambda = 1.4 \times 10^{-4}$.
- Fresnel zone plates (FZPs), 200 μm in diameter and 70 nm in outermost zone width: focussed beam size at sample position: 200(V) x 500(H) nm^2.
- Selected coherent beam size (same size than transverse coherence length) before the FZP [i.e., 60(V) x 20(H) μm^2] to ensure a high degree of coherence and a reasonable flux on the sample [108-110].

The experiment consists record full 3D x-ray diffraction maps at different positions on the Pillar (Figure 2c).

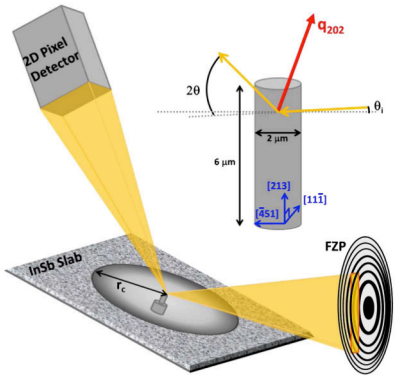

Figure 1. *Diffraction geometry*

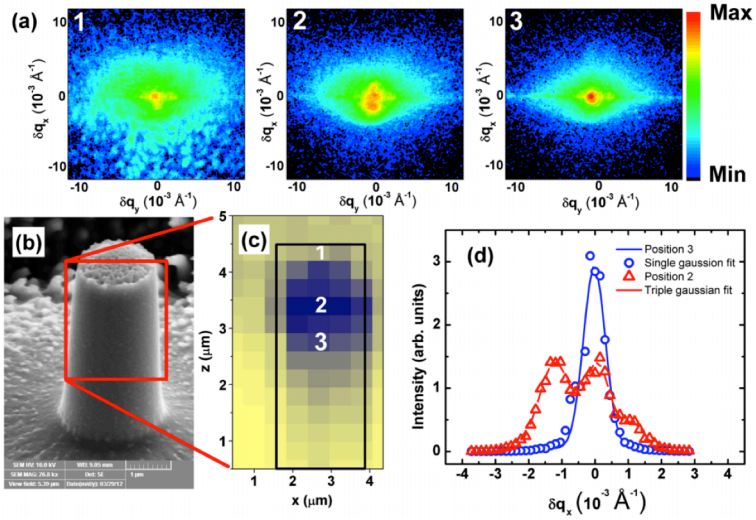

Figure 2. *Coherent diffraction patterns obtained at the maximum of the 202 reflection at three positions indexed in (c) (log intensity scale). (b) SEM image of the studied deformed pillar. (c) Scanning diffraction image obtained at the maximum of the 202 reflection. (d) Projection along qx of the peaks obtained at positions 2 and 3, and fit with Gaussian functions.*

At the very top of the pillar (position 1), the peak is very sharp and appears at the calculated Bragg position. However, many speckles appear around it. At position 2 (1.2 μm from the top), the speckles have disappeared and the central maximum is split. At position 3 (1.8 μm from the top), the peak displays a single maximum again. The projections along the q_x direction of the diffraction patterns recorded at positions 3 and 2 are displayed in Figure 2(d).

The proportion of defects and stacking faults in the system is also proportional to the corresponding number of speckles or peak maximum intensity of the measured 202 reflection, correspondingly.

4.4 RESONANCE

4.4.1 Resonant X-ray Scattering (RXS)

The main feature of the resonant enhancement of x-ray scattering at an absorption edge i.e. of resonant (or resonant anomalous) x-ray scattering (RXS) is its tensorial character, which reflects the anisotropy of the electronic shells involved and distinguishes from general, more widely used x-ray diffraction. Superlattice (or *forbidden*) reflection peaks, extinct by the space group crystal symmetries, appear as originated in a long range ordering of any physical quantity coupled to the electronic density of states [111]. Their origin is due to the fact that x-rays see reflections that should be related by symmetry, but differently oriented atomic scattering factors give rise to non-vanishing structure factor tensors, as consequence of the presence of charge modulations or local structural distortions [112-117]. RXS is widely used for the study of charge or orbitally ordered phases (CO and OO, respectively) [118-125], where no other experimental technique can match the amount of information it provides. The joint analysis of the incoming-scattered light polarization correlation allows us to reconstruct in detail the spatial anisotropic distribution of the electronic density of states. Moreover, the dependence of the scattered intensity on the energy of the incident photons is a mark of the nature of the superlattice reflection, i.e. CO or OO type, if its origin is not magnetic [126]. Thus, RXS has served to precisely quantify the amount of charge segregated between crystallographically inequivalent transition metal ions in doped CO-OO perovskites across metal-insulator transitions, and for instance permitted to discard the classic ionic model based on a distribution of Mn^{3+} and Mn^{4+} ions in manganites. Moreover, some CO configurations can break the centrosymmetric site symmetry and induce ferroelectric phases as a key mechanism to obtain novel charge-driven multiferroics (as in e.g. Ni oxides). Besides the sensitivity to the local distribution of electronic charge, one of the main applications of RXS focuses on Bragg reflections with a magnetic origin. While the dominant interaction between x-rays and matter comes through electronic charge, the fingerprint of magnetization, several orders of magnitude smaller, can also be detected using high brilliance synchrotrons. Magnetic x-ray scattering (MXS) enables the separation of spin and orbital magnetic moment contributions to the total magnetization density in non ferromagnetically long range ordered systems. Resonant MXS or RMXS introduces atomic species and shell selectivity. As in the case of XAS, RXS (understood as comprehending RMXS in the following) can be performed employing soft and hard x-rays. Soft RXS experiments suffer from the same limitations as soft XAS do, those derived from the large scattering cross section in air (the beam propagation at large distances is only possible under ultra-high vacuum conditions), tending to make the experiments technically more troublesome. In addition, large wavelengths characteristic of soft x-rays also play at reducing the reciprocal space attainable and thus, many resonant reflections (originated by either charge or magnetic moments) lie often out of it and cannot be addressed. This forces some RXS studies to be performed necessarily in the hard x-rays domain. Hard RXS presents other advantages: i) the diffractometer is usually placed in open air allowing more spatial flexibility and the inclusion of more circle stages, thus redounding in the enlargement of the reciprocal space attainable; ii) better compatibility with low temperature physics, also derived from the elimination of the ultra-high

vacuum working conditions (which also technically simplifies and speeds up experiments); iii) the larger penetration of x-rays permits to get a more reliable picture of the bulk properties and the effects of sample surface degradation lose importance. On the other hand, neutron diffraction remains to be the reference technique for magnetic structure determinations, although MXS offers some advantages in numerous cases. First, synchrotron radiation provides a higher *Q*-resolution for diffraction studies. Second, the minimum size of the samples that can be studied with x-rays is also far smaller. Third, the neutron diffraction absorption cross section (non monotonously dependent with atomic number or weight) of some rare earths is very large, which makes the precise characterization of the magnetic structures they form only achievable via MXS. Actually, the analysis of the polarization and diffracted intensity as a function of the incident light polarization can yield the moments orientation with great precision. Last but not least, in systems with more than one magnetic species, RMXS can discriminate the individual contributions.

The scientific applications of resonant x-ray scattering cover a broad distribution of topics. This technique was first reported about twenty years ago. The unique combination of spectroscopy and diffraction sensitivities that is proposed was extensively employed during the first decade of the century to address CO and OO phases in transition metal oxides, becoming an invaluable tool for their characterization [118-125]. During the last five years instead, the boosting of multiferroics research has found reflection on the number and impact of dedicated works performed with RXS. As the capability of tuning the incident light polarization in the range of hard x-rays became widespread by the use of diamond phase retarders [127-129**]**, complex spin arrangements like e.g. cycloids or helices were addressed, mainly on materials with more than one magnetic species ordered [130,131]. The problem of chirality, central to these exotic magnetic orders, has also been the subject of several works, and domains mapping becomes also possible thanks to the reduced dimensions of the x-ray beam spot [132-134]. New advances in sample environment, particularly the possibility to in-situ apply large magnetic and electric fields to the samples, made RXS more versatile and suited it even more to the study of multiferroics [135,136]. In parallel to the growing interest on this last class of compounds, the first experiments on new high T_C superconductors based on Fe were conducted early after their discovery, where Fe long range ordered magnetic phases were characterized, also unveiling its influence via exchange interaction over the distribution of the local density of charge in other elements of the unit cell, such as pnictides. Particularly useful were the studies on systems containing rare earths that order magnetically at low temperatures. The detailed study of these phases and their impact on Fe magnetic order is of key importance to understand the mostly exclusive relation between magnetization and superconductivity [137-139].

4.4.2 Effect of light polarization (and its application in extreme sample conditions)

The nature of multipoles involved, charge and orbital ordering, can be investigated by exploring the variation of scattering matrix elements. This is ultimately done by detecting the intensity diffracted in different polarisation channels as a function of either the reciprocal lattice position or, in a fixed position, of the azimuthal angle (so called azimuth scan: rotation around a vector perpendicular to the surface) [140] (Figure 1).

Recently, a rotation of the linear incident light with respect to the scattering plane has revealed new and interesting phenomena of multipole interference [141], resulting in a new technique (so called polscan), complementary to the azimuth scan. By exploiting the chemical and site selectivity of RXS, polscan has been used to

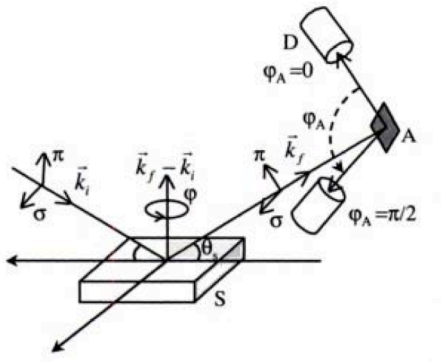

Figure 1. *A schematic experimental arrangement for RXS consisiting of a sample crystal (S), an analyzer crystal (A) and a photon detector (D). The vectors* $\boldsymbol{k_i}$ *and* $\boldsymbol{k_f}$ *are the incident and scattered x-ray momentum,* φ *is the azimuthal angle,* φ_A *is the analyzer angle*

resolve complex magnetic structures, showing enhanced sensitivity to magnetic structure details with respect to neutrons [142].

From the sample point of view, the peculiarity of the technique is that the diffractometer is kept fixed in scattering conditions and just the incoming light is changed during the measurement, avoiding any problem coming from domains and alignments. For this reason, it is particularly suitable when demanding sample environments are needed.

In general, piezoelectric, ferroelectric, magnetoelectric and multiferroic materials represent interesting classes of materials, both from a fundamental point of view and for technological applications. In particular, their sensitivity to externally applied fields plays a central role and calls for an in-situ investigation. For its characteristics, polscan promises to be a very suitable technique to gather information.

Indeed, the very first results by applying a magnetic field on multiferroics [143], on frustrated magnets [144], and of electric field on magnetoelectrics [145] demonstrate the promising versatility and the potential of the technique.

The price to pay is just the installation of a phase retarder to transform the incident light, linearly polarized in the synchrotron plane, to any desired polarisation state, as specified in section 6.2.4.

As mentioned previously, the intensity of weak superlattice reflections can be due to either a structural modulation, contributing to the structure factor as a Thomson term or because the anomalous Atomic Scattering Factor (ASF) of atoms, now in different crystallographic sites, differ in some energy range. Normally, these differences are larger for photon energies close to an absorption edge, showing an enhancement (or strong decrease) of the scattered intensity just around the absorption threshold. In the case of symmetry forbidden reflections, only the resonant term is present. Since RXS involves virtual transitions of core electrons into empty states above the Fermi level, the excited electron is sensitive to any anisotropy around the anomalous atom so that the anomalous ASF has a tensorial character. Thus, a reflection can be observed on resonance if any of the components of the structure factor tensor is different from zero. In the case of weak superlattice reflections, the resonant atoms occupy different crystallographic sites and have different local structures. Thus, the anomalous ASF are different at energies close to the absorption edge and the scattered intensity shows a resonance reflecting the differences of the ASF between these non-equivalent atoms.

Experimentally, the tensor character of the Atomic Scattering Factor (ASF) due to the orbital order can directly be observed through the azimuthal angle (φ) dependent scattering intensity and polarization analysis of the scattering intensity at the orbital and charge superlattice reflections. Because of the tensor character of ASF, the scattered x ray has both the π- and σ-polarized components, which are separated by the analyzer scan. The analyzer crystal must be cut along special plane directions to satisfy the specular reflection condition $2\theta_A=90^\circ$ for the selected absorption edge energy. These components (σ,π) are then separately detected by a detector (analyzer scan) with φ_A = 0 and $\pi/2$, respectively. An enough set of analyzer crystals should be provided to achieve the maximum number of atomic absorption edges for polarization analysis.

4.4.3 Examples

4.4.3.1 Multiferroic systems

The search and investigation of emerging properties in transition metal oxides is currently a very active area in solid-state physics that covers a wide variety of domains, from superconductivity to spin-electronics. Strongly correlated or frustrated oxides derive many of their most interesting physical properties from the interplay between spin, lattice, charge, and orbital degrees of freedom. The delicacy of this interplay makes these materials sensitive to both chemical and physical tuning (external fields). These complex systems offer excellent opportunities for

applications: challenging opportunities are offered associated to a variety of giant responses: magnetoelectric (ME), thermoelectric (TE), magnetoresistive (MR), magnetooptic (MO), etc., i.e., oxides with complex ordering phenomena that may induce magnetoelectric (ME) multiferroicity and novel oxides useful for electronic applications.

Materials that combine coupled electric and magnetic dipole orders are called "magnetoelectric multiferroics" [146-148]. Roughly, multiferroic (MF) compounds can be classified in two groups [147-149]: Type-I, where ferroelectricity appears at temperatures uncorrelated to any magnetic transition, and Type-II, where ferroelectricity and long range order magnetism develop at the same time and consequently are strongly coupled. Typical examples of Type-I MFs are the "mixed systems" with both d_0 and d_n ions like $PbCo_{1/2}W_{1/2}O_3$ or $PbFe_{1/2}Ta_{1/2}O_3$ [148]. Another approach makes use of Bi^{3+} and Pb^{2+} ions with lone-pair electrons in the perovskite A-site like $BiFeO_3$ [148]. In the Type-II group, an exotic (non collinear) magnetic order drives the inversion symmetry break. The orthomanganites showing either a cycloidal magnetic ordering (spin-frustrated) [132,150,151] or an E-type magnetic ordering (exchange striction mechanism) are good examples [131,152]. Figure 1

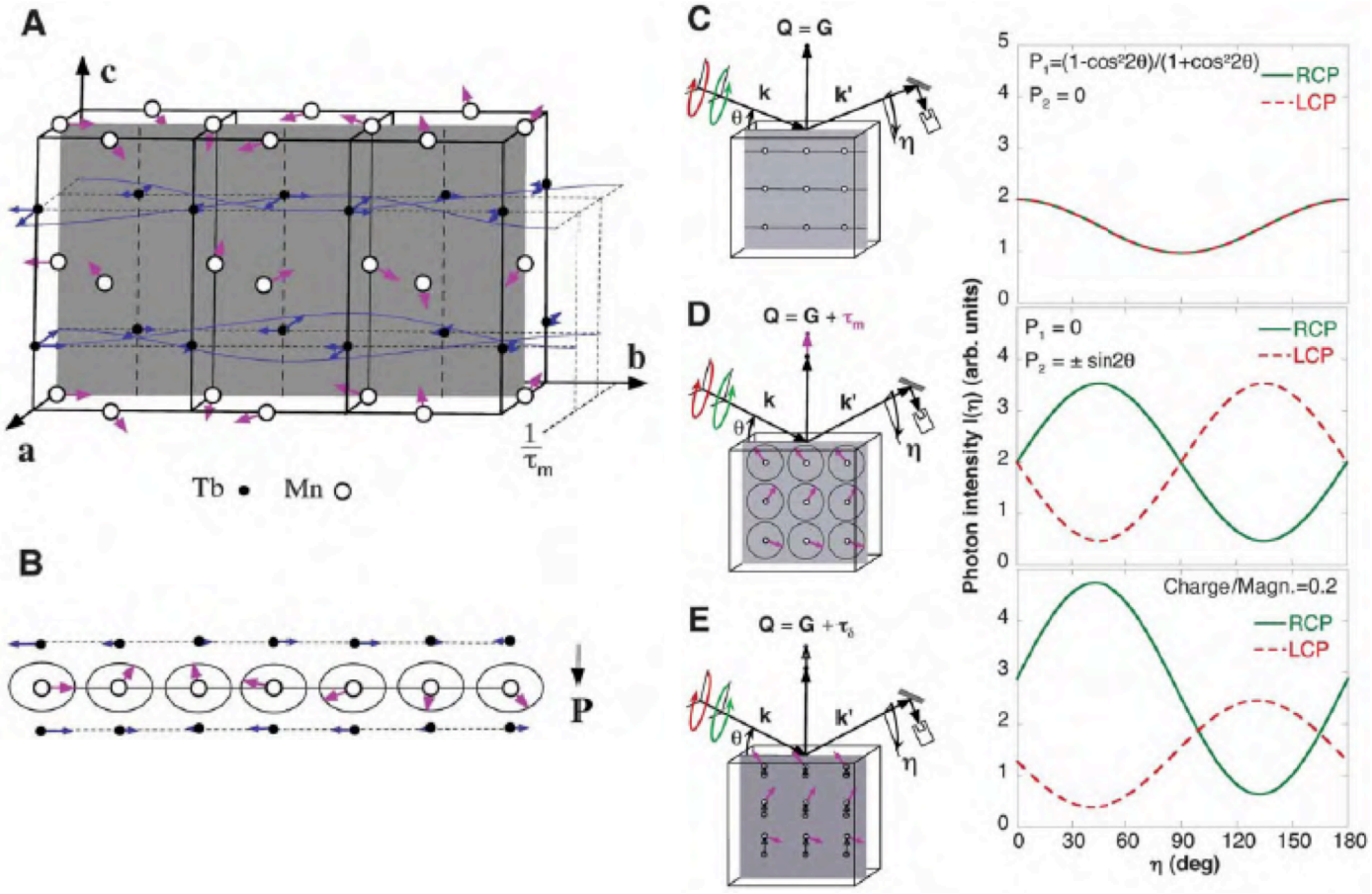

Figure 1. *The x-ray diffraction experiment. (**A**) The crystallographic and magnetic structure of $TbMnO_3$. Arrows in blue and magenta correspond to the spin moments on the Tb and on the Mn, respectively. (**B**) Projection of the magnetic structure onto the bc plane shows how the Mn spin cycloid relates to the spontaneous ferroelectric polarization **P**. (**C** to **E**) Incident circularly polarized x-rays diffract from a sample, and the polarization state of the scattered beam is determined with a linear polarization analyzer. **k** and **k′** are the wave vectors of the incident and scattered beams, respectively. The intensity I(η) as a function of the rotation angle h around k′ is given by $I(\eta) \propto 1 + P_1 \cos(2\eta) + P_2 \sin(2\eta)$, where the Stokes parameter P_1 describes the linear polarization parallel and perpendicular to the plane of scattering, and P_2 describes the oblique linear polarization. (**C**) Charge diffraction occurs when the wave vector transfer $\mathbf{Q} = \mathbf{k}' - \mathrm{k}$ is equal to a reciprocal lattice vector **G** (Laue condition). (**D**) Nonresonant magnetic scattering (NRMS) from an incommensurate cycloid of propagation wave vector tm, depicted with magenta arrows. (**E**) Interference between NRMS and charge scattering (20% that of NRMS) due to atomic displacements, shown with black arrows ($\tau_\delta = \tau_m$).*

shows an example of MF compound becoming to Type-II: $TbMnO_3$ [131,153]. In this example the nature of the ferroelectricity has remained rather elusive. Exploiting the magneto-electric coupling, the use of an electric field to produce a single magnetic domain state, and a magnetic field to induce ionic displacements allows getting from the experimental intensities the interference between charge and magnetic x-ray scattering that encode the amplitude and phase of the displacements. When combined with a theoretical analysis, the data allow resolving the ionic displacements at the femtoscale, and showing that such displacements make a substantial contribution to the zero-field ferroelectric moment.

The family of wolframites $Mn_{1-x}Co_xWO_4$ has also revealed a rich magnetic phase diagram with several, sometimes coexisting multiferroic phases [154-156]. Using RXS the individual orientation of Mn and Co magnetic moments was refined in one of them, which showed to be intriguing [157]. In these compounds as well as in Type I MFs RXS offers the possibility to characterize (often tiny) structural distortions originated in the magnetoelastic coupling, which is of great importance for our understanding of the MF behaviour. In so-called charge ordering oxides, mixed valence ions with geometrical or magnetic frustration may form a polar arrangement causing improper ferroelectricity without ionic displacement. As the ions are also magnetic, the magnetic ordering may appear coupled to ferroelectricity. This mechanism was proposed for $LuFe_2O_4$ and related ferrites [158]. These compounds belong to Type-I as ferroelectricity is developed at the CO transition above the magnetic transition. There is a general agreement in that stoichiometric RFe_2O_4 (R=Ho to Lu, and Y) crystallizes in a rhombohedral unit cell (R-3m) showing a layered arrangement of Lu-O layers separated by a double layer of Fe-O. CO occurs at ~330 K yielding a monoclinic structure. Magnetic order appears at ~240 K and 2D ferrimagnetic order was suggested by neutron scattering studies [159]. Ferroelectricity in $LuFe_2O_4$ was understood as the combination of two factors, the bilayer formation of triangular lattices of Fe atoms and frustrated charge ordering in each layer giving rise to charged planes with opposite signs in consecutive layers [158,160]. However, recent single-crystal neutron and x-ray diffraction studies [161,162] reveal a 3D magnetic ordering and a new CO scheme yielding a nonpolar structure at low temperature, which it is at odd with a bulk ferroelectric behaviour. Extrinsic effects are proposed to account for the ferroelectric features. These materials form part of the interesting $4f\text{-}5d^0$ materials group that has exploded recently with discoveries of novel states of matter, including topological insulators [163] and quantum spin Hall materials [158]. By the other side, the uniqueness of the 5d systems lies in the interplay of the equally strong spin-orbit interaction and the electronic correlations [164]. It leads to unconventional electronic states that cannot be described using the language of weakly interacting spin and orbital states. Resonant x-ray scattering (RXS) is a powerful tool to probe these states. In Sr_2IrO_4, for example, RXS was used to reveal the complex Jeff = 1/2 state of the Ir ion [165], and thus a novel spin-orbital Mott state was discovered. This state has been proposed to give rise to a novel topological state of matter and to a quantum Hall effect in hexagonal lattices [162], and is also relevant for quantum computing [166]. A large number of other intriguing 5d compounds are awaiting investigation. Ir systems, in particular, exhibit anomalous magnetic states ($Sr_3Ir_2O_7$) [167], spin-Hall effect (Na_2IrO_3) [164], and unconventional dimerized orbital states ($CuIr_2S_4$) [168,169]. RXS combined with polarization control/analysis can provide definitive insight into the nature of the electronic states of these materials. Large spin-orbit coupling, which is the defining characteristic of the 5d materials, is important for many other fundamental and applied topics. Multiferroic materials [170], for example, require large values of this coupling for enhanced magnetoelectric effects, and a search of 5d-based systems (based on Ir-doped Ca_3MnCoO_6, for instance).

4.4.3.2 Fe-based novel high T_C superconductors

The unexpected recent discovery of new Fe-based compounds that exhibit a superconductive behaviour at relatively high temperatures has open up new research avenues to probe the origin of zero-resistance electrical conductivity and has fostered hopes that this may ultimately lead to a complete theoretical understanding for all classes of high-T_C superconductors (SCs) [171,172]. Until very recently, high temperature superconductivity was mainly associated to cuprate superconductors (SCs). These are oxides in which the layered crystal structure contains "sheets" with Cu and O. Interestingly, oxides are generally not good electrical conductors aside from superconductors. Even more surprising is the fact that Cu ions carry a magnetic spin, which would be enough to destroy conventional superconductivity. Moreover, it turns out that magnetism is not only tolerated in cuprates, but is suspected to play a key role in the Cooper pairing. Two decades of efforts based on thousands of experimental and theoretical research works allowed pointing electron-electron interactions (rather than electron-phonon ones) play the key role to trigger the superconductivity in high T_C SCs [173,174]. But in 2008 the world of superconductivity was shocked by the surprising discovery of a completely new class of high-T_c superconductors based on iron. The pioneer compound was LaFeAsO, belonging to the so-called "1111" family of pnictides, but immediately many others followed, like SmFeAsO [171,175]. The FeAs4 tetrahedron being the basic building rock of FeAs pnictide layers (believed to be crucial for the superconducting properties), this was also found in "122" rare earth- free compounds such as $BaFe_2As_2$ or "111" 's LiFeAs. [176,177]. Overall, a T_C as high as 55 K was found. Even the simplest FeSe ("11") was found to superconduct, although with a very modest T_C [178]. However, this can be noticeably increased by Te doping or by mechanical pressure [179]. But the interest on Fe selenides goes further and has FeSe become a key block of some of the most interesting new Fe-based SCs. Indeed, the intercalation of FeSe layers with alkali-earths results in measured T_C values as high as those in Fe pnictide, and counts on an added interesting characteristic: alkali metal Fe selenides are magnetic insulators, which brings closer the together the fields of Fe- and Cu-based SCs.

The main focus of the research in Fe-based SCs has been to understand the origin of the vanishment of the electrical resistance in these new materials, as well as their engineering for their potential use in devices [180]. But despite the many attempts and the rapid knowledge progress on these new families of compounds, the electron pairing mechanism remains yet unclear. Interestingly, different Fe-based superconducting families show significant variations in their physical properties, such as magnetically ordered moments, effective masses, superconducting gaps and critical temperatures, and the superconducting state can be manipulated by chemical substitution [179,181,182] or hydrostatic pressure [183-185], underlying the key role of the delicate interplay between electronic and structural properties.

RXS studies have notably contributed to the characterization and understanding of an extensive series of Fe-based SCs during the last years. So, experiments on crystals belonging to the $BaFe_{1-x}TM_xAs2$ (*TM*: Ru, Ir) series demonstrated that Ru and Ir heavy transition metal substitutes at the Fe site get magnetically polarized by Fe forming long range ordered structures below T_N despite their tendency to suppress the spin density wave ordered phase. In other words, magnetism gets to locally survive around the dopant ions [186,187]. Moreover, the Ir-doped compounds showed coexistence zones of magnetic order and superconductivity. On the other hand, in the Ru doped crystal typical signatures of a possible orbital order (with onset at T_N) were found, although deeper investigations are pending to confirm this point. If doping the same Fe-122 system with a lighter magnetic *TM* such as Co, the commensurability of the Fe magnetic order, at the centre of the debate on the SC behaviour, is put into question [188]. Indeed, the observation of coexistence and competition between superconductivity SC and AFM order in some members of the iron-arsenide family of superconductors has raised interesting issues regarding the nature of both the SC and AFM states. Several theoretical treatments have demonstrated that coexistence is inconsistent with conventional BCS coupling, whereas the $s\pm$ state, arising from pairing through magnetic fluctuations,

is compatible with coexistence and competition between SC and AFM order [189,190]. However, the nature of the AFM state in the doped superconducting compounds, particularly the potential for incommensurability of the magnetic structure, remains a significant issue under debate in both theoretical and experimental work. It has been argued that an incommensurate magnetic structure is expected for the doped iron arsenides because of imperfect nesting of the hole and electron Fermi surface pockets, referencing previous work on chromium. Some theoretical models find that the coexistence between AFM and SC points to incommensurate AFM order. But it has also been noted that while incommensurability may broaden the coexistence regime, it does not appear to be a prerequisite for coexistence [191,192].

The analysis of spin-lattice interactions is another well-known stronghold of hard x-rays RXS. This would permit to verify the proposal of Balatsky et al. [193] who based on symmetry considerations have suggested that the Fe SDW order may induce a CDW in Fe-122 (e.g.$BaFe_2As_2$) and Fe-11 (e.g. FeTe) compounds. The latter remain nearly as unexplored by RXS as the recently discovered FeSe.

The stability of the Fe SDW phase against internal fields such us those produced by the magnetic ordering of rare earths at low temperatures in pnictides (e.g. $EuFe_2As_2$ [138] or SmFeAsO [194**]**) has been also studied by RXS. While in most of the cases the characteristics of Fe AFM order tuned by the rare earth ordering at very low Ts, $EuFeAs_2$ is one of the few known examples where this interaction has been shown to be minimal. However, the polarization effect of the rare-earth on As electronic bands near the Fermi level, which remains barely explored in Fe-122 compounds, yielded positive results in $EuFe_2As_2$ compound, with a possible interpretation in terms of an orbital order, as suggested for Ru in $BaFe_{1-x}Ru_xAs_2$ [184]. The substitution of Fe by Rh in the Eu-based compound ($EuRh_2As_2$ [137]) produces the appearance of an incommensurate AFM structure coupled to the CM one. The analysis of resonant magnetic reflections indicates a large sensitivity of the magnetic structure on the Eu valence. Last, the study of the effects of the Ce magnetic moments order in CeFeAsO has also shown the (generalized) vulnerability of the Fe SDW order by small perturbations, as it happens with small chemical doping or external applied pressure. [139].

4.5 REFERENCES

[1] P. Eisenberg, W.C. Marra, Phys. Rev. Lett. **46**,(1981), 1081
[2] R. van Rijn et al., Rev. Sci. Instrum. **79**, 085103 (2008)
[3] S. Ferrer, X. Torrelles, E. V. der Vegt, P. Fajardoand V. Etgens, Phys. Rev. Lett, **75**, (1995), 1771-1774
[4] S. Ferrer, P. Fajardo, F. de Bergevin, J. Alvarez, X. Torrelles, H. A. van der Vegt and R. van Silfhout, Phys. Rev. Lett., **77**, (1996), 747-750
[5] H. A. van der Vegt, J. Alvarez, X. Torrelles, S. Ferrer and E. Vlieg, Phys. Rev. B **52**, (1995), 17443-17448
[6] X. Torrelles, J. Rius, M. Pedio, R. Fellichi, P. Rudolf, J. Alvarez, S. Ferrer, C. Miravilles, Phys. Stat. Sol. B **215** (1999) 773
[7] A. Maskaraque, J. Avila, J. Alvarez, M.C. Asensio, S. Ferrer, EG. Michel, Phys. Rev. Letter **82** (1999) 2524
[8] I. K. Robinson et al., Phys. Rev. Lett. **88**, 096104 (2002)
[9] P. Carro, *Phys.Chem.Chem.Phys.* **16** (2014) 19017 and references therein.
[10] P. Carro et al., *J. Phys. Chem.* C **117** (2013) 2160
[11] J. Ga et al., *J. Phys. Chem.* C **117** (2013) 24985–24990.
[12] M. G. Roper, M. P. Skegg, C. J. Fisher, J. J. Lee, V. R. Dhanak, D. P. Woodruff and R. G. Jones, Chem. Phys. Lett., **389** (2004) 87–91.
[13] C. Ponchut et al., J. Inst. **6** (2011) C01069.
[14] M.J. Capitan, J. Alvarez, J.J. Calvente, R. Andreu, Angewandte Chem. Int Ed. **45** (2006) 6166

[15 and related] J. Weckesser, A. de Vita, JV. Barth, C. Cai, K. Kern, Phys. Rev. Lett. **87**(9) (2001) 96101; P. Qian, H. Nanjo, T. Yokoyama, T.M. Suzuki, K. Akasaka, H. Orhui, Chem Comm (2000) 2021; M. Pérez Méndez, J. Fayos and C.R. Mateo, Advances in Biochirality Chapter 24 (1999) Elservier; M. Pérez Méndez, R. Marsal, L. Garrido, M. Martín, Macromolecules **36** (2003) 8049
[16 and related] S. Mayer and J. Kessler, Phys. Rev. Lett. **74**, 4803 (1995); K. Blum and D.G. Thompson, Adv. At. Mol. Opt. Phys. **38**, 39 (1997); I.M. Smith, D.G. Thomson and K. Blum, J. Phys. B: At. Mol. Opt. Phys. **31**, 4029 (1998); K. Ray, S.P. Ananthavel, D.H. Waldeck, and R. Naaman, Science **283**, 814 (1999); M. Mussigman, A. Busalla, K. Blum, and D.G. Thompson, J. Phys. B: At. Mol. Opt. Phys. **34**, L79 (2001); L.A. Feigin and D.I. Svergun, Structural analysis by small angle Xray and neutron scattering, Plenum Press (New York, 1987), pp. 335; L.D. Barron, J. Am. Chem. Soc. **108**, 5539 (1986); G.L.J.A. Rikken and E. Raupach, Nature **405**, 932 (2000)
[17 and related] M.J. Capitán, R. Otero, J. Álvarez, R. Miranda, ChemPhysChem **12** (2011) 1267; M.J. Capitán, J. Álvarez, Y. Wang, R. Otero, M. Alcamí, f. Martín, R. Miranda, ChemPhysChem **14** (2013) 3294
[18] I. Kuzmenko et al., Chirality **10** (1998) 415
[19] E.Y. Tsymbal and H. Kohlstedt, Science **313**, 181 (2006).
[20] C.-G. Duan, S. S. Jaswal, and E.Y. Tsymbal, Phys. Rev. Lett. **97**, 047201 (2006).
[21] M. Fechner, S. Ostanin, and I. Mertig, Phys. Rev. B **77**, 094112 (2008).
[22] S. Valencia et al., Nature Matter. **10**, 753 (2011).
[23] S. Thiel, G. Hammerl, A. Schmehl, C.W. Schneider, and J. Mannhart, Science **313**, 1942 (2006).
[24] M. Salluzzo, S. Cariglio, X. Torrelles et al., Adv. Matter. **25**, 2333 (2013)
[25] H.L. Meyerheim et al., Phys. Rev. Lett. **108**, 215502 (2012)
[26 and related] S. Blomberg, M.J. Hoffmann, J. Gustafson, N. M. Martin, V. R. Fernandes, A. Borg, Z. Liu, R. Chang, S. Matera, K. Reuter, and E. Lundgren, 'In situ X-ray Photoelectron Spectroscopy of model catalysts: At the edge of the gap ' Phys. Rev. Lett. **110** 117601 (2013); A. Hellman, A. Resta, N. M. Martin, J. Gustafson, A. Trinchero, P.-A. Carlsson, O. Balmes, R. Felici, J. N. Andersen, E. Lundgren, and H. Grönbeck, 'The active phase of Pd during methane oxidation' J. Phys. Chem. Lett. **3** 678 (2012); J. Gustafson, R. Westerström, A. Mikkelsen, A. Resta, J. N. Andersen, X. Torrelles, O. Balmes, M. Schmid, P. Varga, B. Hammer, G. Kresse, C. J. Baddeley, and E. Lundgren. 'Structure and catalytic reactivity of Rh oxides' Catalysis Today **145**, (2009), 227; S. Ferrer, M. D. Ackermann, and E. Lundgren, 'In Situ Investigations of Chemical Reactions on Surfaces by X-Ray Diffraction at Atmospheric Pressures' MRS Bulletin **32** 1010 (2007)
[27] H.S. Taylor, Proc. Roy. Soc. Lond. A **108** (1925) 105.
[28] Yates, J. T. Surface Chemistry at Metallic Defect Sites. J. Vac. Sci. Technol. A **13**, 1359–1367 (1995).
[29] Hammer, B., Nielsen, O. H. & Nørskov, J. K. Structure sensitivity in adsorption: CO interaction with stepped and reconstructed Pt surfaces. Catal. Lett. **46**, 31–35 (1997).
[30] Somorjai, G. A. Introduction to Surface Chemistry and Catalysis (Wiley, 1994).
[31] Zambelli, T.,Wintterlin, J., Trost, J. & Ertl, G. Identification of the 'active sites' of a surface-catalyzed reaction. Science **273**, 1688–1690 (1996).
[32] Dahl, S. et al. Role of steps in N2 activation on Ru(0001). Phys. Rev. Lett. **83**, 1814–1817 (1999).
[33] Geerlings, J. J. C. et al. Fischer–Tropsch technology—from active site to commercial process. Appl. Catal. A **186**, 27–40 (1999).
[34] Vang, R. T. et al. Controlling the catalytic bond-breaking selectivity of Ni surfaces by step blocking. Nature Mater. **4**, 160–162 (2005).
[35] D.W. Blakely, G.A. Somorjai, J. Catal. **42** (1976) 181.
[36] J. Xu, J.T. Yates Jr., J. Chem. Phys. **99** (1993) 725.
[37] T. Zambelli, J. Wintterlin, J. Trost, G. Ertl, Science **273** (1996) 1688.
[38] S. Dahl, A. Logadottir, R.C. Egeberg, J.H. Larsen, I. Chorkendorff, E. Törnqvist, J.K. Nørskov, Phys. Rev. Lett. **83** (1999) 1814.

[39] T. Zubkov, G.A. Morgan Jr., J.T. Yates Jr., O. Kuhlert, M. Lisowski, R. Schillinger, D. Fick, H.J. Jansch, Surf. Sci. **526** (2003) 57.
[40] R.T. Vang, K. Honkala, S. Dahl, E. Vestengaard, J. Schnadt, E. Laegsgaard, B.S. Clausen, J.K. Norskov, F. Besenbacher, Nat. Mater. **4** (2005) 160.
[41] S.M. Davies, G.A. Somorjai, Surf. Sci. **91** (1980) 73.
[42] J.L. Gland, M.R. McClellan, F. Read McFeely, J. Chem. Phys. **79** (1983) 6349.
[43] L.P. Ford, H.L. Nigg, P. Blowers, R.I. Masel1, J. Catal. **179** (1998) 163.
[44] A. Szabó, M.A. Henderson, J.T. Yates, J. Chem. Phys. **96** (1992) 6191.
[45] B. Atalik, D. Uner, J. Catal. **241** (2006) 268.
[46] J. Silvestre-Albero, G. Rupprechter, H. Freund, J. Catal. **266** (2009) 359.
[47] D.W. Goodman, J. Catal. **216** (2003) 213.
[48] N. Lopez, T.V.W. Janssens, B.S. Clausenb, Y. Xu, M. Mavrikakis, T. Bligaard, J.K. Nørskov, J. Catal. **223** (2004) 232.
[49] B.L.M. Hendriksen, M.D. Ackermann, R. van Rijn, D. Stoltz, I. Popa, O. Balmes, A. Resta, D. Wermeille, R. Felici, S. Ferrer, J.W.M. Frenken, Nat. Chem. **2** (2010) 730.
[50] O. Balmes, G. Prevot, X. Torrelles, E. Lundgren, S. Ferrer, Journal of Catalysis **309** (2014) 33.
[51] M. A. Newton, C. Belver-Coldeira, A. Martinez-Arias, M. Fernandez-Garcia, Angew. Chem. Int. Ed. **46**, 8629 (2007).
[52] M. Bäumer et al., Phys. Chem. Chem. Phys. **9**, 3541 (2007).
[53] Nolte et al., Science **321**, 1654 (2008)
[54] W.G. Onderwaater, R. van Rijn, D Wermeille, A. Resta, O.Balmes, R.Felici, J.W.M.Frenken, (to be published).
[55] Hadbook of Electrochemistry, Edited by Cynthia G. Zoski, Elsevier, The Netherlands, First edition (2007) pag.47
[56] *Frontiers in Surface and Interface Science*, edited by C. B. Duke and E.W. Plummer (Elsevier, Amsterdam, 2002).
[57] J. A. Rodriguez and J. Hrbek, Acc. Chem. Res. **32**, 719 (1999).
[58] *Self-Assembled Monolayers of Thiols*, edited by A. Ulman, Thin Films Vol. 24 (Academic, San Diego, 1998).
[59] P. Fenter, A. Eberhardt, and P. Eisenberger, Science **266**, 1216 (1994); G. J. Jackson *et al.*, Phys. Rev. Lett. **84**, 119 (2000).
[60] J. Wang, A. J. Davenport, H. S. Isaacs, and B.M. Ocko, Science **255**, 1416 (1992).
[61] C. Vericat et al., Phys. Rev. Lett. **90**, 075506 (2003).
[62] C. Vericat, G. Andreasen, M. E. Vela, and R.C. Salvarezza, J. Phys. Chem. B **104**, 302 (2000).
[63] A. Naudon and D. Thiaudière, J. Appl. Cryst. **30** (1997) 822
[64] P. Andreazza, C. Andreazza, J.P. Rozenbaum, A.L. Thomann, P. Brault,. Surf. Coat. Tech.. **150** (2002) 1
[65] M. Rauscher, T. Salditt, H. Spohn, Phys. Rev. **B 52** (1995)16855
[66] A. Barbier, G. Renaud, J. Jupille. Surface Science **456** (2000) 979 and ESRF Highlights 1999.
[67] T.H. Metzger, I. Kegel, R. Panlago and J.P Pelsi, J. Phys. **D 32** (1999) 202
[68] M.-C. Saint-Lager, A. Bailly, P. Dolle, R. Baudoing-Savois, P. Taunier, S. Garaud_ee, S. Cuccaro, S. Douillet, O. Geaymond, G. Perroux, O. Tissot, J.-S. Micha, O. Ulrich and F. Rieutord, Rev. Sci. Instrum. **78** (2007) 083902.
[69] M.-C. Saint-Lager, A. Bailly, M. Mantilla, S. Garaud_ee, R. Lazzari, P. Dolle, O. Robach, J. Jupille, I. Laoufi and P. Taunier, Gold Bull. **41** (2008) 159.
[70] M.-C. Saint-Lager, I. Laoufi, A. Bailly, Faraday Discuss. 162 (2013) 179.
[71] I. Laoufi, M.-C. Saint-Lager, R. Lazzari, J. Jupille, O. Robach, S. Garaud_ee, G. Cabailh, P. Dolle, H. Cruguel and A. Bailly, J. Phys. Chem. C **115** (2011) 4673.
[72] M.-C. Saint-Lager, I. Laoufi, A. Bailly, O. Robach, S. Garaud_ee and P. Dolle, Faraday Discuss., **152** (2011) 253.
[73] J.-M. Pan, B. L. Maschhoff, U. Diebold and T. E. Madey, J. Vac. Sci. Technol. A **10** (1992)

2470.
[74] F. Cosandey, L. Zhang and T. E. Madey, Surf. Sci., **474** (2001) 1.
[75] R. Lazzari, G. Renaud, J. Jupille and F. Leroy, Phys. Rev. B, **76** (2007) 125412.
[76] R. Lazzari, J. Appl. Crystallogr., **35** (2002) 406.
[77] G. Yu , J. Gao, J .C. Hummelen, F. Wudl, A. J. Heeger, Science **270** (1995) 1789
[78] J. J. M. Halls, C. A. Walsh, N. C. Greenham, E. A. Marsegila, R. H. Friend, S. C. Moratti, A. B. Holmes, Nature **376** (1995) 498
[79] R. J. Kline, M. D. McGhee, E. N. Kadnikova, J. Liu, J. M. J. Frechet, M. F. Toney, Macromolecules **38** (2005) 3312
[80] H. Sirringhaus, P. J. Brown, R. H. Friend, M. M. Nielsen, K. Bechgaard, B. M. W. Langeveld-Voss, A. J. H. Spiering, R. A. J. Janssen, E.W. Meijer, P. Herwig, D. M. De Leeuw , Nature **401** (1999) 685
[81] Y. Kim, S. Cook, S. M. Tuladhar, S. A. Choulis, J. Nelson, J. R. Durrant, D. D. C. Bradley, M. Giles, I. McCulloch, S.-S. Ha, M. Ree , Nat. Mater. 5 **(2006)** 197
[82] S. Berson, R. De Bettignies, S. Bailly, S. Guillerez, Adv. Funct. Mater. **217** (2007) 1377
[83] M. Sanyal et al., Adv. Energy Mater. **1** (2011) 363
[84] J.M. Napoles-Duarte, M. Reyes-Reyes, J. L. Ricardo-Chavez, R. Garibay-Alonso, R. Lopez-Sandoval, Phys. Rev. B **78** (2008) 035425
[85] X. Yang, J. K. J. van Duren, M. T. Rispens, J. C. Hummelen, R. A. J. Janssen, M. A. J. Michels, J. Loos, Adv. Mater. **16** (2004) 802
[86] Robinson IK, Vartanyants IA, Williams GJ, Pfeifer MA, Pitney JA, Phys. Rev. Lett. **87**(19) (2001) 195505
[87] Pitney JA, Robinson IK, Vartaniants IA, Appleton R, Flynn CP, Phys. Rev. B **62**(19) (2000) 13084
[88] Goodman, J. W. Speckle Phenomena in Optics 1st edn (Roberts and Company Publishers, Greenwood Village, 2006)
[89] Sutton, M. et al. Observation of speckle by diffraction with coherent X-rays. Nature **352**, 608–610 (1991)
[90] Mochrie, S. G. et al. Phys. Rev. Lett. **78**, 1275–1278 (1997).
[91] Miao, J., Charalambous, P., Kirz, J. & Sayre, D., Nature **400**, 342–344 (1999).
[92] Marchesini, S. et al. Opt. Express **11**, 2344–2353 (2003)
[93] B. Abbey et al., Nat. Physics **4** (2008) 394
[94] B. Abbey et al., Appl. Phys. Lett. **93** (2008) 214101
[95] M.S. Rodrigues et al., HAL-0028263, Hal.archives-ouvertes.fr/hal-00282863.
[96] T. Scheler et al., Appl. Phys. Lett. **94**, 023109 (2009)]
[97] M.S. Rodrigues, et al., J. Appli. Physics **106**, 103525 (2009)]
[98] M. Barchuck et al., Phys. Rev. B **84**, (2011) 094113].
[99] I. K. Robinson et al., Phys. Rev. Lett., vol. **87**, p. 195505, 2001.
[100] M. C. Newton et al., Nat. Mater., vol. **9**, pp. 279–279, 2010
[101] J. P. Hirth and J. Lothe, Theory of Dislocations (McGraw-Hill, New York, 1968).
[102] F. Bonell, S. Andrieu, C. Tiusan, F. Montaigne, E. Snoeck, B. Belhadji, L. Calmels, F. Bertran, P. Le Fèvre, and A. Taleb-Ibrahimi, Phys. Rev. B **82**, 092405 (2010).
[103] B. M. Moskowitz, J. Geophys. Res. **98**, 18 011 (1993).
[104] J. Kundu, C. Sarkar, and P. Mallick, Semi. Phys. Quant. Electron. Optoelectron. **10**, 1 (2007).
[105] L. M. Giovane, H.-C. Luan, A. M. Agarwal, and L. C. Kimerling, Appl. Phys. Lett. **78**, 541 (2001).
[106] L. Thilly, R. Ghisleni, C. Swistak, and J. Michler, Philos. Mag. **92**, 3315 (2012).
[107] V. L. R. Jacques, D. Carbone, R. Ghisleni, and L. Thilly, Phys. Rev. Lett. **111**, 065503 (2013).
[108] A. Diaz, C. Mocuta, J. Stangl, M. Keplinger, T.Weitkamp, F. Pfeiffer, C. David, T. H. Metzger, and G. Bauer, J. Synchrotron Radiat. **17**, 299 (2010).
[109] V. L. R. Jacques, D. Le Bolloc'h, E. Pinsolle, F.-E. Picca, and S. Ravy, Phys. Rev. B **86**,

144117 (2012).
[110] F. Mastropietro, D. Carbone, A. Diaz, J. Eymery, A. Sentenac, T. H. Metzger, V. Chamard, and V. Favre-Nicolin, Opt. Express **19**, 19 223 (2011).
[111] G. Materlik, C. J. Sparks, K. Fischer, *Resonant Anomalous X-ray Scattering,* Ed. North Holland (1994)
[112] V. E. Dmitrienko, K. Ishida, A Kirfel and E. N. Ovchinnikova, Acta Cryst. A 61, 481 (2005)
[113] J. García and G. Subías, J. Phys.: Condens. Matter **16**, R145 (2004)
[114] G. Subías, J. García, M. G. Proietti, J. Blasco, H. Renevier, J. L. Hodeau and M.C. Sánchez, Phys. Rev. B **70**, 155105 (2004)
[115] Dmitrienko et al., Acta Crystallographica A57, 642 (2001)
[116] G. Subías, J. García, J. Blasco, M. G. Proietti, H. Renevier and M.C. Sánchez, Phys. Rev. Lett. **93**(15), 156408 1-4 (2004)
[117] J. García, G. Subías, J. Herrero-Martín, J. Blasco, V. Cuartero, M. C. Sánchez, C. Mazzoli and F. Yakhou, Phys. Rev. Lett. **102**, 176405 1-4 (2009)
[118] S. Grenier, J. P. Hill, D. Gibbs, K. J. Thomas, M. V. Zimmerman, C. S. Nelson, V. Kiryukhin, Y. Tokura, Y. Tomioka, D. Casa, T. Gog, and C. Venkataraman, Phys. Rev. B **70**, 134419 (2004)
[119] G. Subías, M. C. Sánchez, J. García, J. Blasco, J. Herrero-Martín, C. Mazzoli, P. Beran, M. Nevriva and J. L. García-Muñoz. J. Phys.: Condens. Matter **20**, 235211 (2008)
[120] J. Blasco, J. García, G. Subías, H. Renevier, M. Stingaciu, K. Conder and J. Herrero-Martín, Phys. Rev. B **78**, 054123 (2008)
[121] J. Herrero-Martín, G. Subías, J. García, J. Blasco and M. C. Sánchez, Phys. Rev. B **79,** 045121 (2009)
[122] S. Grenier, A. Toader, J. E. Lorenzo, Y. Joly, B. Grenier, S. Ravy, L.P. Regnault, J. Y. Henry, J. Jegoudez and A. Revcolevsky, Phys. Rev. B 65, 180101 (2002)
[123] J. Herrero-Martin, J. García, G. Subías, J. Blasco and M. C. Sánchez, Phys. Rev. B **70**, 024408 (2004)
[124] G. Subías, J. Herrero-Martín, J. García, J. Blasco, C. Mazzoli, K. Hatada, S. Di Matteo and C. R. Natoli, Phys. Rev. B **75**, 235101 1-8 (2007)
[125] J. Garcia, J. Herrero-Martin, G.Subias, J. Blasco, J.S. Andreu, M. C, Sanchez, , Phys. Rev. Lett. **109**, 107202 (2012)
[126] T. A. W. Beale et al, Eur. Phys. J. Special Topics **208**, 89 (2012)
[127] J. A. Golovchenko, B. M. Kincaid, R. A. Levesque, A. E. Meixner, D. R. Kaplan, Phys. Rev. Lett. **57**, 202 (1986)
[128] K. Okitsu, Y. Ueji, K. Sato, Y. Amemiya, J. Synchr. Rad. **8**, 33 (2001)
[129] V. Scagnoli, C. Mazzoli, C. Detlefs, P. Bernard, A. Fondacaro, L. Paolasini, F. Fabrizi, F. De Bergevin, **16**, 778 (2009)
[130] G. Beutier, A. Bombardi, C. Vecchini, P. G. Radaelli, S. Park, S-W. Cheong, L. C. Chapon, Phys. Rev. B **77**, 172408 (2008)
[131] H. C. Walker, F. Fabrizi, L. Paolasini, F. De Bergevin, J. Herrero-Martín, A. T. Boothroyd, D. Prabhakaran, D. F. McMorrow, Science **333**, 1273 (2011)
[132] R. D. Johnson, P. Barone, A. Bombardi, R. J. Bean, S. Picozzi, P. G. Radaelli, Y. S. Oh, S-W. Cheong, L. C. Chapon, Phys. Rev. Lett. **110**, 217206 (2013)
[133] A. Rodríguez-Fernández, J. A. Blanco, S. W. Lovesey, V. Scagnoli, U. Staub, H. C. Walker, D. K. Shukla, J. Strempfer, Phys. Rev. B **88**, 094437 (2013)
[134] A. Rodríguez-Fernández, S. W. Lovesey, S. P. Collins, G. Nisbet, J. A. Blanco, J. Phys. Soc. Japan **83**, 013706 (2014)
[135] L. Paolasini, C. Detlefs, C. Mazzoli, S. Wilkins, P. P. Deen, A. Bombardi, N. Kernavanois, F. De Bergevin, F. Yakhou, J. P. Valade, I. Breslavetz, A. Fondacaro, G. Pepellin, P. Bernard, J. Synchr. Rad. **14**, 301 (2007)
[136] C. Mazzoli, S. B. Wilkins, S. Di Matteo, B. Detlefs, C. Detlefs, V. Scagnoli, L. Paolasini, P. Ghigna, Phys. Rev. B **76**, 195118 (2007)

[137] S. Nandi, A. Kreyssig, Y. Lee, Y. Singh, J. W. Kim, D. C. Johnston, B. N. Harmon, A. I. Goldman, Phys. Rev. B **79**, 100407(R) (2009)
[138] J. Herrero-Martín, V. Scagnoli, C. Mazzoli, Y. Su, R. Mittal, Y. Xiao, Th. Brueckel, N. Kumar, S. K. Dhar, A. Thamizhavel, L. Paolasini, Phys. Rev. B **80**, 134411 (2009)
[139] Q. Zhang, W. Tian, H. Li, J-W Kim, J. Yan, R. W. McCallum, T. A. Lograsso, J. L. Zaretsky, S. L. Budko, R. J. McQueeney, D. Vaknin, Phys. Rev. B **88**, 174517 (2013)
[140] L. Paolasini, Collection SFN **13**, 03002 (2014) DOI: 10.1051/sfn/20141303002
[141] C. Mazzoli et al., Phys. Rev. B **76** (2007) 195118
[142] R. D. Johnson et al., Phys. Rev. B **78** (2008) 104407
[143] T.A.W. Beale et al., Phys. Rev. Lett. **105** (2010) 087203
[144] C. Mazzoli et al., Phys. Rev. B **77** (2008) 094433
[145] Fabrizi F. et al., Phys Rev. Lett. **102** (2009) 237205
[146] A. Posadas *et al.*, Appl. Phys. Lett. **87**, 171915 (2005).
[147] G. T. Kimura et al., Nature **426**, 55 (2003).
[148] D. I. Khomskii, J. Magn. Magn. Mater. **306**, 1 (2006).
[149] S.-W.Cheong & M. Mostovoy, Nature Mater. **6**, 13 (2007).
[150] M. Kenzelmann, A.B. Harris, et al., Phys. Rev. Lett. **95**, 087206 (2005)
[151] F. Fabrizi, H. C. Walker, L. Paolasini, F. De Bergevin, A. T. Boothroyd, D. Prabhakaran, D. F. McMorrow, Phys. Rev. Lett. **102**, 237205 (2009)
[152] M. Mochizuki, N. Furukawa, and N. Nagaosa: Phys. Rev. Lett. **105**, 037205 (2010).
[153] V. Cuartero, J. Garcia, G. Subías, J. Herrero-Martin, J. Blasco, C. R. Natoli., Journal of Physics Conference Series, **430**, 012101 (2013)
[154] K. Taniguchi, N. Abe, T. Takenobu, Y. Iwasa, T. Arima, Phys. Rev. Lett. **97**, 097203 (2006)
[155] Y-S. Song, J-H. Chung, J. M. S. Park, Y-N. Choi, Phys. Rev. B **79**, 224415 (2009)
[156] I. Urcelay-Olabarría, PhD Thesis, Universitat Autònoma de Barcelona (2012)
[157] J. Herrero-Martín *et al*, in preparation.
[158] N. Ikeda *et al* Nature **436**, 1136 (2005) ; A. M. Malders et al. Phys.Rev. Lett. **103**, 077602 (2009)
[159] J. Iida et al. J. Phys. Soc. Jap. **62**, 1723 (1993).
[160]] J. van den Brink and D. I. Khomskii, J. Phys. : Condens. Matter **20**,434217 (2008).
[161] J. de Groot et al, Phys. Rev. Lett. **108**, 181802 (2012).
[162] S. Lafuerza, G. Subias, J. Garcia, J. Blasco, G. Nisbet, K. Conder, E. Pomjakushina, Phys. Rev. B **90**, 085130 (2014)
[163] For a review, see M.Z. Hasan and C.L. Kane, arxiv:1002.3895.
[164] A. Shitade, H. Katsura, J. Kunes, X.-L. Qi, S.-C. Zhang and N. Nagaosa, Phys. Rev. Lett. **102**, 256403 (2009).
[165] B.J. Kim, H. Ohsumi, T. Komesu, S. Sakai, T. Morita, H. Takagi and T. Arima, Science **323**, 1329 (2009).
[166] G. Jackeli and G. Khaliullin, Phys. Rev. Lett. **102**, 017205 (2009).
[167] I. Nagai, Y. Yoshida, S. Ikeda, H. Matsuhata, H. Kito and M. Kosaka, J. Phys.: Condensed Matter **19**, 136214 (2007).
[168] D.I. Khomskii and T. Mizokawa, Phys. Rev. Lett. **94**, 156402 (2005).
[169] Kohei Fujiwara, Yasuhiro Fukuma, Jobu Matsuno, Hiroshi Idzuchi, Yasuhiro Niimi, YoshiChika Otani & Hidenori Takagi, Nature Communications **4**, 2893 (2013)
[170] S-W. Cheong and M. Mostovoy, Nature Mater. **6**, 13 (2007).
[171] Y. Kamihara, T. Watanabe, M. Hirano, H. Hosono, J. Am. Chem. Soc. **130**, 3296 (2008)
[172] G. R. Stewart, Rev. Mod. Phys. **83**, 1589 (2011)
[173] P. W. Anderson, "Theory of Superconductivity in the High-Tc Cuprates." (Princeton University Press, Princeton, 1997)
[174] V. Kresin, H. Morawitz, S. A. Wolf, "Mechanism of Conventional and High Tc Superconductivity." (Oxford Press, Oxford, 1993)

[175] Z-A. Ren et al., Europhys. Lett. **83**, 17002 (2008)
[176] D. C. Johnston, Adv. Phys. **59**, 803 (2010)
[177] J. Paglione, R. L. Greene, Nat. Phys. **6**, 645 (2010)
[178] F-C- Hsu, J-Y. Luo, K-W. Yeh, T-K. Chen, T-W. Huang, P. M. Wu, Y-C. Lee, Y-L. Huang, Y-Y. Chu, D-C. Yan, M-K. Wu, Proceed. Nat. Acad. Sci. United States of America **105**, 14262 (2008)
[179] M. H. Fang, H. M. Pham, B. Qian, T. J. Liu, E. K. Vehstedt, Y. Liu, L. Spinu, Z. Q. Mao, Phys. Rev. B **78**, 224503 (2008)
[180] Hidenori Hiramatsu et al., J. Phys. Soc. Jpn. **81**, 011011 (2012); Keiichi Tanabe Jpn. J. Appl. Phys. **51**, 010005(2012)
[181] K.-W. Yeh et al., EPL **84**, 37002 (2008).
[182] Y. Mizuguchi et al.,J. Phys. Soc. Jpn. **78**, 074712 (2009)
[183] E. Gati et al., Phys. Rev. B **86**, 220511 (2012)
[184] Shanta R. Saha et al., Cond-Matt.Suppr-Con. arXiv:1309.3576
[185] J. Liu et al., Phys. Rev. B **90**, 094507 (2014)
[186] M. P. M. Dean, M. G. Kim, A. Kreyssig, J. W. Kim, X. Liu, P. J. Ryan, A. Thaler, S. L. Bud'ko, W. Strassheim, P. C. Canfield, J. P. Hill, A. I. Goldman, Phys. Rev. B **85**, 140514(R) (2012)
[187] M. G. Kim, J. Soh, J. Lang, M. P. M. Dean, A. Thaler, S. L. Bud'ko, P. C. Canfield, E. Bourret-Courchesne, A. Kreyssig, A. I. Goldman, R. J. Birgeneau, Phys. Rev. B **88**, 014424 (2013)
[188] M. G. Kim, A. Kreyssig, Y. B. Lee, J. W. Kim, D. K. Pratt, A. Thaler, S. L. Bud'ko, P. C. Canield, B. N. Harmon, R. J. McQueeney, A. I. Goldman, Phys. Rev. B **82**, 180412(R) (2010)
[189] I. I. Mazin, D. J. Singh, M. D. Johannes, M. H. Du, Phys, Rev. Lett. **101**, 057003 (2008)
[190] K. Kuroki, S. Onari, R. Arita, H. Usui, Y. Tanaka, H. Kontani, H. Aoki, Phys. Rev. Lett. **101**, 087004 (2008)
[191] R. M. Fernandes, J. Schmalian, Phys. Rev. B **82**, 014521 (2009)
[192] A. B. Vorontsov, M. G. Vavilov, A. V. Chubukov, Phys. Rev. B **81**, 174538 (2010)
[193] A. V. Balatsky et al., Phys Rev. B **82**, 144522 (2010)
[194] S. Nandi, Y. Su, Y. Xiao, S. Price, X. F. Wang, X. H. Chen, J. Herrero-Martín, C. Mazzoli, H. C. Walker, L. Paolasini et al, Phys. Rev. B **84**, 054419 (2011)

5. INTERNATIONAL STATUS OF THE FIELD

Diffraction beamlines exist at virtually all synchrotrons, underlining the usefulness of the technique. While they share the same basic idea, particular setups, experimental configurations and beamline history make them specific and define which experiments are run on these beamlines, and which are their domains of excellence. In recent years, adapting to the economical and political orientations of society, more and more energy oriented experimental setups have been made available. All these beamlines show projects similar or complementary to SIRENA, however, the flexibility of the beamline together with the different and complementary types of techniques that will be present in the beamline will cover a big spectrum of biology, chemistry and physics areas applied to the study of low dimensional systems. Users will have access to a multifunctional beamline in a performant facility as ALBA offering solutions difficult to get in a beamline as the proposed one in Europe, e.g., integration of the resonance technique in the same beamline.

The Swedish P21 beamline at PETRA III (U. Lienert) is a beamline operating at a high-energy range ideally suited for reaching far out in reciprocal space, while high-resolution measurements such as GISAXS or CXDI will be more suited for lower energies available in ALBA. This beamline should become operational in 2016

NanoMAX at MAX IV will be a beamline dedicated to micro- and nano-samples, and accordingly sized beam. The optics and techniques, which will be implemented there, will be specifically targeted to match the high mechanical precision required for positioning and observing such small samples in a small beam. This however implies that heavy, bulky or complicated sample environments will be cumbersome to fit on these experimental stations.

It is foreseen that it would be advantageous to share knowledge, technical solutions, standards, and equipment across these 3 beamlines which will offer complementary techniques and performances.

DiffMAX at MAX IV. This beamline will have an energy range from 5 to 30 keV and will provide both a tunable monochromatic beam, and also a larger bandwidth beam for very fast measurements. The minimum beam size will be of a few microns, obtained with long focal length, achromatic optics, sufficient space should be provisioned in the experimental hutch to allow adding KB focusing mirrors. This beam will be used in one experimental hutch, with a removable sample station and capability for simultaneous small angle techniques (GISAXS) and wide angle techniques (powder, single crystal, surface diffraction, CXDI).

ESRF, Grenoble: ID03, BM25, BM32, SNBL (R. Felici, G. Castro, G. Renaud, V. Dmitriev)

These beamlines have performed at state of the art level for a long time and will benefit from the upgrade program in place at the ESRF. There is a high demand to access these beamlines, and the needs for diffraction from Spanish users is much greater than the available beamtime at these facilities. Moreover, ESRF closed ID32 beamline (surface diffraction and standing waves beamline) 3 years ago reducing almost 1/3 the time dedicated to the study of low dimensional systems. The effect has been an strong increase of the number of proposals requesting beamtime at the ID03 beamline, reducing the Spanish users accessibility to this facility due, apart of that, to beamtime cuts as consequence of an excess of Spanish proposals (more than 4% of the total ESRF beamtime). For example oversubscription is nowadays a factor 3 for ID03 and higher for BM32 due to its low international beam time available (33%))

ESRF, Grenoble: BM28 (Simon Brown)

The ***XMaS*** beamline has been designed to perform single crystal diffraction over an energy range of 2.5 keV to 15 keV. The beamline is sited on the soft end of dipole 28 (critical energy 9.8 keV).

The beamline mounts a diamond phase plate to convert the incident linear polarised radiation into circular polarisation (Pc) either from X-rays emitted above/below the electron orbit or using a quarter phase-plate. The latter technique is the only way to look at highly anisotropic magnetic materials for which the direction of the sample magnetisation cannot be reversed. The phase-plate assembly is situated upstream of the diffractometer. The diamond phase-plate crystal is mounted on a Huber goniometer and is driven to the quarter-wave plate conditions, for maximum Pc, with a theta and a chi circle. The former rotation stage, which moves the crystal off the Bragg condition, has an accuracy of 10^{-4} degrees (0.36 arcseconds). It is orthogonally mounted on the chi circle. The chi circle sets the optical axis of the diamond at 45° to the incident and plane polarization, with an accuracy of ±10 arcseconds. A counter balance is also mounted onto the arm of the chi circle. These two circles are positioned upon two translation stages giving horizontal and vertical adjustment within 10 μm. All the motors are controlled from the SPEC software, which is also used elsewhere on the beamline. The theta circle has an encoder installed.

SIXS and CRISTAL at SOLEIL (Alessandro Coati, S. Ravy)

SixS (Surface Interface X-ray Scattering) is a wide-energy range (5-20 keV) beamline dedicated to structural characterization of surfaces, interfaces (solid-solid or solid-liquid), as well as nano-objects in controlled environments by means of surface-sensitive x-ray scattering techniques, such as: Grazing Incidence X-ray Diffraction (GIXD), Crystal Truncation Rods (CTR), Grazing Incidence Small Angle X-ray Scattering (GISAXS), Anomalous Surface X-ray Scattering, X-ray Reflectivity (XRR), Coherent Diffraction, Magnetic Surface X-ray Scattering (in the near future)
CRISTAL is a high-performance undulator-based beamline providing state-of-the-art techniques such as coherent diffraction, time-resolved diffraction, and high angular and high spatial resolution diffraction. Time-resolved pump-probe experiments are operational at the picosecond resolution, and soon (2014) at the femtosecond resolution.
The three instruments are:
- A 2-circle power diffractometer equipped which multi-analyzers
- A 4-circle diffractometer for precise high-q measurements
- A 6-circle diffractometer, offering an exceptional experimental potential.

SIRIUS at SOLEIL (Philippe Fontaine)

The SIRIUS (Soft Interfaces and Resonant Investigaton with Undulator Source) beamline results from the merging of two proposals (Soft Interfaces and Complexes Systems and Resonant and Magnetic Diffraction) and it is devoted to the study of surfaces, complex systems, magnetic materials and nanostructures exploiting the grazing incidence scattering both at fixed energy and in anomalous or resonant conditions (beam energy: 2-10 keV).

DIAMOND: I07 (Chris Nicklin)

The design of Beamline I07 includes the capacity GISAXS and X-ray reflectivity (XRR) in addition to GIXRD enabling the structure of surfaces and interfaces to be investigated under a wide range of well defined and controllable environments. The beamline has two experimental hutches. The first experimental hutch (EH1) is equipped with a z-axis vertical diffractometer, specially suited for samples with horizontal geometry. Users' chamber can be mounted on the diffractometer (open geometry).

The second experimental hutch (EH2) hosts a z-axis horizontal diffractometer. This diffractometer is dedicated to Ultra-High-Vacuum studies and is coupled with a UHV chamber. The simple can be prepared in-situ and for this reason one or several K-cells or e-beam cells can be

mounted on users' demand. Ion sputtering, LEED, Auger spectroscopy are available as standard tools for cleaning simple purposes. Moreover, the beamline also offers a UHV workshop for simple preparation equipped with ion gun, temperature control, e-beams, STM, LEED… for required long sample preparation sessions and equipped with baby chambers for transferring the sample from the Surface Lab. to the horizontal diffractometer (EH2) or to mount directly the baby chamber on the vertical diffractometer (EH1).

DIAMOND: I16 (Alessandro Bombardi)

The beamline provides X-ray diffraction, Imaging and WAXS (Wide Angle X-ray Scattering Spectroscopy) techniques devoted to Materials Science and Magnetism: electronic, magnetic and mechanical properties. The diffraction facility is optimised to combine high flux and high resolution over a wide and continuously tunable energy range, for diffraction and scattering experiments.

The high flux is essential for two key categories of study:

- measurements of very weak, but increasingly important, scattering processes, such as diffraction from magnetic, charge and orbital ordering;
- measurements on very small samples volumes, including artificial nanostructures, thin films and surfaces.

The intense, low-divergence undulator beam can be focused to a spot less than 50 by 200 microns, with an energy range that is continuously tunable from 3.3 keV (below the uranium M-edges) to around 15- 25 keV depending on the optical configuration. Energies in the range 2.7-3.0 keV are now available but require a non-standard set-up to reduce air absorption and should be discussed with beamline staff.

A diamond crystal phase retarder is available to convert the linearly polarised X-ray beam to circular polarisation.

Material Science Beamline at the Swiss Light Source (P. Willmott)

The MS beamline has just undergone a comprehensive upgrade. The wiggler has been replaced by a short-period (14 mm) in-vacuum, cryogenically cooled, permanent-magnet undulator, (CPMU, U14), while the front end and optics have been completely redesigned to optimally exploit the characteristics of the U14 source. In addition to providing fundamental improvements to both powder and SXRD experiments, the upgrade should allow new experimental setups previously excluded to the beamline, such as coherent x-ray diffraction imaging and micro-Laue diffraction. A SAXS/WAXS setup employing both Mythen and Pilatus 2M detectors is presently being commissioned. Materials Science beamline specifications: Photon energy range 5–40 keV, Flux at 12 keV $>10^{13}$ photons/s, Energy resolution $\Delta E/E=1.4\ 10^{-4}$, Focus at SD station (1:1) Better than 200μm (h)x30μm (v).

Brookhaven National Laboratory: ISR (Christie Nelson)

Two stations using 3m undulator in high beta straight section. ES-A: heavy 6-circle heavy diffractometer. ES-B: multipurpose diffractometer.

Energy range from 2.4 to 23 keV for resonant studies of a very wide range of 3 to 5d elements. Full polarization control and analysis. KB mirrrors: 1 μm vertical focussing. Coherence type of experiments. Techniques: GIXRD, XRR, GISAXS, Polarized XRD, RXS.

Brookhaven National Laboratory: X6B (Elaine Dimasi), **X22A** (Nathalie Bouet)

X6B is optimized for x-ray scattering with high reciprocal space resolution and large q range. Reflectivity, surface scattering resonant scattering, and powder diffraction. Located in a bending magnet section. WAXS, SAXS, GISAXS and pole figure configuration using a CCD camera (15-70 cm). Techniques: GISXRD, XRD wide angle, x-ray reflectivity.

X22A (bending magnet) is a diffraction beamline to study thin films, multilayers,

catalytic materials, electro-chemical interfaces operating at fixed energy (10 keV). The beam is focused to a spot of 0.1 to 1 mm^2 and is equipped with a 4-circle spectrometer. Techniques: XRD, single crystal, wide angle, SXRD, x-ray reflectivity.

PETRA III: P09 Resonant Scattering and Diffraction beamline (Jörg Strempfer)

P09 is designed to operate in the hard x-rays regime with energies ranging from 2.7 to 50 keV. The beamline consists of three experimental hutches. The first two experimental hutches, EH1 and EH2, are dedicated to resonant X-ray scattering and general diffraction (RSD) experiments. The third hutch, EH3, houses a Hard X-ray Photoelectron Spectroscopy (HAXPES) setup.

Experimental Hutch 1 is used for resonant X-ray scattering experiments to investigate magnetic order, orbital order or other processes giving rise to non zero intensity at otherwise forbidden positions in reciprocal space. In addition other scattering experiments requiring good energy tunability between 2.7 and 24 keV or variable polarization, like non-resonant magnetic scattering, can be performed. A phase retarder and a polarization analyzer are available in order to vary and analyze the polarisation of the incoming and scattered beam, respectively. Closed-cycle cryostats covering the temperature range between 1.7K and 800K and a He-flow cryostat are available. Complete windowless operation of the diffractometer is also possible.

APS: 6ID-B and 4ID-D (Magnetic Scattering beamlines) (Jon-Woo Kim, Yejun Feng)

6-ID-B,C is the main branch beamline on sector 6. It's primary focus is on magnetic x-ray scattering and general diffraction experiments using a Huber ψ-diffractometer located in the B experimental station. The B station also is equipped with a second diffractometer for scattering in applied magnetic fields (4 Tesla continuous; up to 30 Tesla pulsed).

Supported Techniques

- Magnetic x-ray scattering
- Anomalous and resonant scattering (hard x-ray)
- General diffraction
- Grazing incidence diffraction

Beamline 4-ID-D focuses on polarization dependent spectroscopic and scattering studies of magnetic materials. This beamline is equipped with crystal phase retarding optics that allow the user to manipulate the polarization of the incoming x-ray beam on the sample (i.e., linear to circular ($P_c \sim 0.98$) or horizontal linear to vertical linear ($P_{lin} \sim -[0.80\text{-}0.95]$)

Supported Techniques:

- Magnetic Circular Dichroism (hard x-ray)
- Anomalous and resonant scattering (hard x-ray)
- Magnetic x-ray scattering

6. BEAMLINE SET UP

The diagram below shows a schematic general and simple representation of the complete beamline, placed in a medium straight section front-end position in the experimental hall of ALBA. SIRENA would be located in the free space of beamline 15 next to beamline 13 (XALOC).

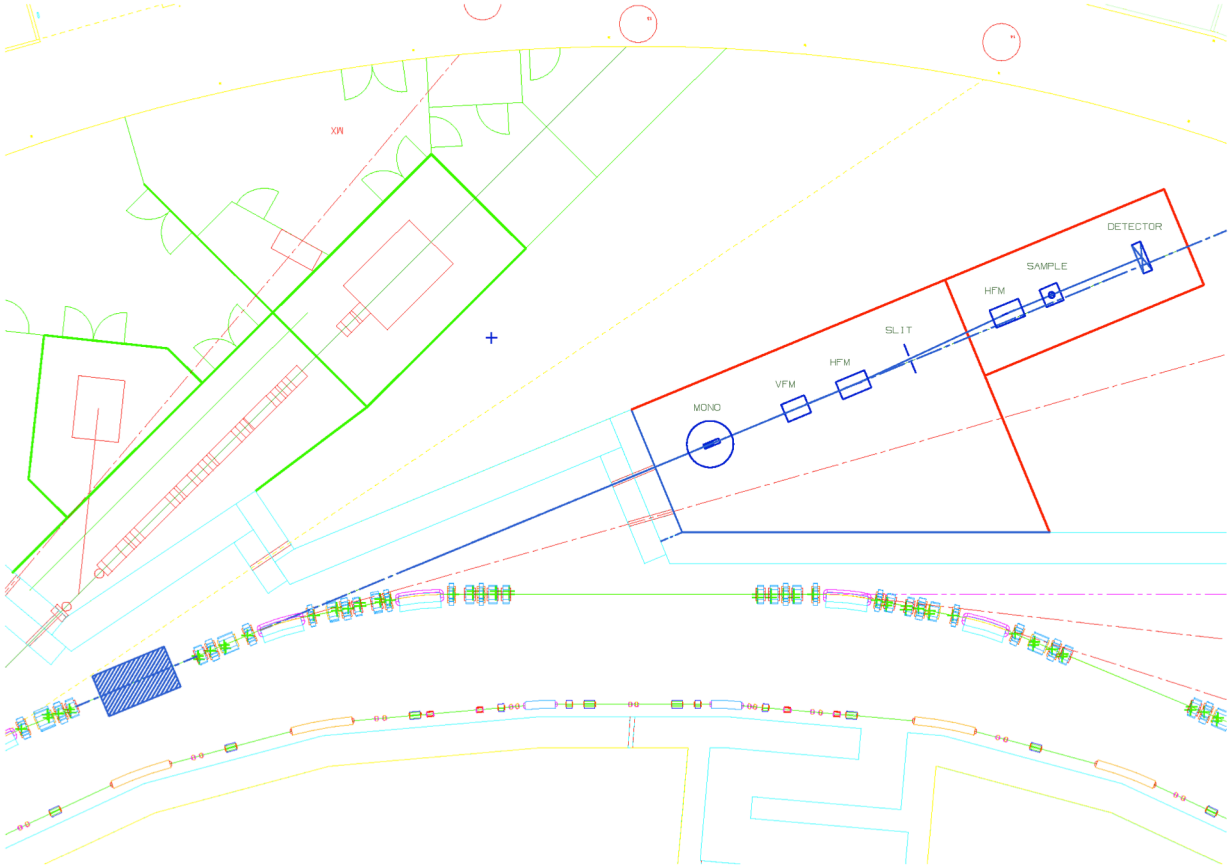

Figure general beamline layout. *Schematic of sector layout showing the possible location of SIRENA (beamline 15) in the experimental hall of ALBA. Blue and red end station corresponds to SIRENA; green design shows the neighbour beamline (XALOC: beamline 13).*

The description of the optical layout indicating the distance to the source of the main components of the beamline in meters is given in the Figure optics layout (section 6.2). The beamline comprises an upstream optical hutch OH (white beam section) and a downstream experimental hutch EH (monochromatic beam section). A more detailed description of the different components in both hutches is given in the next sub-sections.

6.1 Source

The ALBA ring will provide high brilliance for energies in the 4.5 to ~25 keV range (2.5-0.5Å). This range is optimum to obtain high resolution in reciprocal space for length in real space in the order of 0.1-100 Å. This means that the interatomic bond lengths are diffracted to distances in the order of millimeters to centimeters one meter away from the sample, enabling to use common detectors for measurement and still allowing ample space for complex sample environments (electrochemical setups, gas systems, UHV systems…) and/or additional techniques (Spectroscopy…). This energy range is the range where the L and M edges of many elements are

found, allowing for anomalous studies. The scattering power is also generally decreasing when going to higher energies, the energy range of ALBA is therefore well suited to studying small volume samples and low concentration species.

We propose an in vacuum U21 undulator or similar device (continuous lines in figure) could, in principle, fix the desired energy range (better than an in vacuum U24 undulator dashed lines in figure). Due to the small gap needed, this undulator should work under vacuum and placed in a 4m short section of CELLS. The section has a relatively small vertical dimension of the electron beam which is appropriate.

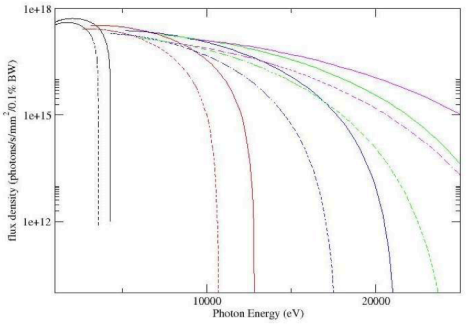

The beamline has to allow the possibility of being windowless from source to sample which is convenient if it operates at 6 keV or less. In the most common cases the beamline has to have only one Be window at the end of the optical components.

A set of filters and attenuators will be installed to reduce heat load if required.

The energy range of this undulator can cover all the 3d transition metals, Se and Br chalcogens (K-edges), the 4d through the lanthanides and most of the 5d elements (L-edges); and the actinides (M-edges) whilst providing the beamline with reasonably high intensities at high energies (harmonic > 9 for E > 25 keV).

6.2 Optics layaout and mirror focusing.

At present we have only done a preliminary ray tracing without any detailed optimization of the optical design and consequently we give only general comments.

The optics design of Xaloc at Alba consisting in a channel cut monocromator and a KB mirror pair with demagnifications is a first approach to the optics of SIRENA. The KB pair at Xaloc demagnifies the vertical source size by a factor 3.8 and the horizontal by 6.6. The result is a cigar-shaped beam at the sample position (as in nearly all undulator beamlines) with measured FWHM dimensions of 52 (H) x 5 (V) μm^2 [O1]. The vertical dimension is considered to be satisfactory for most experiments since at a grazing incidence angle of 0.5 deg. The footprint on a flat sample would be 0.6 mm only. However, the horizontal dimension is too large for some experiments as for example GISAXS or coherent scattering. As the demagnification of the source has to be much more pronounced in the H direction than in the vertical one (ratio of source dimensions = 17), it will probably necessary to introduce a two stage horizontal focusing with an intermediate slit acting as a secondary source (Figure optics layout). To reach a small square beam at the sample may be in practice impossible due to geometric restrictions. Suppose that a horizontal focusing meridional mirror (HFM) is installed at 25 m from the source and that focuses the beam to a slit at 2 m downstream that will act as secondary source. The demagnification is 12.5; as the sample position will be at, say, 32 m from the source, a second H focusing mirror located at 1.5 m from τηε sample (closer may be unpractical), introduces an additional demagnification of 3.5/1.5 = 2.3. The combined total H demagnification would be 12.5 x 2.3 = 28.7 which would lead to a horizontal FWHM at the sample of approximately 300/28.7 = 10.4 μm.

In the vertical direction the source size (FWHM) is 18 μm which can be demagnified to 7 μm by inserting a vertical focusing mirror (VFM) at ca. 23 m from the source. The above values are only indicative but the reality will not be that different.

The strong demagnification of 28.7, increases the H divergence of the beam from 112 mrad FWHM (divergence of the source) to 0.112x28.7 = 3.2 mrad = 0.2 deg. which starts to be high and might be larger that the mosaicity of the samples in some cases. However, it is considered, at present, that a FWHM beam of ca. 10 x 7 μm^2 is achievable and already very good.

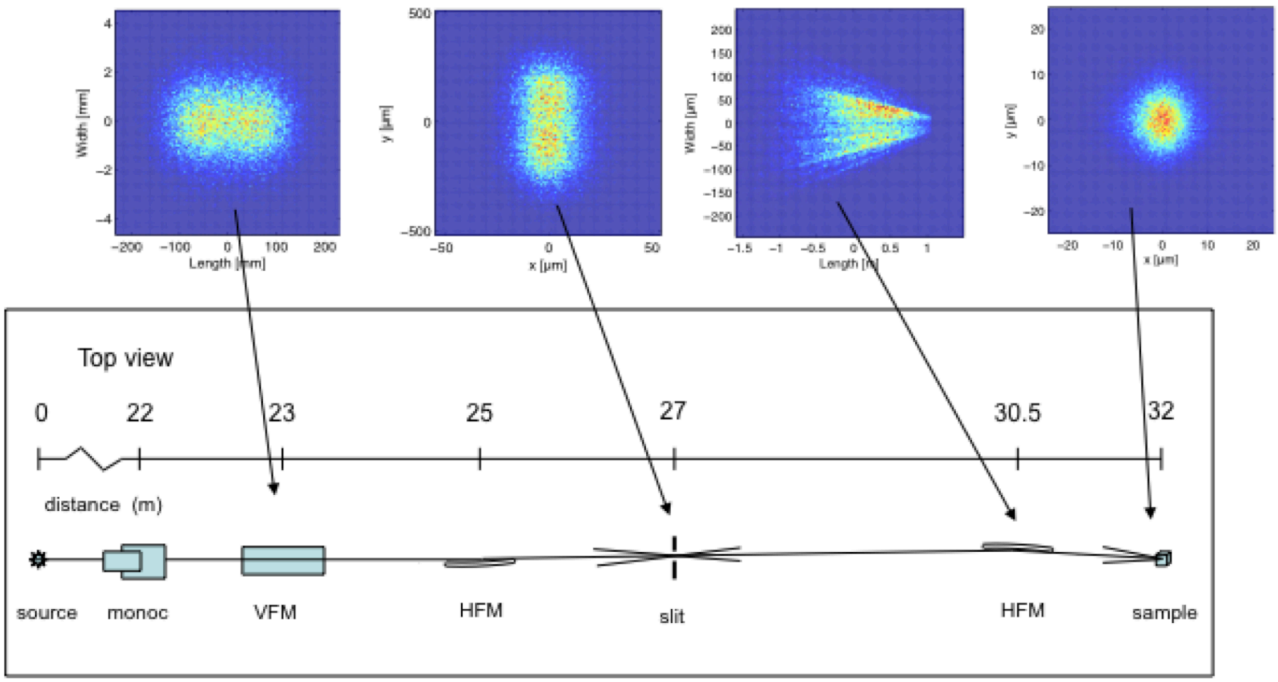

Figure optics layout. *As shown in the ray tracing upper figures, the evolution of the footprint of the beam through the different optical elements to the sample is shown. The beam dimensions at the sample position are approximately 11x10 μm^2 FWHM.*

6.2.1 Monochromator

As stability of the beam position is a figure of merit for grazing diffraction experiments, a cryogenically cooled channel cut Si(111) monochromator is the best option as it has been demonstrated in practice in a number of operating beamlines [O1].

6.2.2 Ancillary

The beamline would be equipped with filters to absorb low energy photons when required, and the appropriate beam diagnostics as it is usual in these kind of beamlines.

6.2.3 Polarization control

The incident linear polarized radiation can be converted into circular polarization using a quarter phase plate. This technique would allow looking at highly anisotropic magnetic materials for which the direction of the sample magnetization cannot be reversed. The plate assembly it is situated upstream of the diffractometer before the last mirror. The (111) diamond crystal is mounted on a goniometer and should be driven to the quarter wave condition with two circles. The rotation

stage, which moves the crystal to the Bragg condition, should have an accuracy of 10^{-4} degrees. Orthogonally mounted to this circle a second circle should be placed to set the optical axis of the diamond at 45 degrees to the incident and plane polarization with an accuracy of ±10 arcseconds. These two circles are positioned upon two translation stages giving horizontal and vertical adjustment within 10mm. Both beams, incident and transmitted, are phase shifted between them when the diamond crystal is slightly detuned from the Bragg position (111). Linear polarization is obtained when the phase shift is $\pm\lambda/2$ (half wave plate). With a diffractometer operating in vertical geometry an incident vertical polarized beam is particularly useful to measure the intensity corresponding to π-σ' and π-π' channels. Circular polarization is obtained when the phase shift is set to $\pm\lambda/4$ (quarter wave plate), and it is particularly useful for the study of chiral or helical magnetic structures.

A polarization analyzer, as the one described in the next section, could be placed at the detector arm to complete the magnetic scattering setup. This setup is fully suitable for detecting the change in the x-ray beam polarization induced by the scattering of chiral structures.

6.3 Experimental station set up

The proposed goniometer is a tentative design that recovers all the instrumental requirements needed to achieve the scientific aims proposed in this project. It has 2 degrees of freedom for the detector arm. The detector arm of the goniometer should have a combination of slits + polarization analyzer + 2D detector mounted on a circle to avoid diffracted beam intersection problems (Fig. polarization analyzer). The goniometer will work in vertical configuration without restriction in reciprocal space. Vertical configuration is good when a high spatial resolution perpendicular to the surface substrate is required, or when it is not possible to set the substrate surface perpendicular to the floor (liquids, electrochemical, polymers, etc.). The goniometer should be open enough to install different sample environments without restrictions in the reciprocal space. These sample environments should ideally be provided by the beamline: batch and flow reactor chambers [O2], electrochemical cell, liquid house for Lagmuir Blodgett, furnace and cryostat, UHV baby chambers and Surface Preparation Laboratory. The spatial resolution would be of (+/- .002 r.l.u.) as maximum. The motor speed should be optimized in order to reduce the travelling times. The maximum time should be set at 60 second per each complete motor turn.

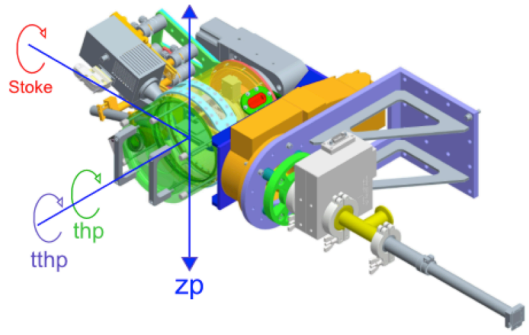

Fig. Polarization analyzer *including the rotation axis:*
zp: sample translation; thp: sample rotation;
tthp: detector rotation

An independent mounting system with a sample-detector distance variable from 1.5-3 metres for GISAXS will be provided for simultaneous GISAXS and wide-angle scattering. The flexible diffractometer geometry enables both hard x-ray diffraction with significant air paths, and tender x-ray studies with thin windows and minimal air path. Incident beam K-B mirrors will provide vertical spot sizes down or close to 1mm. The system will be designed to minimize vibrations and will incorporate features that optimize use with surface preparation equipment [O3].

6.3.1 Multipurpose Diffractometer

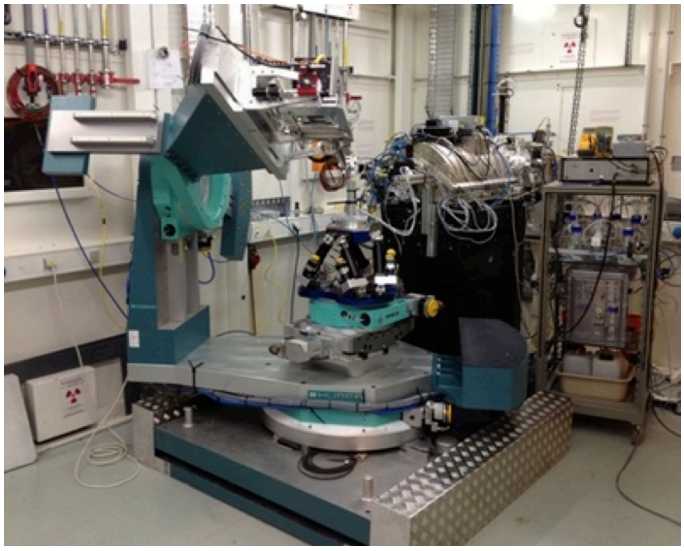

The choice of a multipurpose diffractometer with vertical geometry (sample surface horizontal) has many advantages from a mechanical point of view to its capability to accommodate heavy chambers. In addition, the possibility of working with a vertical polarization with an analyzer crystal tilted of 45° makes this geometry perfectly equivalent to the vertical one. The laboratories interested by the different experiments, in collaboration with the ALBA staff, will carry out the definition of the specific chambers to be adapted to this diffractometer. The maximum load supported by the mechanics would be in the range 150 to 200 kg.

As indicated in the optics layout displayed in Figure "optics layout (section 6.2)", a mirror at 23 m from the source will focus vertically the beam to the sample position. The reflecting surface will be mounted downwards and the reflected beam will make a downwards angle respect the horizontal. As the angle of incidence of the meridionally focusing mirror will be around 4 mrad, the reflected beam will be at an angle of 8 mrad i.e. about 0.5 degrees with the horizontal. This is an appropriate angle for grazing incidence studies on horizontal liquid surfaces.

The main limitation can be given by the necessity of space in order to be able to install the sample environment proposed for such studies at the diffractometer. A minimum sample-closer element (guide tube, KPBM mirrors…) distance of about 100-150 cm should be considered.

6.3.2 Detectors

Detectors have undergone a fast evolution in the last few years and this evolution will continue at the current rate during the period the beamline will be designed and built. It is expected to have a larger offer of detectors with designs and performances more evolved than the current ones. For this reason we will not propose any specific detector for the beamline but just we will briefly describe some of the current detectors that could fit each scientific area:

• Crystallography and coherent diffraction: MAXIPIX is a high spatial resolution (small pixels), high frame rate, photon-counting pixel detector developed by ESRF for synchrotron beamlines. MAXIPIX is best suited for experiments requiring:
- very low noise detection (photon-counting)
- high dynamic range
- pixel pitch: 55 x 55 μm^2
- exposure time range: 1 μs – 1023 s
- readout dead time 0.29 ms
- beam energies between 5 keV and 25 keV

• GISAXS: PILATUS 2M is a large area detector consisting of an array of 8x3 PILATUS modules. A total of 1475x1679 pixels cover an active area of 254x289 mm^2.
- pixel pitch: 172 x 172 μm^2

- readout time: 2.3 ms
- format: 1475 x 1679 pixels

• Dynamic experiments: PAD detector (Pixel Array Detector) is a 2-dimensional imager capable of storing subsequent frames in less than 0.5 microseconds. It can be used for time resolved experiments where speed is a critical factor.
Some of the main PAD goals are:
- Integration time per frame from 1 msec to a few seconds
- Dead-time between frames less than 400 ns
- Format: 1000 x 1000 pixels
- Counting rates: 10^4 x-rays/pixel/microsecond

• Magnetic scattering: APD detector **(Avalanche Photodiode):** Avalanche photodiode detectors have and will continue to be used in many diverse applications such as laser range finders, data communications, photon correlation studies or resonant x-ray scattering experiments. The ideal APD would have zero dark noise, no excess noise, broad spectral and frequency response, a gain range from 1 to 10^6 or more, and low cost.

These detectors are well suited for applications requiring high sensitivity and fast response times. They are used to detect single photons for photon correlation studies and are capable of achieving very short resolving times.

References Optics:

[O1] J. Junahuix et al., J. Synchrotron Rad. **21** (2014) 1
[O2] R. van Rijn et al., Rev. Sci. Instrum. **79**, 085103 (2008)
[O3] P.F. Lyman, D.T. Keane, and M.J. Bedzyk, *AIP Conference Proceedings* **417**, 10-13 (1997).

7. WEAK POINTS OF NEW SYNCHROTRON FACILITES

One of the first goals intended by the first large-scale 3rd generation synchrotron radiation facilities providing electron energies higher than 5 GeV and capable of delivering X-rays from undulators with enhanced brightness, as the ESRF, was to provide software solutions to the users of these facilities to allow for the tracking of the experiment in real time and allowing the decision-making for possible changes in the orientation of the experiment, if necessary, simultaneously to the analysis on-line of the measure. However, in the recent synchrotrons as DIMAOND, SOLEIL…) this is not the case.

These facilities are making enormous economic efforts to provide powerful and versatile beamlines able to cover a large number of possible experiments, distributed by scientific areas, but at the same time they penalize extremely important aspects as data acquisition and analysis on-line software that allows to the experimentalist to see if the data that are being acquired are worth or meaningless. Our experience indicates that there is an enormous waste of beamtime. This is a long standing pending problem still unsolved.

In practice, users prefer go to beamlines where this problem is less acute.

Limitations encountered by users in this field and that today do not seem to have a nearby temporal solution:

• The software used to control the experiment only allows, in most of the cases, what its name suggests: to enable data collection with no real possibility of verification of the measured data. Most current measures contemplate the use of CCD cameras for data collection. The problems related with the current lack of software available to users to check the measured data are, moreover, enhanced due to security restrictions imposed by the synchrotrons to access to this software. These control measures even prevent the access to the (limited/reduced) software that could be implemented in the same computers controlling the experiment or not allowing reading data stored in restricted folders.

• The software control package should provide a powerful environment for the operation of the x-ray diffractometers. Specific functionalities like geometry calculations, operation modes and macro libraries for different standard diffraction geometries (same package for controlling different types of diffractometers) like four circles, six circles, kappa, two circles, and other types of diffractometers. Moreover, this software should be flexible enough to accept new geometries in collaboration with users, i.e., multi-circle diffractometer including unusual degrees of freedom as azimuthal rotation of the detector arm as well as non-standard geometries as those previously mentioned.

Together with the specific diffractometer functionalities, the user interface software should be rather intuitive and be presented to the users with an optimal environment for data acquisition including experimental sequences, large choice of hardware supported, data analysis routines and data display.

Nowadays, one of the most advanced software control packages taking into account all these considerations is SPEC software package. At present it is the most flexible and best-adapted program relating motor positions and reciprocal space coordinates. Moreover, it also offers an intuitive and easy way to display and manipulate the output data from the experiment due to its easy output format, highly compatible with standard software or made user programs.

For these reason, it would be necessary that the control programs of the end stations contemplate SPEC.

• It is detected a lack of collaboration between facilities to implement already tested software, but always in development, from one installation to another. The software groups giving support to the beamlines, if any, work with human resources well below the actual demand that users need. Most of the data acquisition applications also allow visualizing measured data, however, they are not sufficient either quantita- or qualitatively for proper supervision of the experiment.

Examples: crystallographic measures with 2D cameras not recording the motor positions controlling sample orientation, resolution parameters defining the intensity evolution and peak widths with

diffraction angles. Powder diffractometers offering high-resolution capabilities but not calibration files for subsequent correction of diffraction patterns. Unconventional diffractometers with multiple uses that allow even performing surface diffraction experiments. The data is usually given to users with little information on the geometry and correction sources affecting them, i.e. Lorentz factor, footprint, slits defining the beam size whose positions (horizontal and vertical slits and vice versa) are exchanged as function of the diffraction angle during the measurement, etc…. These are just a few examples of the lack of software to control and monitor the experiment during its execution.

The solution is not easy but we should encourage the interrelation between synchrotron facilities for minimally unify the programming language and sharing software development of interest to all of them. Source code-sharing would allow the development of identical packages with specfic variations tailored to the particular characteristics of each facility. The interaction with users could also be a point to consider. However, this point does not offer great potential because users usually make their own software most of the times useless for its distribution between beamlines due to the software design itself. Computing services usually do not recommend them due to excessive investing time required for being adapted to a useful network distribution.

8. ESTIMATED BEAMLINE COSTS

Source		
Insertion device + frontend	900 k€	
Beamline & Optics		
Other equipment (Slits cooled + flight tubes + pumps + etc.)	390 k€	
Three mirrors set plus mechanisms	500 k€	
Monochromator System	300 k€	
Single diamond phase retarder setup (UHV chamber and mechanics)	50 k€	
Diamond crystal	20 k€	
		2160
Infrastructure		
Hutches (shielding)+fluide+wiring+Safety	480 k€	
		480
Experiment		
Multiaxis Diffractometer (with analyzers)	530 k€	
Polarization analyzer	50 k€	
Detectors	350 k€	
SAXS table+tube	190 k€	
Magnetic scattering devices	60 k€	
UHV flow reactor:	200 k€	
Sample environments	500 k€	
Nitrogen gas stream cooling system	50 k€	
Helium gas stream cooling system and control electronics	60 k€	
Cryostat (close cycle)	60 k€	
		2050
User control room		
Enclosure	40 k€	
Control electronics	130 k€	
Commercial analysis software	40 k€	
Data acquisition computing and electronics	50 k€	
Lab (sample preparation equipment, microscope, etc.)	100 k€	
		360
SUB-TOTAL		5050 k€
CONTINGENCY (10%)		505 k€
TOTAL		**5555 k€**

9. ANNEX I. USERS:

9.1 Project Supporting Scientist.

Dr. X. Torrelles Albareda, Inst. Ciencias de Materiales Barcelona CSIC
Dr. M.J. Capitán Aranda, Inst. Estructura de la Materia CSIC
Dr. J. Álvarez Alonso, Dpto. Fisica de la Materia Cond. UAM
Dr. Oier Bikondoa, XMAS beamline (BM28), ESRF
Prof. Fernando Rey García, Inst. de Tecnol. Química (ITQ) Valencia, UPV-CSIC
Dr. Esther Barrena, Inst. Ciencia de Materiales Barcelona CSIC
Prof. Jaume Veciana Miró, Inst. Ciencias de Materiales Barcelona CSIC
Dr. Alejandro Fernández-Martínez, Centre Nat. Recherche Scientific, CNRS (France)
Dr. Leonardo Soriano, Dpto. Física Aplicada, UAM
Dr. Pilar Ferrer-Escorihuela, BM07, DIAMOND (UK)
Prof. Enrique Rodríguez Castellón, Dpto. Química Inorg. Crist. y Miner., Univ. Málaga
Dr. Miguel A. Ciria, Inst. Ciencia Mat. Aragón, CSIC
Dr. Carlos Quirós Fernández, Dept. Física, Univ. Oviedo
Prof. Josep Lluis Tamarit, Física e Ingen. Nuclear, UPC
Dr. J. J. de Miguel Llorente Dpto. Fisica de la Materia Cond. UAM
Dr. Enrique Herrero, Dpto. Química Física Univ. Alicante
Prof. Juan M. Feliú, Dpto. Química Física Univ. Alicante
Dr. Alfonso Cebollada, Inst. de Microelectrónica de Madrid CSIC
Dr. Jorge M. Martínez, Inst. de Microelectrónica de Madrid CSIC
Dr. Miguel A. Rodríguez Pérez, Dpto. Física de la Materia Condensada Univ. Valladolid
Prof. José A. de Saja Sáenz, Dpto. Física de la Materia Condensada Univ. Valladolid
Dr. Rafael Andreu Fondacabe, Dpto. Química Física Univ. Sevilla
Dr. Juan J. Calvente Pacheco, Dpto. Química Física Univ. Sevilla
Prof. Enrique Fatás, Dpto. Química Física UAM
Dr. Concepción Alonso, Dpto. Química Física UAM
Dr. Miguel Clemente, Inst. Ciencia Molecular Univ. Valencia
Dr. Javier Díaz, Dpto. Física de la Materia Condensada Univ. Oviedo
Prof. Fausto Sanz, Dpto. Química Física Univ. Barcelona
Dr. Mercedes Pérez Méndez, Inst. de Polímeros CSIC
Dr. Julio Camarero de Diego, Dpto. Física de la Materia Condensada UAM
Dr. Germán Castro, Inst. de C. Materiales de Madrid (SPLINE) CSIC (ESRF)
Dr. Jose A. Martín Gago, Inst. de C. Materiales de Madrid CSIC
Dr. Maria F. Lopez, Inst. de C. Materiales de Madrid CSIC
Dr. Maria Alonso, Inst. de C. Materiales de Madrid CSIC
Dr. F. Pigazo, Inst. de C. Materiales de Madrid CSIC
Dr. F. Javier Palomares, Inst. de C. Materiales de Madrid CSIC
Dr. Carlos Prieto, Inst. de C. Materiales de Madrid CSIC
Dr. Alicia de Andrés, Inst. de C. Materiales de Madrid CSIC
Dr. Carmen Ocal Moncayo, Inst. de C. Materiales de Barcelona CSIC
Dr. M. Eugenia Dávila Benítez, Inst. de C. Materiales de Madrid CSIC
Dr. Juan de la Figuera Ballón, Dpto. Física de la Materia Condensada UAM
Prof. Rodolfo Miranda Soriano, Dpto. Física de la Materia Condensada UAM
Dr. Amadeo L.V. de Parga, Dpto. Física de la Materia Condensada UAM
Dr. Juan José Hinarejos Murillo, Dpto. Física Materia Condensada UAM
Prof. Clara Conde, Dpto. Física de la Materia Condensada Univ. Sevilla
Dr. Mª Ángeles Gómez Rodríguez, Inst. Ciencia y Tecnología de Polímeros CSIC

Prof. Geoff Thornton, University College London and London centre for Nanotechnology
Dr. Robert Lindsay, The University of Manchester
Dr. Hadeel Hussain, The University of Manchester

9.2 Interested Scientific Groups by areas

9.2.1 Surface crystallography and thin films

- Group of Crystallography of Magnetic and Electronic Oxides and Surfaces: ICMAB-CSIC
Prof. José Luis Garcia Muñoz, Dr. Xavier Torrelles
Interests: ferroelectric/ferromagnetic films and interfaces, molecular systems, oxides

- NANOMOL (Molecular Nanoscience and Organic Materials): ICMAB-CSIC
Prof. Jaume Veciana, Prof. Concepció Rovira, Dr. José Vidal, Dr. Nora Ventosa, Dra. Marta Mas
Interests: Molecular systems for electronicsm molecular magnetism and nanomedicine. Structure and assembly of molecular systems.

- MULFOX (Multifunctional Oxides and Complex Structures): ICMAB-CSIC
Prof. Josep Fontcuberta, Dr. Gervasi Herranz, Florencio Sánchez.
Interests: ferroelectric/ferromagnetic films and interfaces, 2-dimensiona electron gas, spintronic.

- SURFACES: ICMAB-CSIC
Prof. Carmen Ocal, Esther Barrena
Interests: Organic films, oxides, molecular growth

- Dpt. of Condensed Matter Physics: UAM
Electronic Properties:
Prof. Enrique Garcia Michel, Dr. Arantzazu Mascaraque
Surface Science Laboratory (LASUAM): UAM
Dr. Ma. José Capitán, Dr. Jesús Álvarez (XRPS: UAM)
(TIREMISU: TIme REsolved MIcroscopy of SUrfaces)
Dr. Roberto Otero, Dr. José María Gallego
(SMOKE: Surface Magnet–Optical Kerr Effect)
Dr. Julio Camarero
(DANYELA: He diffraction, LEED, MED, AES, MOKE
Dr. Juan José de Miguel Llorente
(TEAMS / HIS : Thermal Energy Atomic Molecular scattering)
Dr. Daniel Farías

- ESISNA: Structure and Nanoscopic Systems Group. ICMM-CSIC
Prof. J.A. Martín Gago, Dr. Javier méndes Pérez-Camarero, Dr. Paqui López Fagundez, Dr. Pedro de Andrés
Interests: Nanoscience and Astrobiology, Nanostructuration of organic molecules, TiO2: structure and catalysis, Fullerenes, 2D systems, graphene.

- Dpt. of Physics, Universidad Complutense de Madrid
Dr. J. García Barriocanal
Interests: Oxides, films, perovskites.

- Dept. of Physical Chemistry, Universidad Laguna

Dr. Pilar Carro
Interests: self-assembling systems, 2D organic systems

- Nano-Bio Spectroscopy Group (Univ. Pais Vasco)
Prof. J.Enrique Ortega
Interests: Extended systems: solids, surfaces, liquids. Applications (e.g photovoltaics)

- Dpt. of Physical Chemistry and Analytical (Universidad de Oviedo)
Prof Santiago Garcia Granda, J, R. García,
Interests: Crystallography, resonance, oxides.

- Dpt. of Condensed Matter Physics (Universidad de Oviedo)
Dr. Carlos Quirós, Dr. J. R. Garcia
Inerests: Magnetism, resonance, polarization, oxides, films, organic sysems.

- Thin Films Group (ICMM)
Prof. C. Prieto
Interests: Thin films, oxides, perovskites.

- Charles Univesity, Praga
Dr. Xavier Martí
Interests: antiferromagnetic semiconductors, films, oxides, ferroelectrics, spintronics.

- Group of Electronic and Magnetic Materials and Heterostructures (ICMM)
Prof. Alicia de Andrés, Ana Espinosa, A. Alberta, …
Interests: Thin films and multilayers (SnO2, MnP films y MnP nanocrystals embedded GaP epilayers grown on GaP(001), magneto structural properties of FeO NPs)

- Dpt. of Nanostructures and Surfaces (ICMM)
Prof. Jesús Gonzalez Fernández, Prof. Isabel Montero Herrero, Prof. Ma. del Carmen Muñoz de Pablo, Prof. Federico Soria Gallego, Dr. Ma. Aloso Prieto, Dr. Ma. Eugenia Dávila Benítez, Dr. Fco. Javier Palomares Simón, …
Interests: Thin films, oxides, magnetism, 2D organic systems,…

- Dpt. of Surfaces, Coatings and Molecular Astrophysics (ICMM)
Prof. José Cernicharo Quintanilla, Prof. José Ángel Martín Gago, Prof. Fco. J. Meseguer Rico, Prof. Luis Fernando Vázques Burgos, Dr. Pedro de Andres Rodriguez, Dr. Ignacio Jiménez Guerrero, Dr. Elisa Leonor Román García, …
Interests: heterostructures in nanoscale, low dimensional advanced materials, silicon nanostructures, organic molecules building blocks, surfaces and interfaces: liquids, organic systems, oxides, metals…

- Department of Electromagnetism and Electronics (Univ. Murcia)
Dr. J. Sanchez-Lacasa
Interests: Fast X-ray imaging acquisition

- Department of Biomaterials and Materials Bioinspired
Prof. José Serafín Moya Corral, Prof. Carlos J. Serna Pereda, Dr. Carlos Peacharroán García, …
Interests: Phase transition and percolation

- Department of Applied Physics (Univ. Politécnica de Cartagena)
Dr. José Abad López, Manuel Caravaca Garratón and José Damian Catalá Galindo

Interests: Ordered molecular systems with GIXRD

- Quantum Nanoelectronics Group (CIN2)
Dr. José Santiso López, Dr. J. Roqueta
Interests: strain, microstructure, magnetism, epitaxial thin films, manganites,…

- Hasylab at Bessy
Dr. F. Bertram
Interests: MgO, photovoltaic semiconductor technology, thin films (photovoltaic applications)

- Surfaces, Interfaces and thin films (ICMS, Sevilla)
Prof Francsico Yubero
Interests: Thin films and óxidos

- BMO7 - DIAMOND (UK)
Dr. Pilar Ferrer-Escorihuela
Interests: Topologic oxides, 2D organic systems.

- Magnetic Materials Department (ICMA-CSIC)
Dr. Miguel A. Ciria Remacha: magnetic nanoetructures and aplications (GIXRD + GISAXS)

9.2.2 Catalysis

- Heterogeneous catalysis (HT and P) (Inst. Tecnolog. Química, ITQ Valencia)
F. Rey García (ITQ Valencia) Zeolitas, Powder diffraction to model system
J.L. Llordá, S. Valencia, M. Palomino, José M. Serra.
Interests: Zeolitas, Powder diffraction to model system. Fuel cells and membranes.

Avelino Corma, Viente Fornes Seguir, German I. Sastre Navarro.
Interests: Molecular and supramolecular catalysts for chemical reactions.

- MNM: Membranes and Nanostructured Materials Section (niversity of Zaragoza)
Dr. Joaquin Coronas Ceresuela, Dr. Carlos Tellez.
Interessts: Development and applications of nanostructured materials, specially porous materials. Composites of interest: zeolites, porous titanosilicates and related systems, layered materials, delaminated materials, ordered mesoporous silicas, metal-organic frameworks.

- COMORCA: Organometallic Compounds and Catalysis (University of Oviedo).
Prof. José Gimeno, Victor Cadierno, Javier Borge, Pascale Crochet, Sergio E. García Garrido, Joaquín García Álvarez, Dr. Josefina Diez (Organic and Inorganic Chemistry Dept., University of Oviedo)
Interests: processes, recycling through biphase catalysis.

- CATHETER: Heterogeneoous Catalysis (Universitat Rovira I Virgili)
Prof. Francesc Medina, Jesús Sueiras, Vladimir Baulin, Sandra Contreras, Anton I. Dafinov, Mayra García, Anna María Segarra, Vanessa Torné, Hayden Webb, Susana Domínguez, Sandra Ramos.
Interests: Multifunctioal heteroheneous catalysts, chiral and achiral molecules, laminar hydroxides, environmental catalysis: water purification, biomass conversion,…

- Group of Chemical Catalytic and Polimerization Reactors (Universidad Pública de Navarra)

Prof. Luis Maria Gandía Pascual, Maria Cruz Arzamendi Manterola,, Idoia, Campo Aranguren, Ainara Moral Larrasoaña, Alberto Navajas León, Inés Reyero Zaragoza, Irantzu Uriz Doray.
Interests: Biofuels, production from organics oils and wastes, heterogeneous catalysis, catalytic combustion and total oxidation of volatile organic compounds, hydrogen for fuel applications, microreactors, nanotechnology: metallic nanoparticles, Fischer-Tropsch synthesis, etc..

- Catalysis for Environment and Energy Group (ICMS-CSIC)
Prof. Alfonso Caballero Martínez, José Antonio Navío Santos, José Antonio Odriozola Gordón, Miguel Ángel Centeno Gallego, Gerardo Coón Ibáñez, Maria del Carmen Hidalgo López, Juan Pedro Holgado Vázquez.
Interests: Developments of surface chemical functionalization processes, eg, superhidrofilic and self-cleaning surfaces under day light illumination, development of micro-reactor welding procedures, application of micro-reactor technology ot hydrogen production and pollution abatement.

- Dpt. of Inorganic Chemistry, Crystallography and Mineralogy (Univ. De Málaga)
Enrique Rodríguez Castellón
Interests: catalysis and GISAXS

9.2.3 Electrochemistry

- LEMMA: Laboratory of Electrochemical materials and Environment, Dept. of Chemical Physics, Chemistry Faculty, Univ. de Barcelona.
Prof. Jose Lluis Cabot
(www.ub.edu/dept-qf/grups/elecmatma/index.html)
Interests: Degradation of organic pollutants by oxidation electrochemicalprocesses, fuel cells, redox characterization of magnetic organic rafdicals in aquous media, electrosynthesis of organic and inorganic materials

- Phys. Chem Department (Univ. of Alicante)
Prof. Juan Maria Feliu
(Web.ua.es/es/eqsup/investigacion/pil)
Interests: Physical electrochemistry, fundaments of electrocatalysis, Nanoparticles and fuell cells, microbial fuel cells,..

- University of Murcia
Angela Molina Gómez
Interests: Characterization of multielectronic processes by electrochemistry

- University of Barcelona
Enric Brillas Coso
Interests: Oxidation electrochemical processes for cleaning water.

- University of Oviedo
Agustin Costa García
Interests: Nanomaterials in electrochemistry to monitoring reactions.

- University of Bristol
David J. Fermin
Interests: Dynamic Photoelectrochemistry of Quasi One-dimensional semiconductors assemblies

- University of Zaragoza

Juan R. Castillo Suárez
Interests: Functional nanoparticles by electrochemical thecniques.

- University of Aberdeen, Scotland, UK
Angel Cuesta Ciscar
Interests: Interatomic effects at the electrode-electrolyte interfaces.

- Universidad de Alicante
Dr. José Solla Gullón
Interests: Nanostructured metallic materials for electrochemistry.

- University of Vigo
Mª del Carmen Pérez Pérez
Interests: Corrosion in metallic structures.

- Universidad de Alcalá de Henares
Alberto Scarpa Miguel
Interests: Biotechnological microfluidic electrochemical systems

- Université Pierre et Marie Curie (UPMC)
Carlos M. Sánchez-Sánchez
Interests: Electrocatalytic reactions at surface structured electrodes.

- University of Sevilla
Francisco Prieto Dapena
Interests: Organic systems on metal electrodes.

- Universidad de Barcelona
Elisa Vallés Giménez
Interests: Electrochemical preparation of micro/nanostructure alloys.

- Universidad de la Laguna
Gonzalo García Silvestro
Interests: CO and alcohol electro-oxidation, metallic carbides and nitrides as catalysts.

- University of Cordoba
Guadalupe Sánchez Obrero
Interests: Molecular assembly on gold alloys.

9.2.4. GISAXS

- Nanostrucutres Functional Materials Group: (ICMS-CSIC)
Juan Pedro Espinós Manzorro, Manual Ocaña Jurado, Agustín Rodríguez González-Elipe, …
Interests: Development of materials to achieve more efficient low-cost solar cells, development of environmental and bio optical sensors, development of functional coatings for optical applications, UV protection, and bioactive films.

- Surfaces Group: ICMAB-CSIC
Esther Barrena, Carmen Ocal
Interests: polymers, solar cells, self assembling molecular systems.

- NANOMOL (Molecular Nanoscience and Organic Materials): ICMAB-CSIC
Prof. Jaume Veciana and Group members.
Interests: Molecular systems for electronicsm molecular magnetism and nanomedicine. Morphology and assembly of molecular systems.

- Leibniz-Institute for New Materials / Inst. Microelectron. Madrid (CNM-CSIC)
Dr. Lola González García, Julian Parra Barranco, Manuel Oliva Ramírez
Interests: Structure, correlation length, TiO2 deposited thin films, porosity, water adsorption

- Microbiology (Universidad Granada)
Prof. Mohamed Larbi Merroud
Interests: Nanoparticles (NPs) on surfaces (Sulphur), microbial synthesis on core/Shell gold/palladium NPs; Catalysis: selective oxidation of Benzyl-Alcohol over Biomass-supported Au/Pd bioinorganic catalysts. Magnetic gold nanoparticles. S-layer proteins for gold adsorption and Au-Np formation.

- ISTerre, CNRS & University Grenoble Alpes: (CNRS) France
Dr. Alejandro Fernández Martínez
(Collaborators: Rafael Perez-Lopez (Universidad de Huelva))
Interests: mineralogy and physico-chemical properties at liquid(solution)-mineral interfaces during nucleation or mineral dissolution by using GISAXS and reflectivity. Biomineralization and formation of carbonates.

- Dpt. of Inorganic Chemistry, Crystallography and Mineralogy: (Univ. de Málaga)
Prof. Enrique Rodríguez Castellón
Interests: Nanoporous materials for catalysis: NO reduction, H2S partial oxidation, H2 production and CO oxidation.

- Organic Nanostructured Photovoltaics (The Institute of Photonic Sciences ICFO)
Prof. Jordi Martorell
Interests: To enhance the performance of organic photovoltaic materials: 1-dimensional photonic crystals (efficiency), nano-thick stacking of several material layers (transparent solar cells), organic molecules adjacent to metal nano-structures (control of the energy transfer mechanism). Topics: Transparent cells, Graphene PV cells, surface nano.structured cells, Tandem OPVs

9.2.5. Coherence

- (XMAS beamline, ESRF)
Dr. Oier Bikondoa

- Biophotonics: Medical Optics Group (The Institute of Photonic Sciences, ICFO)
Dr. Turgut Durduran
Interests: Development of new technologies using advanced photonics for pre-clinical and clinical bio-medicine:
Transcranial, non-invasive neuro-monitoring with diffuse optics. Diffuse optical instrumentation for translational and clinical biomedical research. Physics of photon migration in live tissues. Translational oncology research. Translational stroke research

- Advanced Fluorescence Imaging And Biophysics Group (The Institute of Photonic Sciences, ICFO)
Dr. Melike Lakadamyali

Interests: Dynamics, stoichiometry and organization of ion channels:
Intracellular transport of organelles. Super-resolution microscopy of transcription. Super-resolution fluorescence microscopy

- Optical Institute of Madrid – CSIC. Visual Optics and Biophotonics Lab
Dr. Susana Marcos
Interests: Development of imaging techniques for investigation of the human visual system, and the development of new vision correction alternatives. Aplications of this technology to:
The understanding of the imaging mechanisms of the optical system of the eye (cornea and crystalline lens). Advance of the understanding of the biological mechanisms and early diagnosis of ocular pathologies. Evaluation and new designs of refractive and presbyopic corrections.

9.2.6. Resonance and energy polarization dependence

- Joaquín García, Materials Science Institute (ICMA-CSIC)
Interests: Charge density, weak interactions, ferroelectric systems, magnetism

- Javier Blasco, Materials Science Institute (ICMA-CSIC)
Interests: Charge density, weak interactions, ferroelectric systems, magnetism

- Gloria Subias, Materials Science Institute (ICMA-CSIC)
Interests: Charge density, weak interactions, ferroelectric systems, magnetism

- Fernando Bartolomé, Materials Science Institute (ICMA-CSIC)
Interests: Charge density, weak interactions, ferroelectric systems, magnetism

- Spyros Perlepes, Patras University
Interests: Transition metal clusters, magnetic properties

- Gianluca Ciatto, SOLEIL Synchrotron
Interests: Diffraction Anomalous Fine Structure Spectroscopy, III-V semiconductors

- Richard Winpenny, Manchester University
Interests: Coordination chemistry, molecular magnets, nanoscale, polynuclear complexes

- M. Grazia Proietti, Zaragoza University
Interests: DAFS; MAD. semiconductors

- Renevier Hubert, CNRS-INPG Grenoble
Interests: DAFS, GIMAD, GIDAFS, heterostructures

- José Luis García Muñoz, Materials Science Institute (ICMAB-CSIC)
Interests: RXS, charge and orbital ordering, transition metal oxides

- Javier Herrero-Martín, BL-29: BOREAS, ALBA synchrotron (ALBA-CELLS)
Interests: Charge density, weak interactions, ferro electric/magnetic systems, magnetism, oxide thin films…

- Jesús A. Blanco, Oviedo University
Interests: Resonant X-ray scattering

- Claudio Mazzoli, ESRF Synchrotron
Interests: Magnetic and resonant x-ray scattering